

# **Pore-scale Characterization and Modelling of Kapp Toscana Group reservoir sections using X-ray micro-CT.**

*Jeroen Van Stappen*

Academiejaar 2012–2013

Scriptie voorgelegd tot het behalen van de graad  
Van Master of Science in de geologie

Promotor: Prof. Dr. V. Cnudde  
Co-promotor: Prof. Dr. S. Olausen  
Begeleiders: T. De Kock, M. Boone  
Leescommissie: Prof. Dr. M. De Batist, Prof. Dr. J. De Grave

## Nederlandstalige samenvatting

Het UNIS CO<sub>2</sub> Lab in Longyearbyen, Svalbard, beoogt tegen 2025 een CO<sub>2</sub> neutrale stad van Longyearbyen te maken. Hierbij zou de CO<sub>2</sub> die uitgestoten wordt in de steenkoolcentrales die verantwoordelijk zijn voor de stroomvoorziening in de stad, gecapteerd moeten worden en opgeslaan in de gesteentelagen onder Longyearbyen. Wanneer ook de transportsector aangepast wordt naar een systeem waarbij waterstof uit deze steenkoolcentrales als brandstof wordt gebruikt, kan de cirkel rond worden gemaakt en zal een CO<sub>2</sub> vrij systeem gecreëerd worden. Deze visie, die zijn oorsprong vindt in 2006, kan echter geen werkelijkheid worden zonder een degelijke karakterisatie en analyse van de gesteentelagen die te vinden zijn onder Longyearbyen. Sinds 2007 werden hiervoor 7 boringen uitgevoerd in de onmiddellijke nabijheid van de stad. Hierin werden gesteenten van de Kapp Toscana Groep en meerbepaald van de Wilhelmøya Subgroep geïdentificeerd als de sectie die het meest geschikt wordt geacht voor CO<sub>2</sub> opslag. Deze gesteenten werden aangeboord in twee boringen: Dh2 en Dh4. Sinds hun identificatie waren ze het onderwerp van vele studies, onder andere deze van Ogata et al. (2012) die de nadruk legde op het belang van breuken in deze Subgroep voor potentiële CO<sub>2</sub> opslag. Echter, de manier waarop deze met elkaar geconnecteerd zijn, hun lengte en opening zijn nog onzekere factoren. Onder andere daarvoor, maar ook voor een algemene verdere karakterisatie, werden beide boorkernen in het kader van deze thesis bemonsterd. In totaal werden 12 staalnames uitgevoerd in de boorkernen. Deze werden aangevuld met staalnames van de dagzoomende Subgroep in het veld. In de drie afzonderlijke locaties (op het veld, in Dh4 en in Dh2) werd de Subgroep selectief bemonsterd in de zandsteen gedomineerde secties. Met het doel de gesteenten van de verschillende locaties te kunnen vergelijken werden 3 afzonderlijke lithologs opgesteld: één van de dagzoomende sectie in de valleien Konusdalen en Criocerasdalen, één van Dh4 en één van Dh2. Deze afzonderlijke lithologs werden vervolgens gecorreleerd.

Aan de universiteit van Gent werden de stalen gescand met verschillende X-stralen computer tomografie scanners, ontwikkeld door het UGCT. Door deze analyses uit te voeren wordt gebruikt gemaakt van een non-destructieve techniek waarbij 3D beelden verkregen worden van de interne structuren van gescande stalen. Op deze manier kan een verdere karakterisatie gegeven worden van de gesteenten van de Wilhelmøya Subgroep. Door het “downscalen” van de staalnames kan deze analyse gebeuren met verschillende resoluties. Op deze manier worden de stalen gekarakteriseerd op de schaal van de volledige kern, maar ook op de schaal van individuele poriën en breuken. De CT analyses worden aangevuld met metingen van open porositeit en permeabiliteit in het laboratorium, alsook door een algemene analyse van 8 slijpplaatjes die gemaakt werden van de veldstalen. Tot slot worden de beelden, die verkregen worden door de scans, gebruikt als basis voor numerische modellering van de gesteenten met gespecialiseerde software. Het poriënnetwerk wordt hierbij uit de gescande beelden onttrokken en vervolgens gesimplificeerd. Op dit netwerk worden vervolgens “flow” simulaties uitgevoerd waarbij onder andere de permeabiliteit van het gesteente kan berekend worden.

Om te beginnen werden de gesteentestalen gescand aan een relatief lage resolutie. Deze bedroeg 41 µm voor de veldstalen, 56.61 µm voor de stalen uit boorkern Dh4 en 62.56 µm voor de stalen uit boorkern Dh2. Het verschil in resolutie is te verklaren door de grootte van het monster: kleinere (cylindrische) stalen kunnen namelijk dichterbij de X-stralen bron geplaatst worden. Door de kegelvormige configuratie waarin de X-stralen worden uitgezonden zorgt dit voor een groter beeld op de X-stralen detector. Op deze resoluties was het mogelijk om een algemene karakterisatie te

geven van de verschillende stalen wat betreft het facies wat terug te vinden is in het gesteentemonster, de fossielen die in de scans kunnen herkend worden en indien aanwezig op deze resolutie, de porositeit en eventuele breuken die terug te vinden zijn in de stalen. Op deze manier werd het onderscheid gemaakt tussen heterogene en homogene gesteenten, werden ichnofossielen als *Thalassinoides* en boorgangen en -kamers van *Upogebia affinis* beschreven, en werd een eerste karakterisatie van de porositeit en de breuken in de gesteentes gegeven. Hierbij werden de breuken geanalyseerd voor wat betreft hun oriëntatie, hun maximale opening en indien mogelijk de lengte waarin ze invloed uitoefenen in de gesteenten. Op basis van hun algemene uiterlijk en de fossielinhoud konden verschillende gesteenten, van verschillende locaties, reeds beter met elkaar gelinkt worden. Bovendien werd aan deze lage resolutie reeds duidelijk dat er een belangrijk verschil is tussen de breuken die teruggevonden worden in de veldstalen en deze die de stalen uit de boorkernen affecteren. Wat betreft hun maximale opening vallen de breuken uit stalen van verschillende locaties nog met elkaar te vergelijken. Waar deze in de veldstalen voornamelijk schommelen rond 123  $\mu\text{m}$  en 205  $\mu\text{m}$  zijn de breuken in stalen van boorkern Dh4 aan deze resolutie te karakteriseren met maximale openingen van 169.83  $\mu\text{m}$  tot 283.05  $\mu\text{m}$ . Aangezien de volgende maximale opening die met de analytische software Morpho+ in de veldstalen berekend kan worden 287  $\mu\text{m}$  bedraagt, kan er geconcludeerd worden dat de breuken die terug te vinden zijn in de boorkernstalen gekarakteriseerd worden door een maximale opening vergelijkbaar aan de maximale opening van de breuken in de veldstalen. Een ander raakpunt betreft de plaats in het gesteente waar breuken zich vormen. Voor zowel de veldstalen als de kernstalen blijken de breuken zich te vormen bij plaatsen met een hogere klei-inhoud in de gesteenten. Het verschil zit hem echter in de frequentie waarmee de breuken in de stalen te vinden zijn en de lengte waarmee ze invloed uitoefenen op het gesteente. Op lage resolutie zijn in alle scans van de veldstalen breuken terug te vinden. Van de 11 gescande stalen van Dh4 en Dh2 zijn er slechts in 5 stalen breuken terug te vinden. Hiervan is er bovendien in 1 van de stalen sprake van opgevulde breuken of aders in het gesteente. Wat betreft de lengte van de breuken, die benaderd werd door de diameter van een omgevende bol voor elke breuk te bepalen, valt op dat de breuken in de veldstalen op de scans de hele diameter van het gesteentemonster affecteren. Dit komt overeen met een lengte van ongeveer 3.6 cm. Doordat deze breuken tot aan de zijkant van de stalen reiken, moet deze lengte als een minimale lengte beschouwd worden. Voor de stalen uit boorkernen Dh2 en Dh4, konden op lage resolutie breuken in 3 stalen gekarakteriseerd worden betreffende de lengte. Deze breuken kennen hun oorsprong en einde binnen de grenzen van de stalen en zijn daarom geen minima waarden, maar maxima. Maxima tot 2.1 cm werden behaald, terwijl de gemiddelde diameter voor de omgevende bol bepaald werd op 3.58 mm tot 4.80 mm. Het is duidelijk dat de breuken in de veldstalen onderhevig geweest zijn aan vorstverwerking, wat ervoor gezorgd heeft dat de breuken verder konden propageren in het gesteente.

Vervolgens werden substalen genomen met een diameter van 5 mm en 2 mm van zowel de veldstalen als de stalen uit de boorkernen. Doordat deze kleiner zijn, konden ze gescand worden met een hogere resolutie. De substalen met een diameter van 5 mm behaalden een resolutie van 3.99  $\mu\text{m}$  en deze met een diameter van 2 mm konden gescand worden met een resolutie van 2.8  $\mu\text{m}$ . Één specifiek substaal, genomen in sample D2 uit Dh2, behaalde met een diameter van 2 mm zelfs een resolutie van 1.68  $\mu\text{m}$ . De substalen in de veldstalen werden allen genomen in gebieden binnenin de stalen die door de eerdere scans gekarakteriseerd werden door (i) een verhoogde porositeit binnenin het gesteente, (ii) homogeniteit wat betreft mineraalverdeling en (iii) de afwezigheid van breuken.

Op deze manier wordt de distributie van poriën de belangrijkste factor voor analyse. In totaal 5 veldstalen werden op deze manier geanalyseerd aan de resolutie van 3.99  $\mu\text{m}$ . In 4 van deze substalen was het mogelijk om een porositeit te bepalen in de resulterende beelden. De verkregen porositeit bleek echter voor alle vier deze substalen ontoerijkend om de open porositeit te evenaren zoals deze voor de stalen werd bepaald bij laboratorium tests. Bij het vijfde substaal werden helemaal geen poriën gevisualiseerd. Het besluit dat hieruit kan getrokken worden is dat minstens een deel van de poriën kleiner moet zijn dan de verkregen resolutie van 3.99  $\mu\text{m}$ . Ook de breuken, die zichtbaar waren bij lagere resolutie zullen bijdragen tot de porositeit zoals bepaald door de laboratorium proeven.

3 substalen van de acht eerder gescande stalen uit Dh4 werden geanalyseerd aan een resolutie van 3.99  $\mu\text{m}$ . Twee van deze substalen, beide met een open porositeit bepaald in laboratorium proeven van meer dan 10 vol%, toonden micro-porositeit op deze resolutie. Ook al gaven de porositeitswaarden die bepaald werden in deze scans niet de open porositeitswaarden uit laboratorium tests, toch zijn deze beide scans de meest geschikte voor verdere analyse op te verrichten aan de hand van CO<sub>2</sub>-“flow” simulaties, die dadelijk besproken zullen worden. Het derde substaal werd gekenmerkt door het voorkomen van horizontale micro-breuken. De karakterisatie van deze breuken leidde tot het bepalen van de maximale breukopeningen op 16  $\mu\text{m}$  tot 20  $\mu\text{m}$ . Hun maximale verbreiding in het gesteente werd berekend op 2.27 mm. De gemiddelde diameter van de omgevende sferen voor de micro-breuken in het gesteente was echter een behoorlijk stuk lager. Deze bedroeg namelijk slecht 0.23 mm. Uit boorkern Dh2 werden vervolgens ook 2 substalen gescand met een resolutie van 3.99  $\mu\text{m}$ . Deze scans leverden soortgelijke resultaten op als deze van substalen in Dh4: micro-porositeitswaarden konden bepaald worden, maar deze bereikten niet de waarden als berekend in open porositeit proeven in laboratoria. In het substaal genomen in D1 werden micro-breuken gekarakteriseerd met maximale openingen van 8  $\mu\text{m}$  tot 23.9  $\mu\text{m}$ .

In zowel Dh4 als Dh2 leverden scans aan de resolutie van 2.8  $\mu\text{m}$  soortgelijke resultaten op als de scans met een resolutie van 3.99  $\mu\text{m}$ . Waar breuken konden geobserveerd worden vertoonden deze een horizontale orientatie en werden ze gekarakteriseerd met maximale openingen tussen 8.4  $\mu\text{m}$  en 25.2  $\mu\text{m}$ . De gemiddelde diameter van omgevende sferen in subsample C4 werd bepaald op 175  $\mu\text{m}$ . Dit is nogmaals een betoog dat de breuken die op deze hoge resoluties worden geobserveerd zeer subtiele kenmerken van het gesteente zijn.

Gesteente modellering en intrusie simulaties werden uitgevoerd op 4 stalen. Als basis hiervoor werden volgende scans van substalen genomen van Dh4: C1, C3, C6 en C7. Bij deze stalen werden de poriën onttrokken uit de scans en vervolgens gebruikt in het programme E-core. Hierin werd voor elk substaal afzonderlijk een vereenvoudigde voorstelling gegeven van de poriënstructuur door middel van een “ball-and-stick”-model. Afzonderlijke poriën worden hierin voorgesteld als een bal, terwijl de verbindingen tussen deze poriën als balkvormige “sticks” worden voorgesteld. Analyse van deze vereenvoudigde poriënnetwerken toonde aan dat de poriën in C1 en C3 op deze resolutie onvoldoende verbonden waren om er intrusie simulaties op te gaan uitvoeren. Daarnaast werden ook voor alle stalen de gemiddelde poriëngrootte bepaald. Deze bedroeg voor de vier geanalyseerde stalen ongeveer 11  $\mu\text{m}$ .

Wat volgde waren CO<sub>2</sub> injectie simulaties op de overgebleven substalen van C6 en C7. Hierbij werden de simulaties zowel op het vereenvoudigde netwerk, als op het niet-vereenvoudigde netwerk

uitgevoerd. Bij de simulaties op het vereenvoudigde netwerk wordt een indicatie gegeven van de verdeling van CO<sub>2</sub> en water in de poriën na achtereenvolgende intrusie door beide fluida. Als resultaat op de niet-vereenvoudigde netwerken wordt de absolute permeabiliteit van het gesteente verkregen. Deze resultaten bleken echter niet te kloppen met de gemeten waarden van de gesteenten in een gespecialiseerd laboratorium. Bij de simulaties, zowel op het vereenvoudigde als op het niet-vereenvoudigde netwerk werken telkens te hoge waarden voor wat betreft de permeabiliteit van het gesteente verkregen. Daarom ook dat de resultaten van deze CO<sub>2</sub> injectie simulaties met de nodige aandacht moeten worden geëvalueerd. Indien de scans zouden genomen worden met een nog hogere resolutie, zouden deze simulaties meer waarheidsgetrouwe resultaten opleveren. Dit zou zo zijn, aangezien bij een hogere resolutie de micro-porositeit van het gesteente vertegenwoordigd wordt door een hoger aantal voxels (3D pixels). Dit zorgt voor een betere connectiviteit tussen de verschillende poriën wat voordelig is voor de intrusie simulaties.

Als algemeen besluit kan getrokken worden dat de gesteenten van de Wilhelmøya Subgroep voor het eerst benaderd geweest zijn aan de hand van CT analyses. Hierdoor was het mogelijk een meer gedetailleerde analyse te maken van een slechts beperkt deel van de Subgroep. Voor het eerst werden de breuken uit de kernen in geselecteerde stalen gekarakteriseerd door een maximale opening en werd een indicatie gegeven van de lengte waarin ze de gesteenten beïnvloeden.

## Table of Contents

Acknowledgments.....	7
1. Introduction.....	9
1.1. Geographical and geological setting.....	9
1.2 UNIS CO <sub>2</sub> Lab.....	11
1.3 Research aim.....	13
2. Methods.....	15
2.1 Field work.....	15
2.2 Laboratory characterization.....	15
2.2.1. Open porosity.....	15
2.2.2. Permeability.....	16
2.3 CT.....	18
2.3.1 Hardware and physical principles.....	19
2.3.2 Reconstruction of images.....	22
2.3.3 Analysis.....	24
2.4 Rock modelling.....	27
2.5 Summary of the methodology per sample.....	30
3. Results.....	33
3.1 Field work.....	33
3.2 Laboratory results.....	42
3.2.1 Open porosity.....	42
3.2.2 Permeability.....	43
3.2.3 Thin section analysis.....	43
3.3 CT-data.....	46
3.3.1 Field Samples (S- and T-samples).....	46
3.3.1.1 Scans at resolution 41 $\mu\text{m}$ .....	46
3.3.1.1.1 Facies.....	46
3.3.1.1.2 Fractures.....	49
3.3.1.1.3 Fossil-content.....	52
3.3.1.1.4 Porosity.....	53
3.3.1.2 Scans at resolution 4 $\mu\text{m}$ .....	53
3.3.2 Dh4 Samples (C-samples).....	56
3.3.2.1 Scans at resolution 56.61 $\mu\text{m}$ .....	56
3.3.2.1.1Facies.....	56

3.3.2.1.2 Fractures.....	61
3.3.2.1.3 Fossil-content .....	64
3.3.2.1.4 Porosity.....	65
3.3.2.2 Scans at resolution 4 $\mu\text{m}$ .....	65
3.3.2.2.1 C1.....	66
3.3.2.2.2 C3.....	66
3.3.2.2.3 C7.....	68
3.3.2.3 Scans at resolution 2.8 $\mu\text{m}$ .....	69
3.3.3 Dh2 Samples (D-samples).....	71
3.3.3.1 D3 .....	73
3.3.3.2 D2 .....	74
3.3.3.3 D1 .....	75
3.4 Rock modelling .....	75
3.4.1 Pore network characterization.....	76
3.4.2 CO <sub>2</sub> flow simulations .....	77
4. Discussion.....	81
4.1 Porosity distribution.....	81
4.1.1 Section 1 .....	82
4.1.2 Section 2 .....	83
4.1.3 Sections 3, 4 & 5 .....	83
4.1.4 Section 6 & 7.....	85
4.2 Fracture analysis.....	86
4.2.1 Maximum openings.....	87
4.2.2 Diameter of circumscribed sphere .....	88
5. Conclusion .....	89
5.1 Pore-scale characterization.....	89
5.2 Rock modelling .....	90
5.3 Further research.....	91
6. References.....	93
7. Attachment.....	97

## **Acknowledgments**

To start with I would like to thank my promotor, Prof. Dr. Veerle Cnudde, and co-promotor, Prof. Dr. Snorre Olaussen for the opportunity they both have given me to work in the wonderful environment of Svalbard. Both have trusted me with the first cooperation between the University of Ghent and the University Centre at Svalbard concerning CT characterization of reservoir rocks. For this I am very grateful. Without their help during both the analytical process of the thesis, and the field work at Svalbard, this thesis would not be what it is now. I therefore sincerely hope that my thesis is of value for both Prof. Dr. Veerle Cnudde and Prof. Dr. Snorre Olaussen in their respective area of expertise. I also would like to thank Drs. Kim Senger and Drs. Tim De Kock for their help during the field expedition. Not only was their advice on the field very helpful, but also their companionship at my first ever Friday beer at a latitude higher than 75°N was highly appreciated. That said I would also like to thank all students who I have met during my short stay at Svalbard for their warm welcome, which can also be said for the staff at UNIS, specifically the logistical staff, who even lend us a rifle so we could go hiking at our day off.

In Ghent, the analytical part of my thesis would not have succeeded without the help of the entire SGIG team. Besides Prof. Dr. Veerle Cnudde and Drs. Tim De Kock who were my first hotline with problems, it corners Drs. Marijn Boone without whom my analyses and writings would not have been corrected as accurately as they were which lifted both my moral and analysis speed up when necessary; Drs. Wesley De Boever, who reached me the script from Voorn et al. (2013) which helped for the analysis of the fractures within the rocks; Drs. Tom Bultreys to whom I could go to with theoretical questions; Dr. Jan Dewanckele who often reminded that hard work is the key to success. For their patience and their general help whenever it was needed, my gratitude thus goes to this entire team. I would also like to thank Ing. Pieter Vanderniepen for performing the scans needed for my analyses, and by extension the entire UGCT team for the use of the scanners and their overall help. Daniëlle Schram is thanked for her cheerfulness every time I entered the Laboratory, as well as so many of my fellow thesis students. A special word of thanks goes to everybody who would join me in a coffee break, or help me de-stress at other times. Especially Gijs Berghmans, with whom I shared an office space, Wout Salenbien, who was always into a coffee break when I needed one and also Tim Collart and Thomas Pille deserve to be mentioned for the late nights we spend at the university while the deadline was slowly approaching.

Last, but definitely not least I would like to thank my mother, Hilde Staels, grandmother, Leona Goubert, my sister, two brothers and my sister-in-law for their moral support. I know I am not the most cheerful person to be around when I am stressed, but during the weekends which I spent mostly at home I tried to relax. A perfect time to do this is on a Sunday afternoon, with at the one hand a strawberry pie and in the other one a nice Belgian beer, preferably La Chouffe. For these Sunday afternoons and the way they were spent, my family is warmly thanked.





# 1. Introduction

## 1.1. Geographical and geological setting.

The archipelago Svalbard is located around 650 km north from mainland Norway. It ranges from 74° to 81° north latitude and from 10° to 35° east longitude. As a part of the otherwise submerged Barents Shelf, it lies between the Arctic Ocean, Barents Sea, Greenland Sea and the Norwegian Sea. Geographically it consists of nine main islands of which Spitsbergen is the largest. On this island the city of Longyearbyen is located. The geographical location is illustrated in figure 1.



**Figure 1:** Geographical setting of the archipelago Svalbard, with as largest island Spitsbergen. In the inset Svalbard is localized relative to the northern parts of the European continent in the south, the eastern coast of Greenland in the west and in the south-east the northwestern part of Russia and the island of Novaya Zemlya.

Svalbard, located on the north-western margin of the Barents Shelf, can be subdivided into five fundamental units (Steel & Worsley, 1984; Bergh et al., 1997): (i) Pre-Cambrian to Silurian basement, followed by (ii) localized Devonian to Carboniferous rift basin fills, dominated by sandstones, shales, carbonates and evaporates, and (iii) an upper section of stable marine platform deposits of mostly carbonates, evaporates and shales of Permian ages, followed by (iv) Mesozoic shelf to fluvial deposited sandstones and shales. Finally (v) Cenozoic fold-thrust development takes place with a foreland basin formation, combined with uplift and subsequent rifting in the west, adding complexity to the regional picture.

Geologically spoken, Longyearbyen is located in the Central Tertiary Basin. The term basin here is used in a structural sense for what amounts to a broad synclinal structure. It refers to the whole

post-Devonian cover or platform sequence in Central Svalbard. The Kapp Toscana Group, deposited during the Late Triassic and Early to Middle Jurassic, is an important Mesozoic succession within this basin in which shales, siltstones and sandstones alternate. Strata of this Group crop out extensively in Svalbard and most type sections are found in the Central Basin. The Kapp Toscana Group can be up to 475 m thick in Svalbard and up to 2000 m on the Barents Sea Shelf. It is thought to be a result of deposition in a deltaic environment with reworking of sediments (Worsley, 2008). The Group starts with the dark shales of the Tschermakfjellet Formation which grade upward into siltstones and fine sandstones. It is overlain by the sandstones of the De Geerdalen Formation, a non-marine sequence of fine- to medium-grained plant-bearing sandstones interbedded with silty shales, shaley siltstones and hard calcareous siltstones (Harland, 1997).

The rocks of interest in this research however are those from the overlying Wilhelmøya Subgroup. These are the youngest of the Kapp Toscana Group and are dated to Norian-Toarcian (Båckstrøm & Nagy, 1985). During the Norian and Toarcian, Svalbard experienced a change in mineralogy to mature sandstones, reflecting a different basin configuration, a change in climate and a shift in drainage patterns (Bergan & Knarud, 1993). The Wilhelmøya Subgroup consists of the Knorringsfjellet Formation and the Brentskardhaugen Bed. Overall the Wilhelmøya Subgroup is a condensed section of texturally mature sandstones which were deposited on coastal plains and in deltaic to shallow marine environment. It is important to note that almost 3 km of overburden rock is eroded in the latest Cenozoic. The rocks of the Wilhelmøya Subgroup were sampled from four different locations as indicated on the map in figure 2.

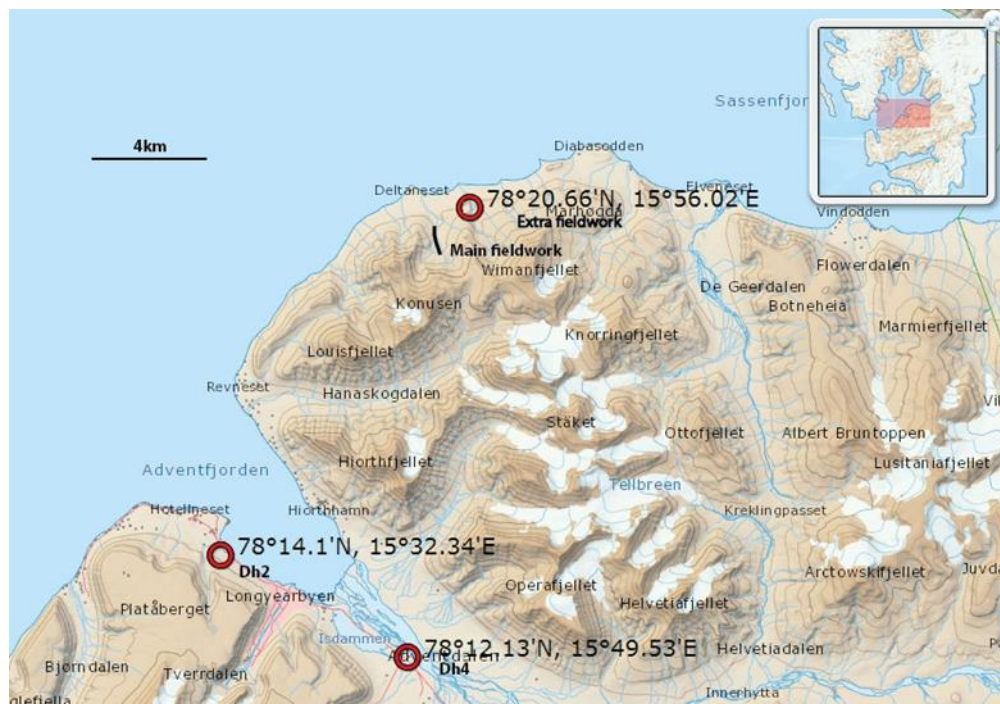


**Figure 2:** Location of fieldwork indicated by a black line along Konusdalen and a red circle in the valley Cricerasdalen towards Wilmanfjellet. The two drill sites Dh2 and Dh4 along Longyearbyen, from which samples were taken for this research, are also indicated. Drill sites Dh1 and Dh3 are not indicated in the figure but are located respectively 15 m from Dh2 and 45 m from Dh4.

The two drill sites Dh2 and Dh4 (localised in figure 2) were developed specifically for the first phase of the UNIS CO<sub>2</sub> project. The correlated logs made after the completion of the wells are added in the

appendix. Since the rocks in this part of Spitsbergen are found in a pronounced Cenozoic synclinal feature, the Wilhelmøya Subgroup is located at a depth of approximately 695 m to 672 m in drill hole 2 (Dh2) and at a depth of 755 m to 733 in drill hole 4 (Dh4). In the two remaining drill sites (Dh1 and Dh3, located respectively 15 m away from Dh2 and 45 m from Dh4) it was only possible to drill into the cap rock section of the overlying Agardhfjellet Formation, belonging to the Janusfjellet Subgroup. All four wells were drilled as part of the first phase in the UNIS CO<sub>2</sub> project from 2007 to 2009.

The Wilhelmøya Subgroup is found in outcrop in the valley Konusdalen close to Deltaneset, approximately 20 km north of drill sites Dh2 and Dh4 (i.e. the drilled unit comes up along the north eastern limb of the synclinal structure). In this valley approximately 15 m of the Knorringfjellet Formation, Wilhelmøya Subgroup was mapped and sampled. At approximately 1 km east from Konusdalen, in a valley informally defined as Criocerasdalen, special attention was given to the uppermost m of the Subgroup, where the 2 m thick Brentskardhaugen Bed is found in outcrop. This is an iron-rich conglomerate bed with clasts mostly of phosphatic, chert or quartz composition. On top of this bed a 5 cm to 7 cm thick condensed phosphatic layer is found followed by layers rich in chamosite, the Fe<sup>2+</sup> end member of the chlorite group.

## **1.2 UNIS CO<sub>2</sub> Lab**

The UNIS CO<sub>2</sub> project finds its origin in 2006 when Grunnar Sand and Alvar Braathen publish an article in Svalbardposten in which they outline the vision of a CO<sub>2</sub> free Svalbard. Longyearbyen, the largest settlement on Svalbard with a population of 2000 citizens, has got a closed energy system with coal mines, a coal fuelled power plant and geological structures that could be suited for CO<sub>2</sub> storage. Soon this vision got political attention and the Norwegian minister of Justice ordered a study on the feasibility of CCS in Longyearbyen. This study was conducted by the University Centre in Svalbard (UNIS) in cooperation with the Norwegian University of Science and Technology (NTNU) and the foundation for scientific and industrial research at the Norwegian Institute of Technology (SINTEF). They concluded that when everything will go to plan Svalbard could be able to be CO<sub>2</sub> neutral by 2025. This is possible because Svalbard is not part of the electricity market on mainland Europe and is not obligated to offer the same fuel for transportation as on mainland Europe. This means that if a coal fuelled power plant with carbon capture and storage (CCS) can provide the electricity and hydrogen from the coal, hydrogen can be introduced into the transport sector as fuel, thus creating a closed and CO<sub>2</sub>-free energy system. Therefore it is a unique location for starting a pilot study of this kind.

Only from December 2011 onwards the UNIS CO<sub>2</sub> Lab AS is officially a spin-off company, 100 % owned by the University Centre but already in 2007 the CCS research conducted by UNIS started with the geological challenges of CCS. Together with partners from the industry, UNIS searched for the best possible reservoir section in the proximity of Longyearbyen. Finding this section and describing it was the main aim of the first of four phases of the project which will be explained in the following text. Since then a total of seven deep wells have been drilled, as well as one shallow well of 61m to understand the permafrost and its possibility to form a seal. These wells were subsequently subjected to detailed analysis and tests. The main result was the confirmation of suitable reservoir sections within the rocks of the Kapp Toscana Group at depths from 670 m to 970 m below Longyearbyen. Because of the low surface temperature in the high-Arctic injected CO<sub>2</sub> will be dense and the transition to the fluid phase will occur at depths of approximately 460 m (Span & Wagner

1996). Therefore the shallow depth of this reservoir section compared to CCS in the North Sea will still be safe for injection. The rocks above this section have got a good sealing capacity in order to keep the CO<sub>2</sub> underground. However due to the fact that the reservoir section is located within the Central Tertiary Basin, injection of CO<sub>2</sub> will happen into a structurally open system with a regional dip to the southwest of 3° (Haremo et al., 1990). The layers of the Kapp Toscana Group are found in outcrop at only 15 km northeast of the injection site as illustrated in figure 3. A number of methods were used to obtain these results during the first phase of the project: drilling together with core logging and sampling; electrical logging; outcrop mapping as well as seismic mapping; constructing digital elevation models; high-Arctic permafrost analysis; subsurface geo-modelling and flow simulations.

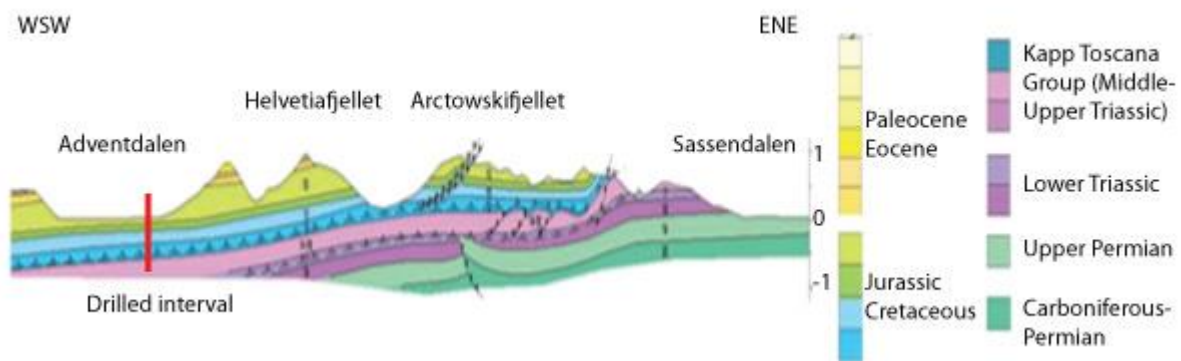


**Figure 3:** Cross section of the geological subsurface from Adventdalen, where the rocks from the Kapp Toscana Group are at a depth of 670 m to 970 m, to Sassendalen where they are found in outcrop (figure modified after Major et al., 2000). The horizontal distance given by this cross section is 30 km while the vertical distance ranges from -1 km to 1 km.

These different research tasks however were not all carried out by UNIS. A long list of partners and contractors to the project were necessary, not only for financial support but also for advisory and research support. Drill hole logging with wire-line tools for example was carried out by the Norwegian Geological Survey (NGU). Together with the borehole cores an overview was given of the subsurface. The results of the borehole logging can be found in the NGU Report 2010.018 (Elvebakk, 2010).

The aim of the second phase of the project was testing the bedrock's ability to store CO<sub>2</sub>. Drill site Dh4 (figure 2) was used to inject fluids in the possible reservoir sections. During this phase the recovered drill cores were also tested for porosity and permeability. This was done on small plugs of sandstone, sent to special laboratories. Although there is a great variation in properties due to differences in facies and diagenesis, the Wilhelmøya Subgroup has been identified as the section that is most suitable for CCS from the entire Kapp Toscana Group (Mørk et al., 2010). From all the plugs that were taken, the highest porosity and permeability (16-18%, 0.6-1.8mD) are recorded in sandstones and sand-supported conglomerates from the Knorringfjellet Formation, just below the Brentskardhaugen Bed. There are however also phosphate- and iron-rich beds within this formation in which the porosity and permeability are strongly reduced. This shows that the Wilhelmøya Subgroup is a very heterogeneous succession. The De Geerdalen Formation that is also part of the Kapp Toscana Group and deposited underneath the Wilhelmøya Subgroup is characterized by an overall lower porosity and permeability (Farokhpoor et al., 2010).

Phase 3 and 4 are still to be executed. It involves respectively medium scale CCS and in the end full scale CCS. During phase 3, which could be seen as a testing phase, the subsurface CO<sub>2</sub> storage will be demonstrated and studied by a start-up phase of approximately 2 years in which traceable water will be injected. This phase will then be followed by a CO<sub>2</sub> injection phase. Since the reservoir below Longyearbyen is physically open, drift of the injected CO<sub>2</sub> towards the North East where the reservoir rocks are in outcrop is expected. For this new monitoring wells will be drilled. Special attention will also be given to the interaction between the rocks, formation water and injected CO<sub>2</sub>. In this phase a more clear view of the storability will be given and of the seal integrity, as well as possible leakage areas along the expected migration path. Phase 4 will be the phase in which full scale carbon capture will happen at the local coal fuelled power plant. The captured CO<sub>2</sub> will then be used as a medium for storage. With this phase the entire energy value chain will be in place and Longyearbyen will be a global show case as a community that takes care of its carbon emissions from the source to the solution. Of course during this phase there will be long term monitoring facilities of the subsurface developments. Although the work has already started to identify capture technologies adaptable to the Longyearbyen power plant, the construction of a capture plant will not start until the storage abilities and qualities have been determined in the previous phase.

Further information about the UNIS CO<sub>2</sub> Lab as well as an overview of the publications linked to the project, newsletters and the research partners and contractors can be found on their website "<http://co2-ccs.unis.no/>".

### **1.3 Research aim**

The aim of this thesis is to provide a further characterization of the rocks of the Wilhelmøya Subgroup. These rocks have been studied intensively on a petrographic scale since the discovery of them in 1973 by Worsley. In 1985 Dypvik et al. published an extensive field and sample description from the Wilhelmøya Subgroup as found at the Bohemanflya-Syltoppen area north of Isfjorden. After lithological, petrographic and palynological analyses they concluded that the Wilhelmøya Subgroup was deposited by marine transgression over a coastal area with low relief. The depositional environment was characterized by low sediment supply and reworking of the sediments. In the same year Bäckström and Nagy published a paper concerning the depositional history and fauna of the Brentskardhaugen Bed specifically. It was concluded that the weak Lower to Middle Jurassic transgression was followed by a regression in the Bathonian which was itself followed by a late Bathonian transgression with deposition of the Brentskardhaugen Bed. This model was refined by Nagy & Berge (2008) who confirmed the depositional setting and the condensed nature of the unit with two important major hiatuses: one in the latest Triassic, earliest Jurassic and one in "mid-" Jurassic.

Since the start of the UNIS CO<sub>2</sub> project however, the reservoir sections of the Kapp Toscana Group have become more interesting for research. Not only are there the UNIS CO<sub>2</sub> lab reports, there is a long list of publications concerning these rocks as a result of the project. Among others is the recent publication of Ogata et al. from 2012 in which they focus on the importance of fractures in the tight reservoir of the Kapp Toscana Group. However, for a better understanding of the pore network, fracture structures and pore connectivity within the reservoir section a new approach is necessary. Models of the pore network, a detailed analysis of the fractures, with special attention to the fracture openings and fracture lengths, and fluid flow models will contribute to the study of CCS in

Longyearbyen. Therefore in this thesis the most interesting sections of the reservoir, as they are defined in the final report of the first phase of the project (Braathen et al., 2012), are sampled and analysed in the laboratory for open porosity and permeability. Not only are the cores in Dh2 and Dh4 sampled for this purpose, but also field samples were taken from two different localities. Furthermore the rocks are analysed with different X-ray computed tomography (CT) scanners developed at the UGCT. This non-destructive type of analysis provides a 3D image of the internal structure of the samples under investigation, such as porosity, mineral distribution, etc. A multi-scale approach, using different types of X-ray computed tomography systems, was applied to analyse the sample from core scale to pore scale. Digital core analysis on the 3D CT images is using specialized fluid flow modelling software and is compared to the laboratory measurements.

## **2. Methods**

### **2.1 Field work**

In order to observe and describe the rocks of the Wilhelmøya Subgroup in detail, three days were spent in the field at Konusdalen and Criocerasdalen, where outcrops along the valley were systematically described using a hand lens, a rock hammer and a tape measure. Metre per metre of rock were described, with special attention to bioturbation, bedding of the rocks, fossil content and, where possible mineralogical composition. During the day time, field notes were taken which were subsequently rewritten in the evenings in order to retain the most accurate descriptions. Also, a number of field samples were taken which were first located in the field notes and subsequently orientated according to their position in the outcrops. Special focus was given to sandstone samples in the outcrops.

A similar methodology was used while describing and sampling the cores. In both Dh2 and Dh4 the Wilhelmøya Subgroup was described in detail, as well as the upper parts of the De Geerdalen Formation, found below the Wilhelmøya Subgroup. This was done because this Formation also contains some important reservoir sections, which could be considered useful for CO<sub>2</sub> injection. Both Dh2 and Dh4 were described with care in order to characterize the facies changes as accurately as possible and to determine the grain size. Where fractures were observed this was noted, as well as bioturbation, siderite levels, or pyrite nodules. Subsequently Dh4 was primarily sampled, specifically in the sandstone sections. These sections were then correlated to core Dh2 in which the facies of the rocks were compared. Interesting samples from Dh2 were then added to the samples in Dh4. The work carried out during these 9 to 10 days in Svalbard could then be summarized in three lithologs with corresponding description and sample characterization. This is given in chapter “3.1 Results: Field work”.

### **2.2 Laboratory characterization**

#### **2.2.1. Open porosity**

In the laboratory rock samples can be analysed for their open porosity. To do this, the standardized characterization test for building stones was applied (NBN EN 1936:1999). The open porosity is compiled by those pores that are interconnected with the constriction that these chains of connected pores are also connected to one of the sides of the sample. These pores then become accessible for fluids to migrate through. The open porosity  $\phi_o$  is expressed as a volume percentage and is the ratio of the volume of open pores to the total volume of the rock. Before measuring the open porosity, the samples were dried in a furnace. It is better to dry with a lower temperature for a longer time than with a high temperature for a shorter period of time. This is done to avoid cracks or mineral alteration to be formed due to the subjection of the samples to high temperatures, according to their thermal expansion coefficient. Particularly samples with a high amount of clay particles tend to be sensitive to cracking. Therefore the samples are preferentially dried at a temperature of 40°C until their mass remains constant for at least 24 hours. Once the water is removed from the pores the dry mass  $M_1$  can be measured. The dry samples then go in a vacuum vessel for two hours after which water is added. When the samples are fully submerged, the vacuum



is maintained for another hour. Then the air pressure is restored. Normally all open pores should be filled with water. To ensure all of these pores are filled, the samples are put to a rest for 24 hours while still being submerged. After this resting period the samples are once more weighted; both below (M3) as above water (M2). The following equation then gives the open porosity:

$$\phi_o = \frac{M2-M1}{M2-M3} * 100 \text{ (vol\%)}$$

### **2.2.2. Permeability**

Permeability is a measure of the ability of a porous media to transmit fluids. It is therefore affected by numerous rock properties such as the pore size and distribution, but also the shape and packing of the grains. Also the amount, distribution and type of clays within rock samples affect the permeability of a rock. In the summary of the first phase of the UNIS CO<sub>2</sub> project by Braathen et al. (2012), a resume is given concerning the permeability measurements on both Dh2 and Dh4. For Dh2 two different approaches were used. First of all there were direct measurements from the core using a Tinyperm II. This is a portable air permeameter specifically used for measurements in outcrop or cores. The permeability measurement range however is limited from 10 millidarcys to 10 darcys. The measurements with the Tinyperm II were carried out above and beneath every core plug taken. These plugs form the second approach and were sent to a specialized Reservoir Laboratory in Trondheim as part of the first phase of the CO<sub>2</sub> project. Six of these plugs lie within the boundaries of Dh2 studied in this research. These six samples had an average porosity of  $8.55 \pm 2.50$  vol% and an average permeability of  $0.165 \pm 0.188$  mD. Core plugs taken in Dh4 were sent to the Petroleum Laboratory of Sintef Petroleum (Braathen et al., 2012). From all the plugs taken from Dh4, 19 lie within the boundaries of the section studied in this research. These 19 plugs had an average porosity of  $13.02 \pm 3.8$  vol% and an average permeability of  $0.377 \pm 0.610$  mD. Figure 4 illustrates the measurements of porosity and permeability available prior to this research as well as the depth at which sampling happened for CT analysis.

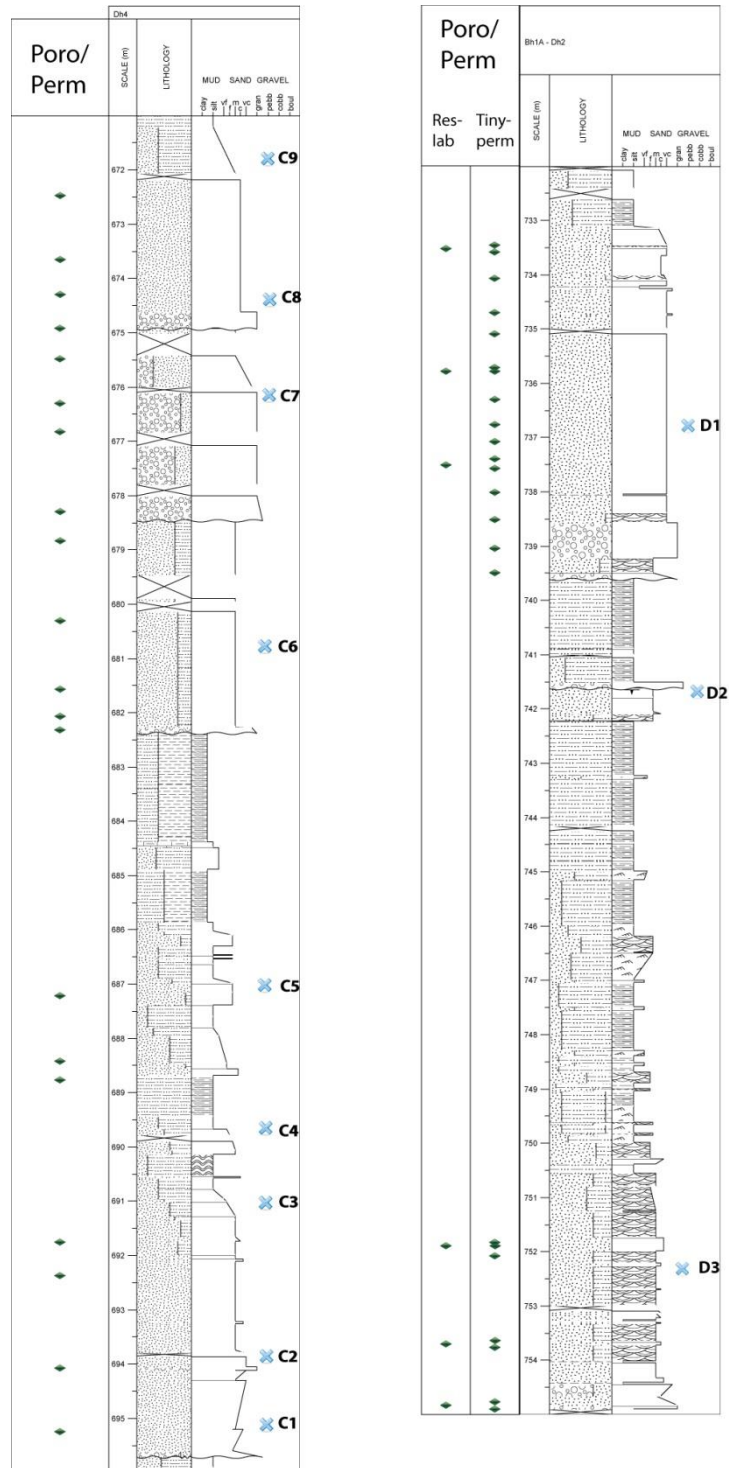


**Figure 4:** Lithostratigraphic log of Dh4 (left) from 671 m to 696 m deep; and Dh2 (right) from 731 m to 755 m deep. Porosity and permeability measurements available prior to this research is indicated in green. Depth of sampling is indicated with a blue X.

Additional permeability measurements were carried out for 4 selected samples (C1, C3, C7 and C8) that were selected on the basis of their facies, size, homogeneity and their correlation with the samples measured prior to this research. This was done at the company PanTerra Geoconsultants B.V. in the Netherlands, using steady-state gas permeability. In this technique, air is forced through

the sample at various pressures. For this research, the pressures used range from 1 atm to approximately 4 atm. At these pressures, the gas flow rate through the sample is measured. Via Darcy's law, the permeability of the sample can be calculated:

$$K = \frac{Q\mu L}{A\Delta P}$$

In this equation K is the permeability, expressed in Darcy (D); Q is the flow rate of gas through the sample (m<sup>3</sup>/s);  $\mu$  is the viscosity of air (1.810 x 10<sup>-5</sup> kg/ms) or any other fluid used for permeability measurements; L is the length of gas penetration (m); A is the surface area of the sample (m<sup>2</sup>) and  $\Delta P$  is the pressure drop across the sample (Pa). When air is the fluid used in this method permeability can be measured from 0.001 mD up to 25 Darcy because of the very low viscosity of it and the ease of penetration of the sample with it. Although the absolute permeability of a porous rock is a constant value, unchanged by the type of fluid used to calculate it, gases at relatively low pressures tend to give a calculated permeability greater than the true permeability of the rock. This is due to the Klinkenberg effect, also known as gas slippage effect. It occurs because when gases occupy pores in a rock, the velocity profile of it is not zero at the walls, but it has a finite velocity in the direction of the flow. This is in contrast to liquid laminar flow in which the layer of molecules which is in contact with the solid material acting as walls from the pores is stationary. Gas molecules however do not flow in layers. Therefore there will be periods when no gas molecule is in contact with the wall at any location on it, yet the congregation of molecules is still flowing through the pores so that they flow with more ease than their liquid counterparts. The result is that the calculated permeability when using gas as a fluid will be higher than the true absolute permeability of the rock. Klinkenberg (1941) however concluded from experiments that gas permeability is a function of the composition of the gas and the mean pressure applied to the system. To calculate the absolute permeability of the rock, following equation can be used:

$$K_L = \frac{K_G}{(1 + b/\bar{P})}$$

In which  $K_L$  is the true absolute permeability of the rock;  $K_G$  is the apparent permeability calculated from gas flow tests;  $b$  is Klinkenberg's slip factor which is a constant for a particular gas in a particular porous medium (atm) and  $\bar{P}$  is the mean flowing pressure of the gas in the system (atm). Notice that the term  $(1 + b/\bar{P})$  always is greater than or equal to 1.0 so that the true permeability will be smaller than or equal to the apparent gas permeability (Tanikawa & Shinamoto, 2006).

### **2.3 CT**

X-ray computed tomography (CT) is a method used to obtain information of the internal structure of an investigated object. It is a non-destructive technique to reconstruct an object in 3D based on a set of 2D projections. The 2D projections are obtained by placing the object, for this research a cylindrical rock sample, on a rotating stage in between an X-ray point source and a detector as illustrated in figure 5. X-rays have wavelengths below 10 nm which is smaller than those of visual light (0.4 – 0.7  $\mu$ m). Therefore the details which can be observed with them are smaller than those observed with a microscope. However in practice the resolution is limited because of other reasons (Vlassenbroeck, 2010).

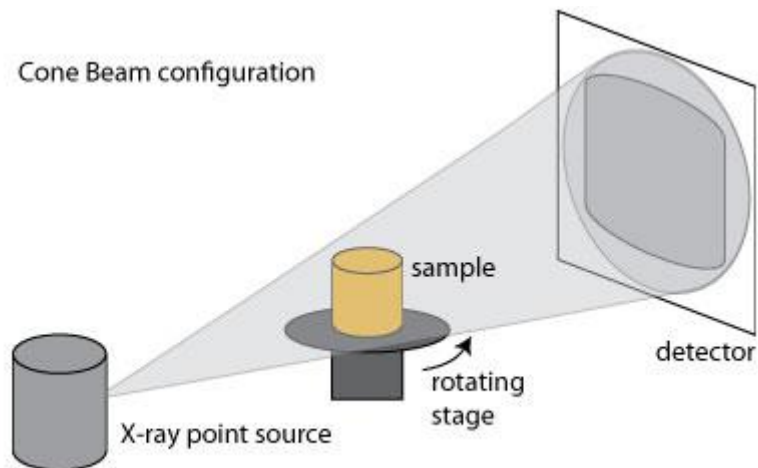


**Figure 5:** Sketch of the setup of a scan using a cone beam configuration. The sample is mounted on a rotating stage between an X-ray source and an X-ray detector. Depending on the size of the sample, it can be put closer to the source, resulting in a higher resolution. This figure is modified after Ketcham (n.d.).

The Centre for X-ray Tomography of the Ghent University (UGCT) does intensive research on the improvement of both hardware and software for high-resolution X-ray CT. The scanners are fully constructed by UGCT, as well as the data acquisition and reconstruction software packages (Vlassenbroeck, 2010; Brabant et al., 2011). Due to the cone beam of the X-ray source, the resolution will be higher when a sample is put close to the X-ray source. As a consequence small samples will be able to be scanned with a higher resolution than larger samples. Not only is the sample size important for the resolution, but also the resolution of the detector as well as the energy of the X-ray source. The higher the energy from the source, the wider the focal spot size will be which has a negative effect on the resolution. This is why downscaling of the sample size is important: not only will it be possible to put the sample closer to the source, the energy required to penetrate the sample will be less and thus the spot size will be smaller (Vlassenbroeck, 2010). At first the samples are scanned with a low resolution in order to obtain an overview of the internal structure. These samples have a diameter of approximately 40 mm and obtain a resolution of 60  $\mu\text{m}$ . From the field samples taken at Konusdalen and Crioceradalen, cylindrical samples were drilled with a diameter of 34 mm which obtained a resolution of 41  $\mu\text{m}$ . These scans are analysed for their internal homogeneity in order to select interesting areas for subsamples. Subsamples were taken using drill bits with internal diameters of 6 mm and 2 mm. The resolution obtained on the subsamples was 4  $\mu\text{m}$  and 2.7  $\mu\text{m}$  respectively.

### **2.3.1 Hardware and physical principles**

The X-ray source used for this research is that of the micro-CT scanner available at the UGCT. It is a medium energy scanner in which voltages up to 160 keV can be reached. The source is an open type X-ray tube in which electrons are emitted from a heated filament. The filament typically composed of tungsten, heats up to a temperature above 2700 K, resulting in emissions of electrons from the tip. Under high vacuum these go towards a positively charged anode which is cooled from the backside (Cnudde, 2011). The cooling is necessary because most of the energy of the electrons is converted into heat. To reduce the electron beam diameter between the filament and the anode, an electrostatic focusing cup or control grid can be used to focus the electron beam emitted from the heated filament and thus reduce the spot size. This is held at a negative potential  $-U_g$  relative to the

filament. This forces the electrons to focus in a beam since they are repelled by the grid. To further reduce the electron beam diameter, an additional electromagnetic focussing mechanism is added (Vlassenbroeck, 2010). The electromagnetic lenses, for this mechanism, two in the case of the Feinfocus tube, are assembled in the tube head. This can be removed in order to open the tube. In this way, filaments and targets can be replaced according to the application or upon failure. A vacuum system is continuously evacuating the tube since an open type tube is never sealed airtight. In figure 6, a schematic drawing from Vlassenbroeck (2010) is displayed in which the set-up of the open X-ray tube is given.

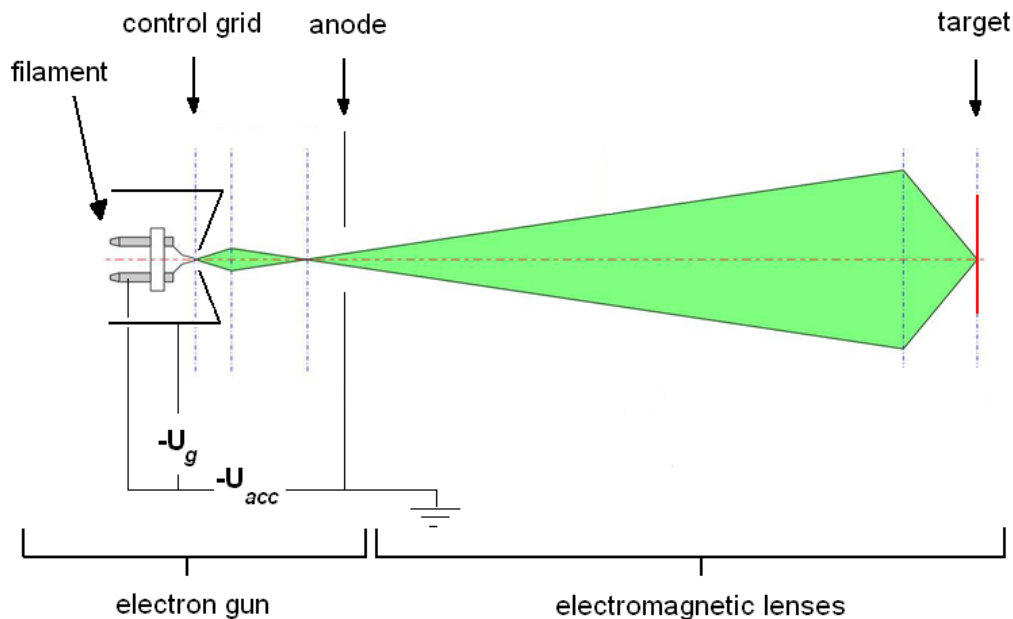


**Figure 6:** Schematic drawing of an open X-ray tube, from Vlassenbroeck (2010). A current  $I_f$  is sent through a tungsten filament which heats up. This results in emission of electrons which are accelerated towards an anode. The control grid, held at a negative potential  $-U_g$ , focuses the electron beam. The filament itself is charged negative ( $-U_{acc}$ ) relative to the anode. Between the anode and the target, or the end of the X-ray tube, two electromagnetic lenses focus the electron beam.

The X-rays form a cone configuration (figure 5) when leaving the X-ray tube after which they interact with the sample placed on top of a rotating stage. There are two types of photon interactions with material that are of high importance for X-ray CT setups: photoelectric absorption and Compton scattering. Photoelectric absorption occurs when the energy of an incoming photon is higher than the binding energy of a shell electron of an atom with which it interacts. The electron will then be knocked out of the shell of that atom while the atom completely absorbs the photon. This type of interaction occurs mainly at the inner shell electrons (Vlassenbroeck, 2010) and is strongly dependent on the atomic number of the atom with which the photons interact since the binding energy of the shell electrons depends on the atomic number. Therefore, low-energy X-rays are used to study light elements while heavy elements need to be penetrated by high-energy X-rays. Compton scattering on the other hand occurs when the energy of the photon is considerably higher than the binding energy of the shell electrons. The interaction between the photon and the shell electron results in the photon giving part of its energy to the electron, making it recoil. The photon is not absorbed, but is emitted in a different direction from the original, containing the remaining energy of the photon-electron collision. Because of the deviation of the photons from their original trajectory, Compton scattering is undesirable in imaging. For this type of interaction, the (average) atomic

number of the penetrated matter is not the most important factor since it is almost independent of the material. Another type of scattering that occurs to some degree for low energies is Rayleigh scattering. This is the elastic scattering of photons by the whole electron cloud of an atom. The electrons start oscillating due to the interaction with the photons and the particle becomes a small radiating dipole. In this elastic process, almost no energy is lost by the photons. However at low energies and when heavy elements are penetrated, the scattering angles can be significant. One last interaction process of photons with matter is not relevant in micro-CT. It involves photons with energies above 1.022 MeV that are absorbed, resulting in the production of an electron and positron. This type of interaction is called pair production. When the energy increases even more, the photons can interact with the nuclei of the atoms while emitting protons, neutrons or charged particles. However, the X-rays used in micro-CT rarely exceed energies of 200 keV, thus the latter type of interaction is of no interest in micro-CT analyses.

The most frequently used detector system in micro-CT is indirect X-ray detection. Incident X-rays interact with a scintillating material at the surface of the detector. In the Varian PaxScan 2520V detector used for the scans taken for this research, the scintillator is thallium doped caesium-iodide (Vlassenbroeck, 2010). This is an inorganic scintillator, grown in a columnar structure. Incident X-rays are absorbed in the crystals and the resulting light is brought to the detector surface through internal reflections at the crystal surfaces. The caesium-iodide is doped with thallium in order to ensure a light emission in the green spectrum. This matches the sensitivity of the photodiodes in the Charge-Coupled Device or CCD-sensors. Here it is converted to an electric signal, roughly proportional to the energy of the X-ray after passing through the sample. The detector resolution is dependent on the amount of scattering of light inside the scintillator, the field-of-view of the detector and the size of the individual CCD pixels.

Due to various ways in which emitted X-rays can interact with matter as described above, the intensity of the X-rays will decrease as they pass through matter. The transmitted intensity  $I$  of a monochromatic X-ray passing through a homogeneous object can mathematically be described by Beer's law:

$$I = I_0 e^{-\int \mu(s) ds}$$

Where  $I_0$  and  $I$  are the initial and final X-ray intensity respectively and  $\mu(s)$  is the local linear attenuation coefficient along the raypath  $s$ . The attenuation coefficient  $\mu$  is determined by the four interaction effects as described above, in which the two most important are the photoelectric effect and Compton scattering. Beer's law illustrates that due to these interactions, an X-ray beam with the initial intensity  $I_0$  will be exponentially reduced to intensity  $I$  when passing through a material with thickness  $s$ . Due to the fact that the sample is rotated between the X-ray source and the detector, a number of different angular projection images are made. By means of filtered back projection, the local value of attenuation  $\mu$  can be calculated. In this way each point inside the scanned volume can be characterized for the attenuation value, which will eventually lead to different grey values in the scanned images. Since  $\mu$  depends on the material density  $\rho$  and the atomic number  $Z$ , it can be plotted against the energy of the source for different minerals. This is illustrated in figure 7. In this figure the attenuation curves for six different minerals are plotted against the source energy. It concerns, from low attenuation values to high attenuations: quartz ( $\text{SiO}_2$ ), glauconite ( $(\text{K,Na})(\text{Fe}^{3+},\text{Al,Mg})_2\text{Si}_4\text{O}_{10}(\text{OH})_2$ ), calcite ( $\text{CaCO}_3$ ), apatite ( $\text{Ca}_5(\text{PO}_4)_3\text{OH}$ ) and pyrite ( $\text{FeS}_2$ ). As can be

seen in figure 7, the values for  $\mu$  for quartz and glauconite are lying close together. This is because the attenuation is proportional to the density and  $Z^3$  in the energy range typically used for CT (Attix, 1986; Knoll, 2000). In this,  $Z$  is the average atomic number of the mineral.

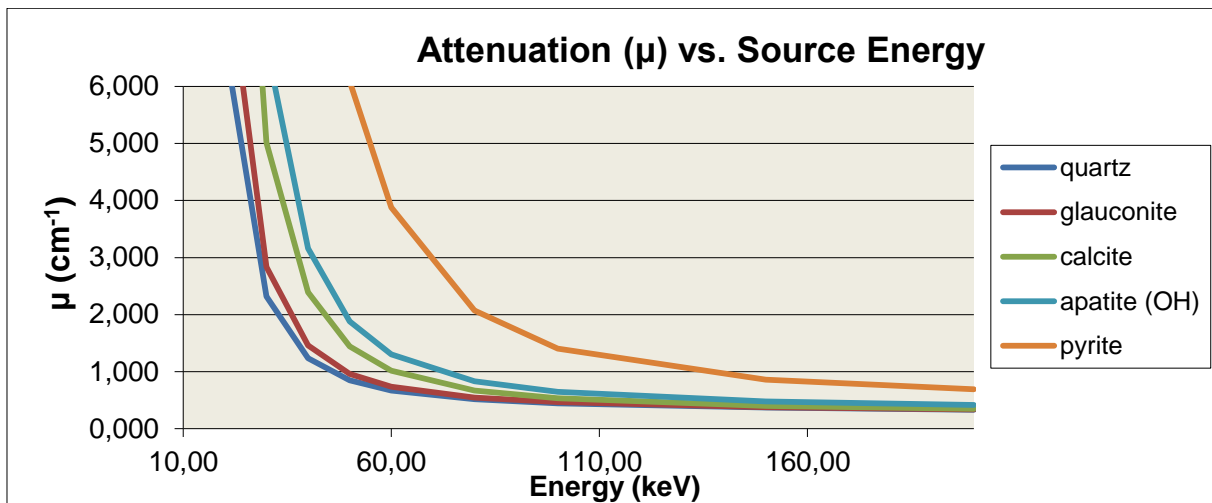


**Figure 7:** Graph plotting the attenuation ( $\text{cm}^{-1}$ ) of different minerals to the energy of the source (keV). The clearest differences between the different minerals are found in the area with source energies from 10 keV to 110 keV. This graph was constructed with the MuCalcTool, using the NIST XCOM database for the mass X-ray attenuation coefficients for minerals at <http://physics.nist.gov/PhysRefData/Xcom/Text/XCOM.html>.

### **2.3.2 Reconstruction of images**

The transformation of the obtained 2D projections into a 3D image is done in the reconstruction phase. In this stage the projections are transformed into cross-sections through the object by means of filtered back projection. This method combines different projections in order to reconstruct the attenuation values of single voxels (3D pixels) and is illustrated in figure 8c and 8d, from Greg (2001). It differs from simple back-projection, illustrated in figure 8a and 8b, because of the filter function that is added on the attenuation line. In this way, a star-burst pattern around each point in the image that degrades contrast and blurs the edges of objects as seen in figure 8b, is eliminated (Greg, 2001). However, because of the limitations concerning resolution when dealing with X-ray CT, all material boundaries are blurred to some extent (Ketcham & Carlson, 2001).

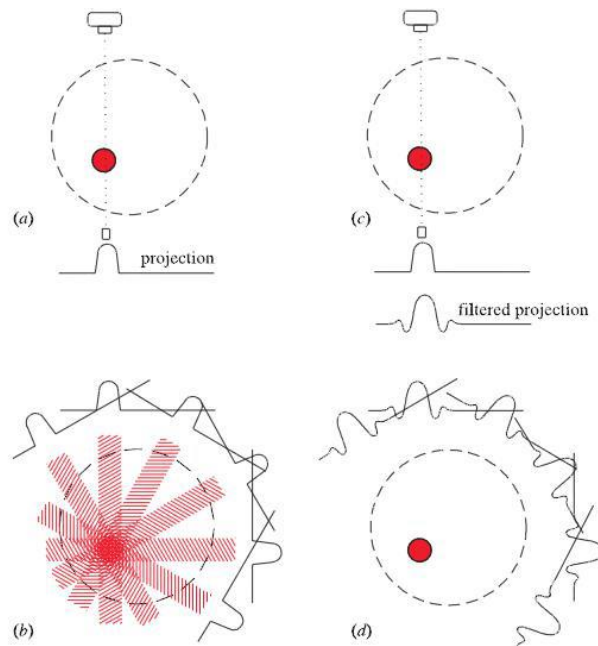


**Figure 8:** The principle of simple back-projection is illustrated in figure 8a and 8b. In figure 8b, the reconstructed point is surrounded by a star-burst pattern because the measured attenuation profiles (8a) are merely projected along the image plane. This is resolved thanks to a filter function (8c) added to the projection. The star-burst pattern is eliminated in figure 8d. This figure is from Greg, 2001.

The UGCT developed special software, named “Octopus”, to take care of this very computer intensive reconstruction process (Vlassenbroeck et al., 2007). By using this software, the images can be corrected for multiple possible errors such as a possible tilt or skew in the images due to the fact that the sample did not have a vertical position during the scan. A first step in the reconstruction is the so-called pre-processing. In this phase the 2D projections are corrected to remove acquisition-specific effects in the data before the actual filtered back projection can be done. Every scan is therefore accompanied by a number of open beam images or flat field images and dark images or offset images. Open beam images are images taken while the X-ray source is working, but the sample is absent; while dark images are images taken while the X-ray source is not working. The dark images are needed to correct for detector features and are subtracted from every projection image and open beam image. With the open beam images the projection images are normalized. This is a step which is necessary in order to correct for errors from within the X-ray source. For statistical reasons the open beam and dark images can be taken at different times during scanning, not only before and after the samples have been scanned but also during the scanning period of the sample. It is however only important when dealing with very high resolutions, or a long duration of scanning. Following the normalisation, a spot filter is applied. It is used to correct for overly dark and bright pixels in the images, resulting from direct X-ray impacts on the detector (Vlassenbroeck et al., 2007). Another pre-processing step which is necessary is the application of a ring filter. It tracks non-linearities from the detector pixel by pixel and removes them. If these are not removed, they would give rise to the formation of ring artefacts in the reconstructed cross-sections (Vlassenbroeck et al., 2007). As a last pre-processing step sinograms have to be generated. They contain the projection data of a single detector row for all normalised projections (Vlassenbroeck, 2010). All these operations can be implemented in one step in the program “Octopus”, however it is recommended to perform some of them separately in order to ensure that the correct reconstruction parameter are used. For all of the



reconstructed scans in this research, the normalisation and ring filter were applied together, while the spot filter and sinogram generation were carried out separately.

The next step in the process is the actual reconstruction. The obtained sinograms are processed via a filtered back projection algorithm after which a stack of cross-section is generated through the sample. In this algorithm, the sinograms are filtered once more with the so-called ramp filter. After this, the data of every projection angle is projected back to the object, in this way reconstructing the scanned sample. For the cross sections to be generated in a correct way, Octopus implements several parameter input options for the user. The first of these options concern the geometry of the scan. One can determine: the precise rotational axis of the sample, the amount of tilt and skew the sample had during scanning, the precise horizontal and vertical centre of the images and the correct distances from the source to the detector (SDD) and from the source to the object (SOD). These parameters are of high importance for the reconstruction, because if they are not adjusted correctly the obtained images will be blurry.

After adjusting the parameters concerning the scanning geometry, one can adjust the quality of the images. To do this, a noise filter is implemented. A bi-linear interpolation algorithm compares the attenuation of individual pixels to these of their neighbouring pixels. The noise filter can be set from 0% to 100% and for the reconstructions of scans in this research values of 40% to 70% were generally used. Another important parameter in the quality reconstruction is the correction for beam hardening. This is an effect in which the centres of the reconstructed cross-sections seem to have a lower attenuation than the sides of the sample. Here the X-rays had to penetrate further into the sample which will lead the detector to record a higher energy spectrum which corresponds to a lower average attenuation coefficient (Brooks & Di Chiro, 1976). The beam hardening effect can be avoided by using hardware filters, like an aluminium plate placed in between the X-ray source and the scanned sample, but when it is still present an algorithm exists in Octopus which corrects for this effect. In Octopus one can insert different values for the beam hardening correction and assess the correction factor via a vertical or horizontal line profile through the cross-section in which the attenuation values along this line are shown. When these values can be fitted by a horizontal trend line, the beam hardening correction factor is correct.

In the Output subdivision of Octopus, one selects the type of files in which the data should be saved. The options are 8 bit files, 16 bit files or 32 bit files. Once reconstructed the attenuation values of every voxel will be remapped to integer values. Therefore it is important to know which type of file to choose. An 8 bit file can hold an integer value up to 255 while a 16 bit integer can be up to 65535 and a 32 bit integer up to  $2^{32}$ . It is advised to choose the 16 bit files in order to have a large enough range of grey values. One can also adjust the contrast of the reconstructed cross-sections by changing the original grey values, used by Octopus. A last correction factor added in the software is one for ring artefacts which can be still present after the pre-processing. Once all of the correction factors are filled in, the entire volume can be reconstructed.

### **2.3.3 Analysis**

Once the scan is reconstructed the images can be analysed using the software developed by UGCT called "Morpho+" (Vlassenbroeck, 2010). In this toolkit the CT images of the rock sample can be analysed in 3D. Before starting, Morpho+ offers a selection of noise filters. If necessary these can be

used, but since similar noise filters are already implemented in the reconstruction phase this step can often be skipped. Then the volume of interest (VOI) can be selected by defining a circular or rectangular region in one of the cross-sections of the image stack. This selection is then propagated over the other cross-sections. It can be interesting if the user plans on analysing only a part of the volume of the scan. In this way irrelevant data which would give rise to wrong results are discharged. In this research for example, the porosity distribution in the sample is an important feature. To analyse it, the air outside the sample has to be discharged.

Once the VOI is defined, different minerals as well as the porosity can be separated, or thresholded, based on the different grey values, resulting from different X-ray attenuations. During thresholding, voxels are categorized as foreground or background voxels depending on whether or not their grey values lie within a certain interval. Thresholding can be carried out automatically, but this often fails when applied to real data. Therefore manual selection and evaluation of the threshold values is the recommended strategy to obtain correct results. Morpho+ provides the option of dual thresholding in which a weak threshold and a strong threshold value are chosen. This is based on the difficulty in identifying voxels as objects or as background based solely on its grey value. The voxels with a grey value lying between that of the weak and strong threshold value will be categorized as foreground voxels only when they are connected to one or more voxels that satisfy the strong threshold value. In this way the sensitivity to residual noise is reduced. If the thresholding is carried out, the foreground voxels form a mask on top of the original image. To remove white or black voxels which have been wrongly labelled, different morphological operations can be performed. For example, one can remove isolated background or foreground voxels, expand or shrink the mask with a number of voxels, invert the mask and many other options are available.

Once the different components such as porosity, clay, quartz grains, etc. are thresholded, they can be labelled as objects. In this study the main focus lies on the porosity of the rocks so mainly this will be what is labelled. Because of connections inside object it is often necessary to separate them in different subcomponents. To do this, first an euclidean distance transform is calculated for the objects. For every foreground voxel of an object, the euclidean distance to the nearest border voxel is calculated. This is also used when calculating the maximum opening of objects. It is defined as the diameter of the maximum inscribed sphere fitting inside the object. Following the distance transform is a watershed segmentation. This segmentation method can be compared to the filling of the objects with water so different catchment basins will form in the objects. With an increasing water level, the water from different basins will meet. Where they meet, watersheds are formed. The original object will be separated along these watersheds so that each catchment basin will define a new object. These separated objects can then be characterized quantitatively by several parameters. One can obtain the volume of the separated objects in relation to the volume of interest, which is called the total porosity, whether or not the labelled objects actually represent pores or another material. A distinction can be made between objects which are connected to the border and those which are not by calculating the open and closed porosity. If the sample has a heterogeneous distribution of the porosity, or any other material which can be labelled as a separate object, the partial porosity is a useful parameter to describe the distribution of this material in different chosen blocks of the sample. These can be defined in any direction (X, Y or Z). For each individual object following parameters can be extracted: the maximum opening, as described above; the equivalent diameter, which is the diameter of a sphere with the same amount of voxels as the object; the sphericity, which is defined as the ratio of the maximum opening and the equivalent diameter and gives an

approximation of the shape of objects; and the orientation of the equivalent ellipsoid in which the object is modelled as an ellipsoid from which the orientation in the sample can be calculated. All these analysis results are written to a spreadsheet, together with additional information such as the voxel size and information about the construction of the volume of interest. For each object, the binary data and distance map can be exported, allowing further visualization in different computer programs, or to reload them into Morpho+ for further analysis.

Specifically for analysis of fractures within the samples a Multiscale Hessian Fracture Filtering (MSHFF) script in the program "Fiji" is used. This script, developed by Voorn et al. (2013), allows segmentation of narrow fractures in 3D image data without also thresholding porosity which is the case if they would be thresholded in Morpho+. In this script, one must specify the minimum and maximum pixel width of the fractures of interest, as well as the average and maximum material greyscale value, excluding the fractures, and the conservative threshold value of the fractures which estimates the greyscale value present in them. These are all parameters which can be extracted from analysis of the cross-sections using Fiji. The MSHFF script divides the data set in a given number of blocks (blocksize) according to the available RAM memory for the calculation, the number of cross-sections in the data set, the width and height of these cross-sections expressed in pixels and the maximum width of the fractures. If for the blocksize a value higher than the amount of cross-sections is given, the blocksize has to be defined as the number of cross-sections. In a defined region of interest, the script then starts its search for fractures and segments these from the sample material with the use of a mask of foreground pixels. These are not binary and thus have a variance of greyscale values. After this, a calibration of the segmented fractures is often necessary. To do this, two values are required in order to simplify the mask: a lower cut-off for noise and an upper cut-off for "maximum porosity", which is the last threshold value before the minimum width of the fractures, as defined previously, gets too wide (Voorn et al., 2013). In order to define this value, control lines were added to the cross-sections with widths from the minimum fracture width to the maximum fracture width. One must threshold these control lines so that every line has the correct width. The threshold value which is obtained in this way is then used as the upper cut-off value. After calibrating, the obtained images are saved and can be exported to Morpho+ to be labelled as individual objects. Figure 9 gives an impression of the fracture segmentation before and after calibration. In Morpho+, the fractures within a sample can subsequently be described with regards to their opening and orientation. With the program "3D Viewer", developed by the UGCT, stereographic projections can be made out of the exported objects from Morpho+. These are useful in order to evaluate trends in object orientations and are specifically used in this research to plot the orientations of segmented fractures.

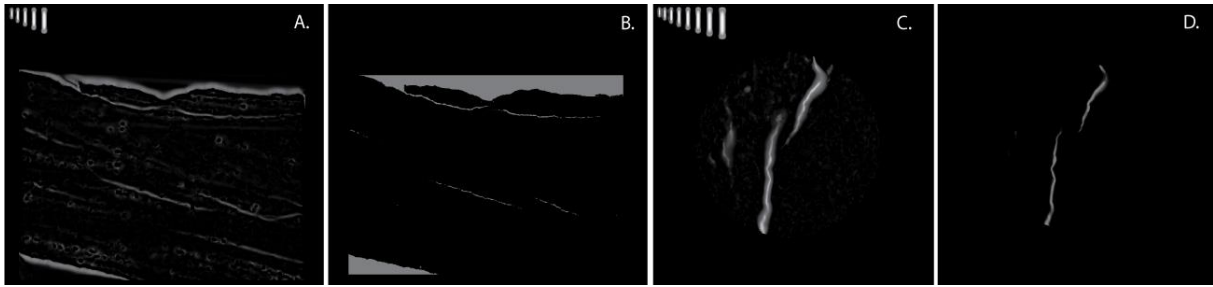


**Figure 9:** Comparison between non-calibrated fracture segmentation (a and c) and calibrated fracture segmentation (b and d). Figures 9a and 9b are images taken during fracture segmentation of sample T2. In this sample the fractures were first segmented in the X-plane after which the images were converted to the Z-plane. In figures 9c and 9d fractures in sample T5 are segmented in the Z-plane.

Although the program “VGStudio MAX®” can also be used to reconstruct and analyse CT data, at the UGCT it is mainly used to render the rock samples and the exported objects in 3D. This is because Morpho+ was specifically designed to be user-friendly and have a performance and coding flexibility in order to be able to add extra functionalities when desired. VGStudio MAX® however uses the scan data and analysis results in order to create a 3D model of the volume. This can be displayed in 3D or in 2D slice images. It is also possible to visually cut into a volume in the 3D display area. When this option is used, one can for example visualise the distribution of certain segmented objects in the entire sample. There are also different types of light sources available from which one can choose and form combinations. Depending on the rendering method, realistic shadows can be added in the 3D view.

## **2.4 Rock modelling**

A numerical model of the rocks can be made based upon the 3D images analysed in Morpho+. The program used to do this is “E-core”. Starting from the existing 3D image in which the porosity is labelled as such, the pore network can be extracted. As a result of simplifying the labelled porosity, a skeleton of the pore space is made. This skeleton is defined as a set of voxels at equal distances from two or more points of the solid material (Bakke & Øren, 1997). It is thus extracted by an ultimate dilation of the solid grains followed by detailed measurements along the obtained skeleton. The combination of the voxels at equal distances of the solid material gives centre lines as a spatial representation of the pore network. Two or more lines meet at the centre of pore bodies and form the network nodes. They are connected to other nodes via links called pore throats. The pore nodes and throats forming the pore network can easily be represented by a ball-and-stick model. In this simplification of the network following statistical parameters are calculated: the maximum inscribed radius in pore bodies for volume calculations; the minimum inscribed radius in the pore throats for drainage capillary pressure and hydraulic conductance; and the pore shapes for describing the simultaneous flow of two or more fluids in one pore (Bakke & Øren, 1997).

Using E-core this simplified network can be used to compute rock and fluid flow properties. This is based on the fact that several macroscopic properties of rocks, such as absolute permeability, capillary pressure and relative permeability, are determined by the microstructure of the rocks themselves and the fluids occupying the pore space. Some of these properties, such as the absolute permeability, are determined by numerically solving differential equations directly on the virtual rock. In order to minimise boundary effects, the calculations of the permeability are performed on a central region of the pore network. On a fully saturated network, a constant pressure drop  $\Delta P$  is

established across the network. For this pressure drop the flow rate  $Q$  of a fluid with permeability  $\mu$  is calculated. The permeability  $K$  is then determined from Darcy's law as explained in chapter "2.1 Laboratory characterization". For these simulations a lattice Boltzmann (LB) method (Ramstad et al., 2010) is used to characterize the fluid flow. The fluid particles in a LB model move and interact on a regular lattice with very limited degrees of freedom. Detailed descriptions of the LB method and possible lattices can be found in Succi (2001) and Chen & Doolen (1998). In spite of the limitations of fluid particle movement, the LB model can closely mimic typical experimental setups. However, these calculations are so computer intensive that it has to be carried out by a supercomputer. At the University of Ghent the High Performance Computing (HPC) Team offers a supercomputing environment. A total of six computer clusters are available and on one of them (Gengar, with 156 computing nodes) these calculations are carried out.

Other properties, such as relative permeability, are performed on a simplified model of the pore space (ball and stick model), which is less computer intensive so they don't need to be calculated on Gengar. The relative permeability is the permeability measured at a specific fluid saturation and is expressed as a fraction of the total or absolute permeability. When there is only one fluid phase present in a rock sample, the relative permeability in that rock is thus 1. Therefore relative permeabilities are determined from multiphase flow simulations. There are several assumptions that are used when simulating multiphase flow (Bakke & Øren, 1997): the flow is laminar in every point, with all the fluids as Newtonian, incompressible and immiscible; the pores, as defined by pore bodies and pore throats can be occupied by one or more fluids simultaneously; non-wetting fluid is the bulk fluid while wetting fluid is retained as films in the corners of pore bodies and throats; fluid pressures are only defined in pore bodies, which are considered to be large enough for the capillary pressure across an invading interface in the pore body to be negligible; when occupied by one bulk fluid pore bodies are called full as where those occupied by two bulk fluids are characterized as interface nodes. The multiphase flow simulations are based on capillary dominated drainage displacement of fluids. They start with the ball-and-stick model of the porosity from which the open porosity is filled with water which acts as a wetting phase. After this there is a primary drainage with a non-wetting fluid. As a standard in E-core this is oil, but the properties of the fluid can easily be adjusted to those of liquid  $\text{CO}_2$ , with a density adaptable to the injection depth, pressure and temperature. E-core gives a visual and statistical representation of the amount of pores which is now filled with water, trapped during the primary drainage, and the non-wetting fluid representing liquid  $\text{CO}_2$ . What follows is a secondary drainage, filling the open porosity again with water. Now a statistical and visual representation is given of the pores filled with water trapped during the primary drainage, trapped  $\text{CO}_2$  and water filling the pores after the secondary drainage. It is very important to pay attention to the scale of the sample since E-core will only use the largest pore clusters to determine the relative permeability. An increased resolution will thus lead to a better estimate of the relative permeability in relation to, for example, the porosity within a rock.

Another experiment which can be simulated with E-core is the Mercury Injection Capillary Pressure (MICP) analysis which otherwise is a destructive test. The setup of the experiment is illustrated in figure 10: the sample of interest is placed in a chamber (figure 10a) which is flooded with mercury (figure 10b). During the approximately 3 hours during experiment, the pressure on the mercury is incrementally increased. In this way mercury is forced through progressively smaller pore throats (figure 10c). At the end of the experiment, pores which are accessible through pores as small as  $36 \text{ \AA}$  ( $1 \text{ \AA} = 1.0 \times 10^{-10} \text{ m}$ ) are intruded. The volume which is forced into the sample is equivalent to the

pore volume of the sample. To constitute the pore size distribution of a sample, mercury volume measurements are carried out after each incremental increase of pressure. Because the pressures can be related to pore throat sizes, pore size distributions can be made in this way. This method is especially very useful for determining porosity distributions in samples with low porosities and very low permeabilities, making it difficult for the distribution to be analysed in another way (Olsen & Grigg, 2008).

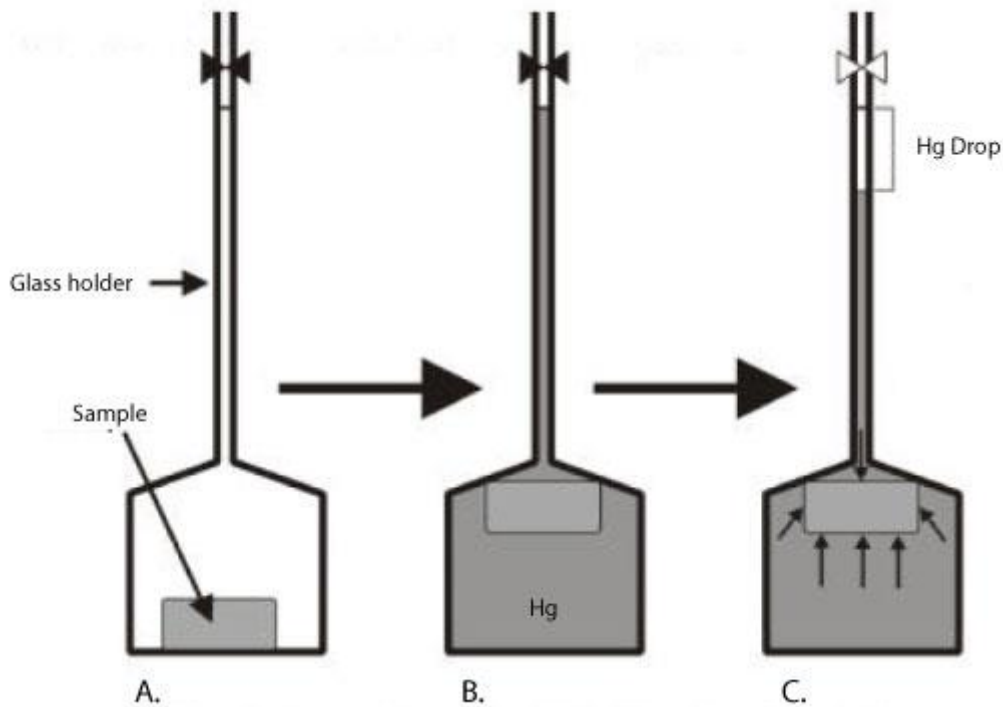


**Figure 10:** Experimental setup for the MICP test: the rock sample of interest is placed in a chamber (a), which is then flooded with mercury (b). The pressure in the chamber is subsequently increased after which mercury is forced in the sample. This gives a drop in the level of mercury, which can be measured through a glass holder (c). This figure was modified after a 'Formation Evaluation' Masters course notes from Glover (2001).

In table 1 a summary is given of all physical rock properties as well as the overall rock characteristic and transport properties that can be computed in E-core starting from CT-data provided that some extra information is added. For example the characterization of grain types is a result of earlier segmentation and labelling of different grains in Morpho+ or another CT-data analysing program

**Table 1:** Physical properties, transport characteristics and rock characteristics that can be computed from 3D digital rocks. Table from Cnudde (2011).

<p><i>Physical Properties</i></p> <p>Porosity (total, effective, and non-connected)</p> <p>Absolute permeability (matrix and fractures) in x-y-z directions</p> <p>Elastic properties in x-y-z directions</p> <p>Formation factor (resistivity) in x-y-z directions</p> <p>Mechanical strength</p> <p><i>Fluid flow characteristics (two-phase flow simulations)</i></p> <p>Relative permeability in x-y-z directions</p> <p>Capillary pressure</p> <p>Irreducible water saturation</p>
---

Residual oil saturation  
Oil-water wettability

Rock characterization

Grain type distribution (quartz, feldspar, carbonate, clays, etc.)  
Surface area and volume of grains  
Pore size distribution  
Grain size distribution  
Grain sphericity and roundness  
Clay mineralogy analysis  
Total organic carbon content (connected and non-connected)  
Silt fraction  
Bedding plane orientation  
Geologic setting and origin of the rock

## **2.5 Summary of the methodology per sample**

In table 2a and table 2b an overview is given per sample of the work that has been carried out. In the tables the samples are listed according to their altitude, so the field samples are listed first in table 2a, followed by those from Dh4 and then the samples taken from Dh2, together in table 2b. As can be read from table 2a, porosity measurements were performed on all samples except for S4 and S1. For S4, sample S7 which was taken at Criocerasdalen can substitute. They both are conglomerates with an iron-rich matrix from the Brentskardhaugen Bed. The porosity of S1 was not measured because T3 can substitute for it. T3 was taken at exactly the same location, 8 days after sampling S1. This second day of sampling was necessary in order to take larger samples which are easier to drill. The field samples were taken in order to compare their results to the results obtained from the samples of the drill cores. The field samples are much more fractured due to weathering so fracture analysis will be important for these samples. Only the field samples were used in order to make thin sections. Thin sections were made from the following field samples: T1 to T5, S3, S6, S7 and S8. They were subsequently etched and stained on one side of the thin section with Alizarin red S in order to stain calcite and aragonite; and on the other side with Potassium ferricyanide in order to stain iron-rich dolomite and calcite. Siderite will not react with Potassium ferricyanide and will thus not be stained.

Four samples, all from Dh4, were sent to PanTerra Geoconsultants B.V. (The Netherlands) for permeability measurement. From these samples, C1 is the only sample from which a target value is known from previous studies. This target value is 0.247 mD which was measured at the Petroleum Laboratory of Sintef Petroleum (Braathen et al., 2012).

**Table 2a:** Overview per sample of the work that has been carried out on the field samples.

Sample	Location	Altitude (m)	Poro.	Perm.	Thin sect.	Scan 1	Scan 2	Scan 3	E-core
S8	Criocerasdalen	150	X		X	X			
S7	Criocerasdalen	149.5	X		X	X	X		
S6	Criocerasdalen	149.4	X		X	X			
T5	Konusdalen	91.0	X		X	X			
S5	Konusdalen	90.8	X						
S4	Konusdalen	90.5							
S3	Konusdalen	85.1	X		X	X			
S2	Konusdalen	77.7	X				X		
T4	Konusdalen	75.1	X		X	X			
T2	Konusdalen	74.1	X		X	X	X		
T3	Konusdalen	71.9	X		X	X	X		
S1	Konusdalen	71.9							
T1	Konusdalen	69.8	X		X	X	X		

**Table 2b:** overview per sample of the work that has been carried out on the core samples.

Sample	Core	From (m)	To (m)	Poro.	Perm.	Thin sect.	Scan 1	Scan 2	Scan 3	E-core
C9	Dh4	-671.92	-672.00	X			X			
C8	Dh4	-674.48	-674.56	X	X		X			
C7	Dh4	-677.12	-677.20	X	X	X	X	X		X
C6	Dh4	-680.94	-681.00	X			X		X	X
C5	Dh4	-687.10	-687.12	X						
C4	Dh4	-689.64	-689.70	X			X		X	
C3	Dh4	-691.00	-691.08	X	X		X	X		X
C2	Dh4	-693.96	-694.00	X		X	X			
C1	Dh4	-695.22	-695.28	X	X		X	X		X
D1	Dh2	-736.73	-736.81	X			X	X		
D2	Dh2	-741.67	-741.72	X			X		X	
D3	Dh2	-752.30	-752.38	X		X	X	X	X	

Scans were carried out at samples with 3 different sizes. First of all large samples, with a diameter of 34 mm to 40 mm were scanned with a resolution ranging from 41  $\mu\text{m}$  to 56  $\mu\text{m}$ . These scans were executed for all samples with the exception of: S1, for which T3 can substitute; S2 which was a too small sample for drilling a cylinder with a diameter of 34 mm; S4 and S5 for which the analogue samples S7 and S8 taken at Criocerasdalen can substitute and C5 which was too small. In table 2 these scans are brought together under the title "Scan 1". After this, subsamples were taken with a diameter of 6 mm and scanned with a resolution of 4  $\mu\text{m}$ . For the field samples T1, T2, T3 and S2 this was done in order to have a look at the faults inside them specifically; while for the samples from Dh2 and Dh4 a more general view of the porosity was given. The scans with a resolution of 3.99  $\mu\text{m}$  are brought together under the title "Scan 2" in table 2. After some first scans at this resolution samples C1, C3 and C7 were analysed in E-core. The MICP data, gathered in E-core showed that the resolution still was not high enough for accurate analysis of the porosity. Thus some samples were selected to drill subsamples with a diameter of 2mm. These were subsequently scanned with a resolution of 2.8  $\mu\text{m}$  and analysed using E-core. Analogous to the previous scans, scans with this resolution are named "Scan 3" in table 2.





### **3. Results**

#### **3.1 Field work**

The field work took place from 8 June 2012 to the 18<sup>th</sup> of June. This period started with mandatory safety training necessary for moving out of Longyearbyen to have a look at the outcrops. The trip from Longyearbyen to the outcrops was made three times spread over three days. To give an impression of the field figure 11 is inserted below. It shows Professor Dr. Snorre Olausen (in red) and myself (in blue) walking in Konusdalen towards the first outcrops.



**Figure 11:** A picture taken by Drs. Tim De Kock, at the first day of field work (10<sup>th</sup> of June 2012) in Konusdalen while walking alongside the outcrops of the Wilhelmøya Subgroup. In the distance the inner Isfjorden is visible as well as the mountains on the other side of the fjord.

Two of the days the field work took place in Konusdalen where a succession of rocks from the Wilhelmøya Subgroup of approximately 15 m thick was described and sampled in detail. The other day of actual field work was carried out in Criocerasdalen. In this valley to the east of Konusdalen rocks of the Brentskardhaugen Bed are found in outcrop. The work carried out during these three days in the field resulted in the composition of one litholog which combines the observations in Konusdalen and the Brentskardhaugen Bed in Criocerasdalen. A total of 13 samples were taken in the field. These are labelled S1 to S8 and T1 to T5. The T-samples were taken during the second day at Konusdalen with the purpose of taking large samples of interesting sections. The same location as where S1 was sampled for example was sampled in more detail later, resulting in sample T3. The same facies from samples S4 and S5, taken at Konusdalen, were also sampled at Criocerasdalen during the second day of field work; so these samples can be substituted by S7 and S8 respectively.

Two other lithologs were subsequently made from the sections of the Wilhelmøya Subgroup taken from the available cores from Dh2 and Dh4. In Dh2, 60 m of core were described from which 23 m is part of the Wilhelmøya Subgroup. Another 102 m from Dh4 were described from which

approximately 25 m is part of the Wilhelmøya Subgroup. From the section in Dh2 3 samples were taken (D1 to D3) and from Dh4 9 samples were taken (C1 to C9). Figure 12 shows the three lithologies with sample localization and the correlation between Dh2 and Dh4.

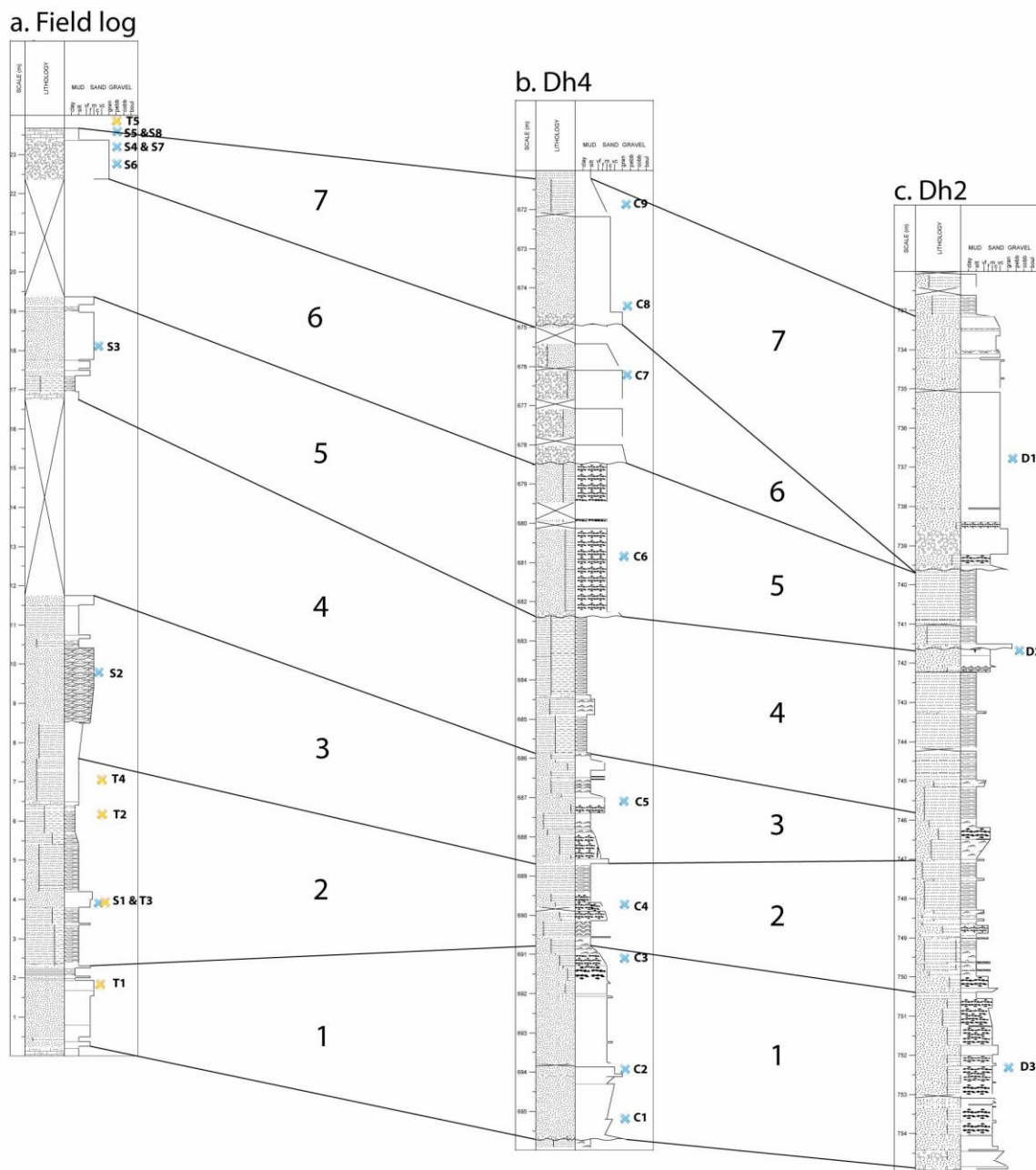


**Figure 12:** Three lithostratigraphic logs as a result of the field work that has been carried out. Figure 12a is the litholog as a result of the combined work at Konusdalen and Criocerasdalen; figure 12b represents the litholog of Dh4 from 671m to 696m deep and figure 12c is the litholog of Dh2 from 732m to 755m deep.

As can be seen on figure 12, the thickness of the Wilhelmøya Subgroup as found in outcrop is not comparable to the Subgroup identified in Dh2 and Dh4. On the field, there were two gaps in which rocks in situ were missing. These gaps were approximately 3 to 5m thick and reflect the significant lateral variations typical for the Wilhelmøya Subgroup in Western Spitsbergen. The fact that some parts are missing on the field does not mean that the field and the cores from Dh2 and Dh4 cannot be correlated. In spite of lateral variations this is still possible thanks to some distinguishable



horizons. Within the cores of Dh2 and Dh4 some sections are missing due to previous sampling for research purposes, but it is at most 20 cm. In both Dh2 and Dh4 the Wilhelmøya Subgroup is 20 m to 25 m thick and therefore very condensed compared to the type section at the island Wilhelmøya where it is 109 m thick in the stratotype.







The different correlated sections in figure 12 are numbered from 1 to seven in order to describe them. Section 1 ranges from a depth of 754.90 m to 750.00 m in Dh2 and from 695.70 m to 690.80 m in Dh4. In Dh4 the section starts with an erosional surface above which a thin conglomerate bed is deposited. This is followed by a coarsening upwards sequence of homogeneous sandstones. This sequence ends with a conglomerate bed at a depth of 694.10 m. In Dh2 the same sequence can be found, but more condensed, ending with a conglomerate bed at a depth of 754.45 m. Following both conglomerate beds in both Dh4 and Dh2 are fine sandstones interrupted by several coarse levels. They are partly (Dh4) or fully (Dh2) characterized by flaser bedding. This is a cross-bedding with numerous intercalated mud flasers (Reineck & Wunderlich, 1968) and the origin of this bedding type is related to the alternation of current or wave action and slack water. In the field, the section is represented by heterolithic sandstones which are bioturbated and hold several siderite nodules. Section 2, from 750.00 m depth in Dh2 to 747.04 m and from 690.80 m to 688.68 m in Dh4, is predominantly characterized by siltstones with horizontal to wavy bedding. These are interrupted by several levels with an increased amount of sand. Depending on the ratio of silt and sand, flaser bedding or lenticular bedding can be distinguished in these levels. In lenticular bedding, the silt forms the base material in which sand forms lenses or ripples that may or may not be connected (Reineck & Wunderlich, 1968). In the field there is a similar distribution of facies. The siltstones have horizontal bedding and the sandstone layer found between them is mineralogically immature. This sandstone layer appears to be a drainage layer along which water exits the outcrop. Therefore sample S1 and T3 were taken here. The third section represents a sequence consisting of sandstones and siltstones which are in Dh2 related to each other via a coarsening upwards sequence and in Dh4 by three successive fining upwards sequences. The silt is found in flaser bedding in the sandstones while the sand is found in lenses in siltstones, thus constituting a lenticular bedding. In the field this section consists of fine to medium grained sandstones, part of a coarsening upwards sequence. In a 2 m thick sandstone layer there are clearly identifiable wave ripples. Section 4, ranging from 746.00 m to 741.62 m deep in Dh2 and from 685.86 m to 682.35 m in Dh4, represents a succession of horizontal bedded siltstones which are sparsely intercalated by layers in which the sand content is elevated. These are characterized by a lenticular bedding. In Dh2, this section ends with the presence of nearly vertical fractures filled by secondary minerals. It is from this part of Dh2 that sample D2 was taken. This section is missing in the outcrops at Konusdalen. The transition from section 4 to section 5 can be found in both cores as an erosional surface followed by the presence of conglomerate layers. In Dh2, the conglomerates show notable large sandstone clasts, resembling sandstones as found below the erosional surfaces. These sandstone clasts are strikingly larger than the other clasts in the conglomerate, indicating a close provenance. In Dh2, the approximately 10 cm thick conglomerate layer is followed by horizontally bedded siltstone until a depth of 739.60 m. In this succession a layer can be found at a depth of 740.94 m made out of pyrite nodules. In Dh4 the conglomerate is followed by a succession of sandstones which are bioturbated and have silt incorporated in flaser bedding. These two different successions in Dh2 and Dh4 however are correlated due to the fact that they both start with an erosional surface on top of a lithology they obviously share (section 4) and due to the shared thickness of the initial conglomerate layer. The different successions on top of the

conglomerate layer can be explained by lateral variations. In the field the conglomerate layer, as well as the erosional surface is missing. However, the section starts with a siderite layer which is an indication of a condensation event (Gómez & Fernández-López, 1994). This is then followed by a silty clay shale of 40 cm thick after which iron rich, bioturbated sandstones are deposited with horizontal and vertical burrows. Section 6, only found in Dh4, starts with an erosional surface which is followed by a 3.52 m thick succession of conglomerates. The conglomerates in this succession are part of a fining upwards sequence in which the amount of sand as matrix gradually increases while the amount of clasts decreases. The last section starts with an erosional surface in both Dh2 and Dh4, followed by a conglomerate layer. In Dh2, this continues as a sandstone package with flaser bedding after which it is again followed by a conglomerate layer, this time without an erosional surface. What follows is very coarse grained sandstone with greenish sand grains. This is sparsely intercalated by thin mud layers. At a depth of 733.10 m the sandstones abruptly turn into siltstones with horizontal bedding. This is where the Wilhelmøya Subgroup ends in Dh2. In Dh4 the conglomerate is followed by coarse grained sandstones with an iron-rich matrix. From a depth of 672.00 m onwards there is a fining upwards sequence towards a siltstone package with pyrite nodules from 671.20 m onwards. This is where the Wilhelmøya Subgroup ends in Dh4. In the field, this section is represented by depositions of the Brentskardhaugen Bed. These 2 m thick conglomerates are directly followed by a chamosite layer and a siderite layer. Above these, the clays of the Adventdalen Group form the seal of the Wilhelmøya Subgroup reservoir.

The samples taken on the field are described in table 3. Although they were sampled at a different location, S5 and S8 are treated as one sample since they have the same facies. This is also the case for S4 and S7. For further analysis S8 and S7 were chosen. Therefore the pictures in table 2 also are those of S8 and S7. T3 was sampled at exactly the same location as S1 and therefore S1 and T3 are described once.

**Table 3:** Overview of the samples from the field section in which the sample is illustrated with a picture, the location and a facies description

Sample name	Picture	Location	Facies
T5		Konusdalen	Bioturbated medium sandstone which is very rich in quartz and has small burrows. The rock shows fractures along which enrichment in clays is noticeable.
S5 & S8		S5: Konusdalen S8: Crioceradalen	Chamosite-rich sandstones typical for the top of the Brentskardhaugen Bed. The chamosite occurs in the form of ooids and is probably formed as a result of storms (Maher, 1989).

S4 & S7		S4: Konusdalen S7: Criocerasdalen	Conglomerates with phosphatic clasts, quartz- and chert-clasts which are part of the Brentskardhaugen Bed. They are characterized by an iron-rich matrix. Like the chamosite in S5 and S8, the conglomerates are the result of storms.
S6		Criocerasdalen	Conglomerate, part of an iron-poor lens within the Brentskardhaugen Bed. This lens has got a length of approximately 6 m. The rocks below this lens are poor in clasts, while above it they are rich in chert-clasts.
S3		Konusdalen	Bioturbated medium sandstone with small burrows with a similar appearance as that of sample T5.
S2		Konusdalen	Medium sandstone with clear wave ripples as part of a coarsening upward sequence. The ripples consist of alternating sand-rich and mud-rich layers.
T4		Konusdalen	Sandy siltstone with wavy bedding, but no clear alternation between sand- and silt-rich layers.
T2		Konusdalen	Sandstone with elongated wave ripples consisting of mud-rich layers bedded in the sand-rich matrix. Along the mud-rich layers fractures are formed.





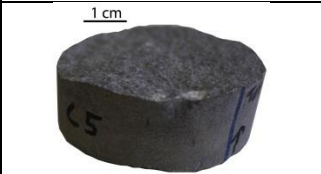



S1 & T3		Konusdalen	Greenish sand layer of approximately 3 m thick. In outcrop this layer tends to form a migration pathway for water. Clay-rich layers are present along which the sample tends to fracture.
T1		Konusdalen	Medium sand with wavy interbedding of clay. The clay-rich material seems to form a network of shafts which can be recognized as the ichnofossil "Thalassinoides".





Table 4 gives an overview of the samples taken from Dh4 and Dh2. These samples were chosen in such a way that there is a maximum in variety of facies, with the constriction that the samples are interesting as reservoir section within the Wilhelmøya Subgroup. Therefore they are chosen from the silt- to sand-rich intervals in both Dh2 and Dh4.

**Table 4:** Overview of the samples taken from cores Dh4 and Dh2 with for each sample a picture of the sample, the depth in the core and a short description of the facies which is present.

Sample name	Picture	Depth	Facies
<b>Dh4</b>			
C9		From 671.92m to 672.00m.	Claystone, part of the overlying cap rock sequence. Some black sand grains are incorporated in the sample
C8		From 674.48m to 674.56m.	Chamosite-rich sandstone.

C7		From 677.12m to 677.20m.	Iron-poor conglomerate.
C6		From 680.94m to 681.00m.	Medium grained bioturbated sandstone with a significant amount of clay-rich material in flaserbedding.
C5		From 687.10m to 687.12m.	Siltstone.
C4		From 689.64m to 689.70m.	Fine grained sandstone with a significant amount of clay-rich material in flaserbedding. In certain parts of the sample the flaser bedding becomes lenticular bedding in which sand lenses are found within the clay material.
C3		From 691.00m to 691.08m.	Sandstone with admixture of clay in flaserbedding.
C2		From 693.96m to 694.00m.	Coarse grained bioturbated sandstone with some clay-rich material.



C1		From 695.22m to 695.28m.	Medium grained sandstone with admixture of clay-rich material.
<b>Dh2</b>			
D1		From 736.73m to 736.81m.	Chamosite-rich coarse grained sandstone with some clay-rich material.
D2		From 741.67m to 741.72m.	Sandstone below erosional surface with vertical fractures and secondary mineralization.
D3		From 752.30m to 752.38m.	Sandstone with double lithology. The lower part of C3 is fine grained bioturbated sandstone while the upper part is very coarse grained sandstone. The transition between the two facies is sudden.

From Dh4 another 77 m were described which are not part of the Wilhelmøya Subgroup. They consist largely of the Upper Triassic De Geerdalen Formation, described from a depth of 770 m and partly from the Adventdalen Group laying above the Wilhelmøya Subgroup. Because the De Geerdalen Formation contains important sandstone sections, the succession from 770 m depth to the start of the Wilhelmøya Subgroup at 695.70 m will be described briefly. From 770 m to 764.50 m, the formation mainly consists of bioturbated fine sandstones with horizontal to wavy bedding and widespread pyrite nodules. These sandstones are interrupted by siltstone layers of 10 cm to 20 cm thick with horizontal bedding. In this 6 m thick section there are 5 horizons with syn-sedimentary

fractures. These can be found at a depth of 769.55 m, 769.30 m, 768.92 m, 767.36 m and 766.70 m. This interval rich in sandstones is part of a larger interval, reaching to a depth of approximately 800 m and was considered one of the potential intervals for CO<sub>2</sub> storage in the first phases of the UNIS CO<sub>2</sub> project (Farokhpoor et al., 2010). It has an average open porosity of 11 vol% and an average permeability of 0.03 mD and is rich in sandstones because the paleo-environment in which it was deposited is that of a flood tidal delta (Braathen et al., 2012). From 764.50 m to 752.35 m the De Geerdalen Formation consists of siltstones with sparsely distributed sandstone intervals of 5 cm to 10 cm thick. The siltstones are horizontally bedded and have significantly less bioturbation than the above mentioned sandstones. The pyrite nodules however are evenly distributed in the siltstones as in the sandstones lower in the section. Above the siltstone interval, a 6 m thick sandstone interval follows. In these sandstones the overall trend is one of fining upwards into a silty claystone. However, at a depth of 750.20 m, there is a coarsening upwards sequence from fine sandstone into conglomerate. This sequence has a thickness of 32 cm. In one of the fining upwards sequences, the sandstones are bioturbated and have syn-sedimentary fractures. This is found at depths of 747.45 m and 747.70 m. This short interval rich in sandstones ends at a depth of 746.50 m where a new interval of clay-rich siltstones begins. These are characterized by horizontal bedding alternating with ripple structures, which give rise to the formation of lenses filled in with silt or sand, cross laminations and other cutting relations within the rocks. At a depth of 735.80 m there is a syn-sedimentary fracture, as well as at 731.06 m and 731.60 m deep where the fractures are filled with sandy material. Fossils are found at the depths of 731.86 m and 730.92 m (shell fragments), as well as at a depth of 722.95 m and 722.50 m where plant fossils are found in the neighbourhood of a coal layer of 4 cm thick. Starting from a depth of 719.10 m, several coarsening upwards sequences can be found. They grade from silt to fine sandstone which are usually bioturbated. Siltstones are characterized by horizontal bedding, lenticular bedding or wavy bedding, as where the structures in the sandstone alternate between horizontal bedding and flaser bedding. This last section in which several sandstone levels occur ends at the depth of 695.70 m in an erosional surface which indicates the start of the Wilhelmøya Subgroup. The paleo-environment of the entire section from 764.50 m to 695.70 m is a lagoonal setting (Braathen et al., 2012).

In Dh2 a total of 60 m of the core was described, resulting in 37 m which is not part of the Wilhelmøya Subgroup. 5 of these 37 m are part of the De Geerdalen Formation. They consist of an alternation between two siltstone bodies and two sandstone bodies in which the siltstones are characterized by horizontal bedding and the sandstones by lenticular bedding. The other 32 m which are described are found above the Wilhelmøya Subgroup and are thus part of the Adventdalen Group which forms a seal. The lowest 7 m of this section is still characterized by the admixture of a significant amount of sand in the siltstones, resulting in wavy bedding alternating with lenticular and flaser bedding. This is then followed by a decrease in sand content and the siltstone is characterized by horizontal bedding. At a depth of 708.40 m the facies of the rock has shifted to a clay rich siltstone with horizontal bedding and this facies does not change up to the highest described point in Dh2 at a depth of 700 m. Within these rocks there are pyrite-rich beds, as well as a pyritised wood fragment.

## 3.2 Laboratory results

### 3.2.1 Open porosity

From the field samples a selection was made for the porosity measurements. S1 and S4 were not measured because they can be replaced by T3 and S7 respectively. The results for the other samples are expressed in the tables below. Table 5a lists the samples taken in the two valleys, while table 5b and table 5c give the porosities of the samples of Dh4 and Dh2 respectively.

**Table 5a:** Calculated open porosities of the field samples.

Sample #	$\phi$ (vol%)
T1	9,68
T2	5,13
T3	9,03
T4	7,00
T5	5,78
S2	7,85
S3	5,96
S5	7,26
S6	16,76
S7	4,47
S8	12,09

**Table 5b:** Calculated open porosities of the Dh4-samples.

Sample #	$\phi$ (vol%)
C1	12,58
C2	10,71
C3	3,92
C4	1,81
C5	13,86
C6	7,54
C7	12,96
C8	7,09
C9	1,24

**Table 5c:** Calculated open porosities of the Dh2-samples.

Sample #	$\phi$ (vol%)
D1	1,83
D2	1,05
D3	4,71

As can be seen in table 5a, b and c most of the rocks are characterised by an open porosity lower than 10 vol%. From all field samples, listed in table 5a, only S6, the iron-poor conglomerate, and S8, the chamosite-rich sandstone, have a porosity exceeding 10 vol%. S6 is comparable to C7 (from table 5b) as conglomerate but lacks an iron-rich matrix. C7 also exceeds the 10 vol%. It is however not the only sample from Dh4 with a relative high porosity. C1, C2 and C5 also show porosities higher than 10 vol%. In spite of their sand-content C3 and C4 show porosities almost as low as the porosity of the clay-rich sample C9 which is already part of the cap rock sequence above the Wilhelmøya Subgroup. Apparently C6, which has a similar facies as C3 and C4, still has an open porosity of 7.54 vol%. C8, the chamosite-rich sandstone from Dh4 has a significantly lower porosity as the analogue S8 in the field. Also D1 from Dh2 which is also chamosite-rich has a very low porosity. One can assume that the samples taken in the field have undergone more physical weathering, thus showing higher porosities than their equivalents in the cores. Specifically for these chamosite-rich sandstones one can assume values between those of D1 and C8 to be more correct, dependent on the amount of the rock affected by the formation of chamosite. The value for open porosity of D3 must be approached with attention. Since D3 is very heterogeneous it is likely that the porosity in the upper parts of the sample is higher than the one in the lower parts where the rock consists of less coarse material.

In general the average open porosity of the samples taken in the field (S & T) is 8.27 vol% with a standard deviation of 3.58 vol%. The average porosity of the selected samples from Dh4 is 7.97 vol% with a standard deviation of 4.86 vol% and for the samples from Dh2 this is 2.53vol% with a standard deviation of 1.93 vol%.

### **3.2.2 Permeability**

Permeability measurements were carried on four samples taken from Dh4. Prior to the measurements, PanTerra Geoconsultants B.V. also calculated the ambient He porosity. This is another way of calculating the open porosity and can lead to small differences, compared to the open porosity measurements as described above. Therefore, the results from the open porosity measurements are listed side by side from those calculated by PanTerra Geoconsultants B.V. in table 6. Then the gas permeability was measured together with the empirical Klinkenberg permeability. As a last factor the grain density was calculated. These four factors are listed below in table 6.

**Table 6:** An overview of the results by PanTerra Geoconsultants B.V. with regards to the porosity and permeability of samples C1, C3, C7 and C8.

Sample	Core depth (m)	He Porosity (vol%) (PanTerra)	Open Porosity (vol%)	Gas Permeability (mD)	Emp. Klink. Permeability (mD)	Grain Density (g/ml)
C1	695.25	12,6	12,58	0,23	0,14	2,69
C3	691.04	7,1	3,92	0,05	0,03	2,68
C7	677.16	15,3	12,96	1,11	0,77	2,73
C8	674.52	10,9	7,09	0,18	0,11	3,17

Concerning sample C1, the permeability as measured by PanTerra Geoconsultants B.V. corresponds accurately with the results from the laboratory results of Sintef Petroleum (Braathen et al., 2012). There the permeability of the fine bioturbated sandstones of the same section was determined to be 0.247 mD and the permeability with Klinkenberg effect was 0.144 mD. Also for sample C7, from which the facies is represented by four different measurements from the Sintef laboratory ranging from depths of 678.32 m to 675.49 m, there is a fairly good agreement with the average permeability previously measured. Sintef Petroleum determined a gas permeability of  $1.158 \pm 0.429$  mD as an average for four conglomerate samples in the above mentioned section and with the Klinkenberg effect incorporated the permeability for this section was  $0.892 \pm 0.474$  mD. The permeabilities determined for C7 are closely related to these values and fit within the boundaries of the standard deviation. The measurement of C8 can be linked to a medium to coarse sandstone higher up in the section with a permeability determined to be 0.140 mD and a Klinkenberg permeability of 0.111 mD. These values are conform those of the permeability measured by PanTerra. As for sample C3, no previous measurements were made to which these, displayed in table 6, can be linked. However since the close correspondence found between the measurements made by PanTerra and those made by Sintef for the other samples one can agree these low values of 0.05 mD and 0.03 mD of permeability without and with Klinkenberg effect respectively are correct.

### **3.2.3 Thin section analysis**

Thin sections were made from nine field samples in order to give a general idea of the minerals building the rocks. However, the thin section made from S6 failed to visualise the matrix of the conglomerate. The results from the remaining thin sections are illustrated in figure 13. These 8 samples are: S3 (A), S7 (Bi & Bii), S8 (C), T1 (D), T2 (E), T3 (F), T4 (G) and T5 (H).

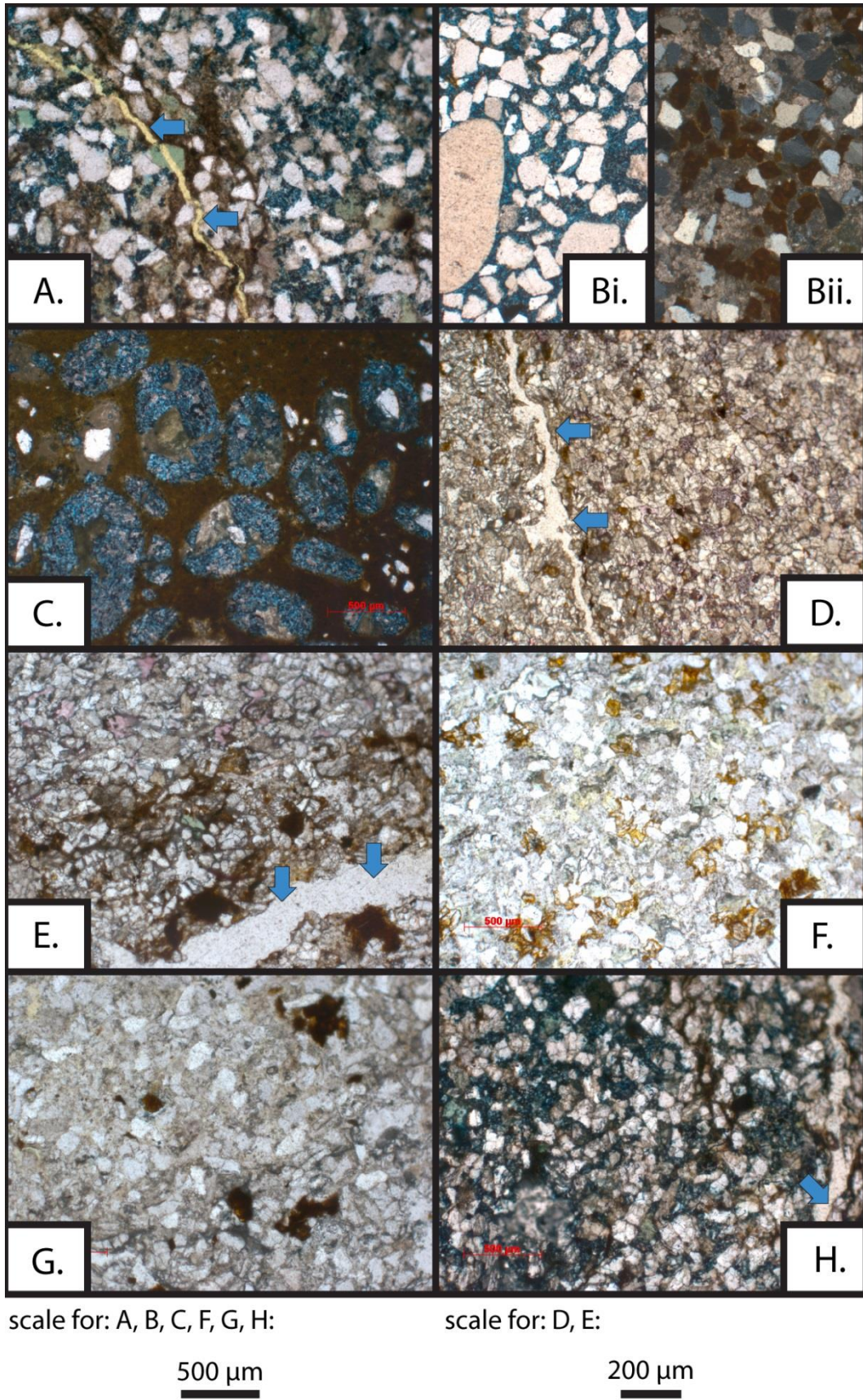


**Figure 13:** Thin sections from samples S3 (A), S7 (Bi & Bii), S8 (C), T1 (D), T2 (E), T3 (F), T4 (G) and T5 (H). in figures a, d, e and h, fractures are indicated with blue arrows. Blue colouring indicates Fe-rich calcite and red to pinkish colouring indicates calcite.

Sample S3 (figure 13a) is characterized by rounded quartz grains which are found in a matrix of iron-rich calcite cement, coloured blue. Within this main facies, some layers are found in which the calcite cement is absent. In these layers, it is replaced by a clay matrix. These are typically the places in the rock where fractures can be found. As accessory minerals, glauconite and siderite can be distinguished. Also some smaller opaque minerals which seem to have a rather cubic shape can be recognized. These are possibly pyrite. Figures 13bi and 13bii both represent the conglomerate sample S7. Figure 13bi is made from an area of the thin section, coloured by potassium ferricyanide. This reveals an iron-rich calcite cement in which sub-rounded quartz grains can be found. Mørk (2013) identifies a siderite-phosphate cement in comparable conglomerate samples. However, siderite or phosphate would not be stained using potassium ferricyanide. This conglomerate is poorly sorted and grain supported. Chert pebbles and quartz pebbles can be recognized in it. As accessory content, feldspars are found, as well as glauconite and organic debris. Siderite can be found as individual minerals, which tend to form linear structures in the rock. In figure 13bii, siderite can be distinguished as a rhombic mineral with brown appearance in a cross-polarised thin section.

Sample S8 (figure 13c) is characterized by a siderite matrix in which ooid grains are found as most distinctive features. In these ooids, the central part is often composed of chamosite, the  $\text{Fe}^{2+}$  end member of the chlorite group. The outer parts however are composed of iron-rich calcite, which reacted with the potassium ferricyanide and coloured blue. This probably replaced the original chamosite of the ooids. The ooids probably formed in distal parts of a delta where clastic sedimentation is low. Spread over the thin section, one can also identify small quartz grains in the siderite matrix as well as larger phosphate grains. Sample T1, illustrated in figure 13d consists mainly of quartz found in an iron-poor calcite cement, with the presence of dispersed iron oxide hydroxides. Between some quartz grains, quartz cement is present. The fracture which is visible in figure 13d is possibly due to the making of the thin section.

In figure 13e, sample T2 is shown. It is characterized by a layered distribution of clay minerals along which fractures originate. Sub-rounded quartz grains are found in an iron-poor calcite cement in which also some accessory mica and glauconite are found. Also siderite minerals can be distinguished. Figure 13f shows sample T3 in which sub-angular quartz is the most abundant mineral. Clay fills the available space between these grains and some glauconite can be found as accessory mineral. Sample T4 is represented in figure 13g. This sandstone sample shows a patchy distribution of clay and some dispersed iron-rich calcite. Rhombic brown siderite and accessory mica can also be identified. In T5 (figure 13h) fractures are found along an iron oxide hydroxide matrix. In this grain supported sandstone quartz is the most abundant mineral. Also siderite and some opaque minerals can be identified. Some quartz boundaries are characterized by sutured contacts.

### **3.3 CT-data**

In this chapter, the samples and scans will be discussed according to their location and resolution. First the field samples (S- and T-samples) will be discussed going from low resolution to high resolution. Doing so different features will be highlighted at two different resolutions: 41  $\mu\text{m}$  and 4  $\mu\text{m}$ . Then the samples taken from Dh4 and Dh2 will be discussed. The same principle in which different features are described at different resolutions will be used. Because these samples were wider to start with, the first resolution at which they were scanned was 56  $\mu\text{m}$ . Then subsamples were taken with a diameter of 6 mm and 2 mm which were respectively scanned with a resolution of 4  $\mu\text{m}$  and 2.7  $\mu\text{m}$ .

#### **3.3.1 Field Samples (S- and T-samples)**

##### **3.3.1.1 Scans at resolution 41 $\mu\text{m}$**

From the field samples, seven were chosen to be scanned at a relative low resolution. These are samples T1 to T5, S3, S6, S7 and S8. All of the samples were scanned with a SOD of 132.43 mm and obtained a magnification factor of 6.12. Additionally, to limit the beam hardening in advance, two hardware filters were placed between the X-ray source and the sample. It concerns a 1 mm thick aluminium plate and a 0.3 mm thick copper plate. The resulting resolution was 41  $\mu\text{m}$ . The scans were subsequently analysed for their fractures, fossil-content, homogeneity or heterogeneity and porosity. Especially the fractures appear to be striking features in the field samples.

##### *3.3.1.1.1 Facies*

A first distinction that can be made from looking at the scans of the samples is the distinction between samples which are homogeneous and those that are heterogeneous concerning the distribution of minerals. A sample consisting of different minerals is homogeneous when the minerals exist side by side and their relation to one another does not change throughout the sample. However when there is a clear distinction between different areas concerning the mineralogical composition, the samples has a heterogeneous distribution of minerals. Five of the field samples have a homogeneous distribution of the minerals. These are T1, T3, T4, T5 and S3 from which the scans are displayed in figure 14.

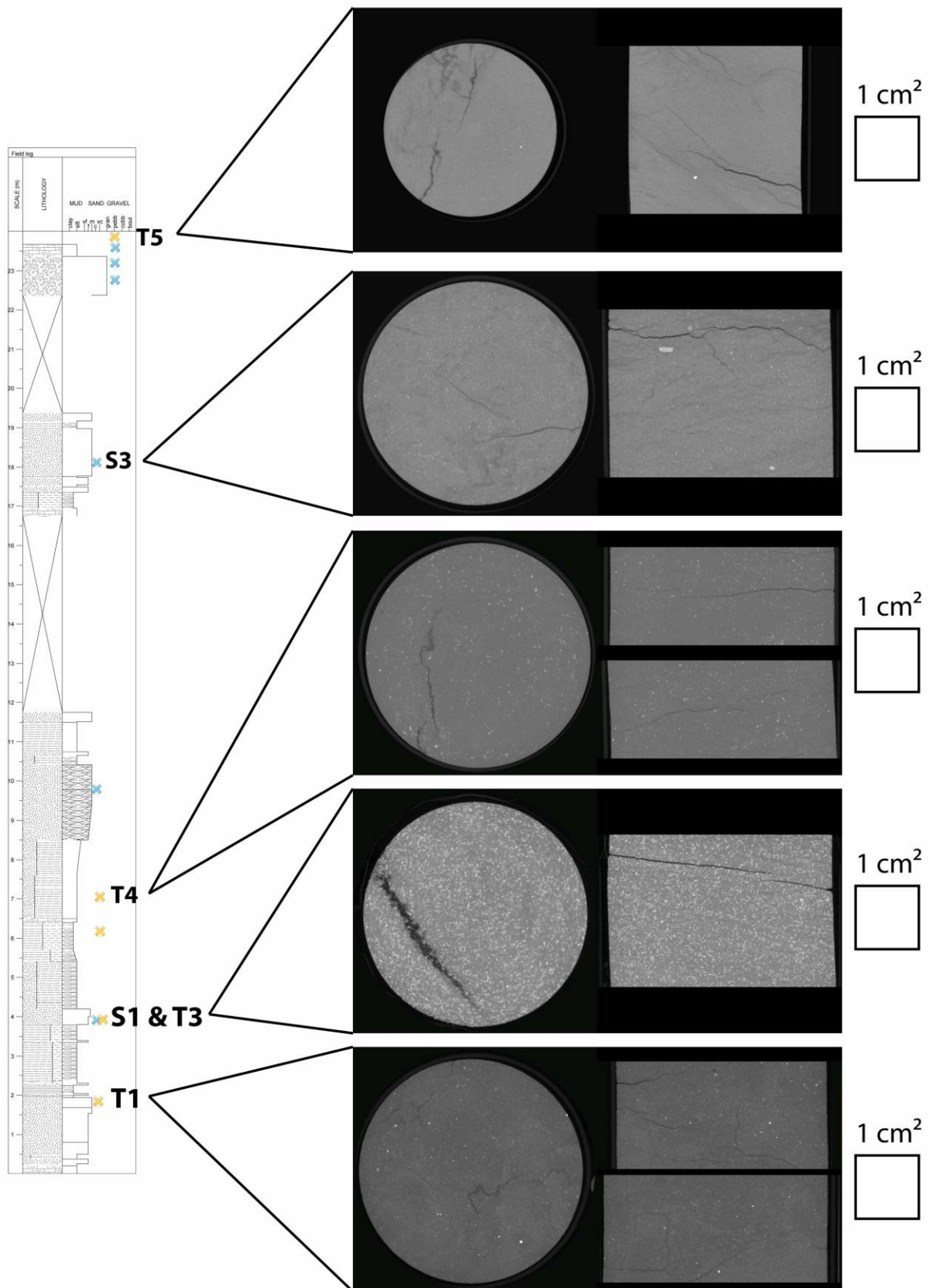


**Figure 14:** Visualisation of samples T1, T3, T4, S3 and T5. They are linked to the field litholog in order to locate them. In every sample fractures can be identified. Another feature in common is the homogeneous distribution of minerals found in all 5 samples. As scale a corresponding square centimetre is given.



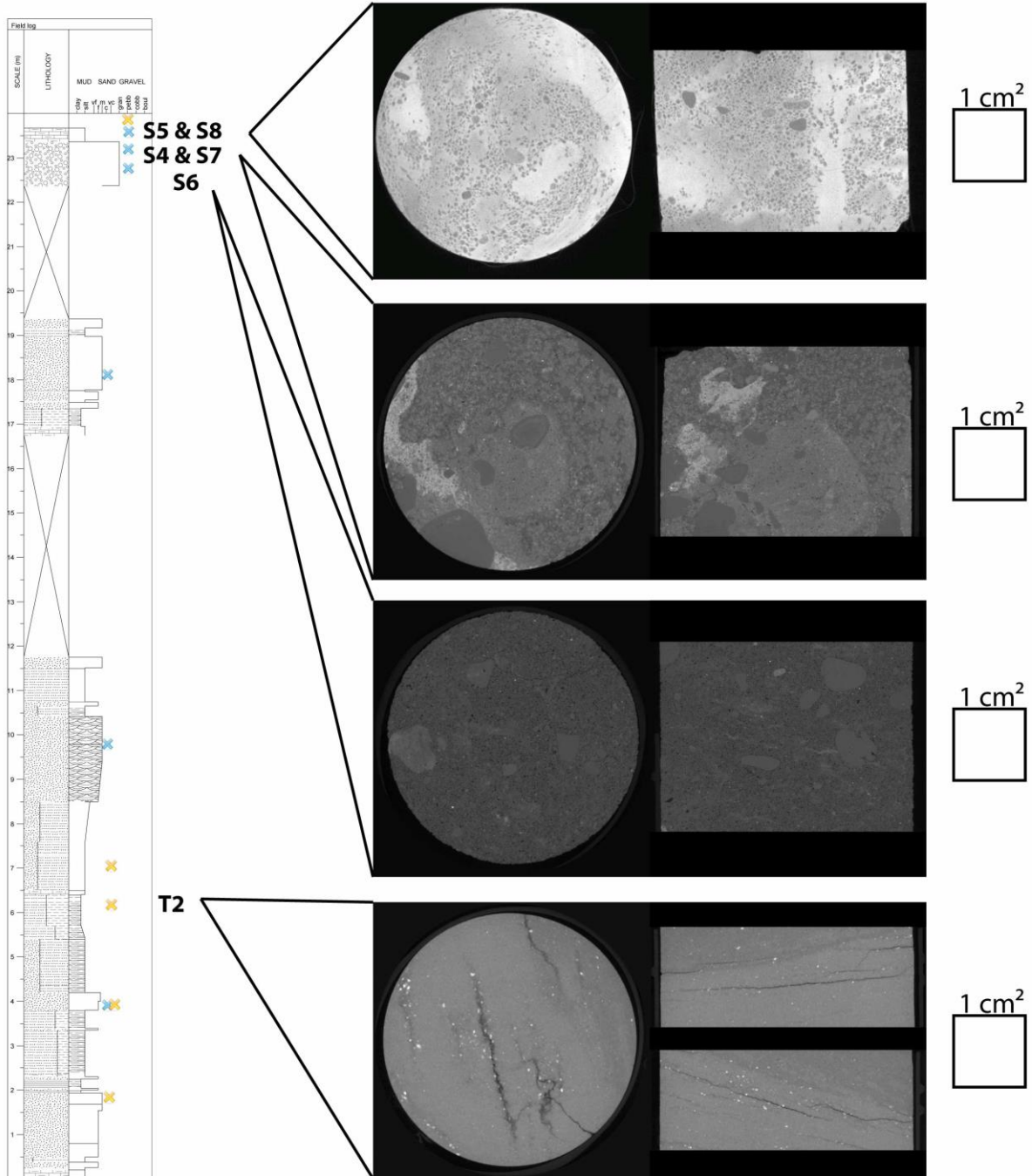


**Figure 15:** Visualisation of samples T2, S6, S7 and S8, linked to their location in the field litholog. These samples have a heterogeneous distribution of minerals and are all characterized by fractures, although these are very subtle in samples S6, S7 and S8. As a scale, a corresponding square centimetre is given.

The heterogeneous samples T2, S6, S7 and S8, illustrated in figure 15, are characterized by different reasons of heterogeneity. T2 for example is a sample in which a horizontal bedding structure causes the heterogeneity. Layers of quartz-rich sandstones alternate with more clay-rich layers in which corroded iron-rich minerals can be found. In the scans, this layering can be noticed due to the presence of these minerals since they are very bright thanks to their iron-content. In S6, the conglomerate sample with a matrix generally poor in iron, there are several patches within the matrix where the porosity is decreased due to infill of iron-rich minerals. This is the reason why this

sample is heterogeneous and as with sample T2, it can be seen on the scan thanks to the bright character of these minerals. Sample S7 has an overall higher iron-content than S6 but is also heterogeneous due to the occurrence of different types of matrix. A total of three different matrixes are distinguishable. A first matrix consists almost entirely of an iron-rich cement and appears very bright on the scanned images; the second one still has the iron-rich minerals but they do not occur in a cement type distribution so that this matrix has an overall lower greyscale value; the last matrix has a similar appearance as the second one, although now it is mixed with a cement which appears to be iron-poor. These three types of matrix are distinguishable in both the cross-section in the Z-plane and the cross-section in the X-plane of S7 in figure 15. When examined closely one can identify the three matrix types in the hand sample as well. In the last heterogeneous sample, S8, the heterogeneity is accomplished due to the irregular spreading of ooids in the sample. There are regions rich in ooids and regions which are poor in ooids. As mentioned in the subdivision “fractures”, the fractures in S8 are generally located in the ooid-poor areas of S8. Overall these areas are brighter in the scanned images, not because the matrix here contains more iron, but because the signal of the matrix is diminished by the ooids which contain less iron.

#### *3.3.1.1.2 Fractures*

Fractures are important and prominent features in the field samples. All seven of the samples which were scanned show the presence of fractures in one way or another. However it is unclear to what fraction these fractures are primary to the rocks. Most of the fractures seem to be related to the frost weathering the samples have undergone. This is probably the case for all fractures in samples T1 to T5 as well as for those in S3. This interpretation can be supported by the fact that the fractures are concentrated along the clay-rich sections of the rocks. The clays have water within their mineralogical structure and thus are prone to expansion and contraction in freezing and thawing conditions as present in Spitsbergen. In this way the fractures come about. When looking in detail one can see the fractures originate in areas of low attenuation which are rich in clays and follow a path interlinking these clay-rich regions of the rock. Especially for sample T2 it is obvious that the presence of fractures is connected to a change of mineralogy of the rock due to the fact that they follow changes in grey scale values in the scanned images. With the MSHFF script of Voorn et al. (2013) the fractures from sample T1 to T5 and those in S3 were segmented. In figure 16 an overview is given of the observed fracture orientations in these samples. This is done via stereographical projections of objects which were made from the segmented fractures using Morpho+. The stereoplots which will be used differ from normal geological stereoplots. Since the scans cannot be oriented, there is no specified north-, east-, south- or west-direction in the stereographs. The dip of the fractures is not linearly distributed on the stereoplot, but the dip angles are always indicated on the figures. For further information about the construction of these stereographical projections, reference is made to Brabant et al. (2011).

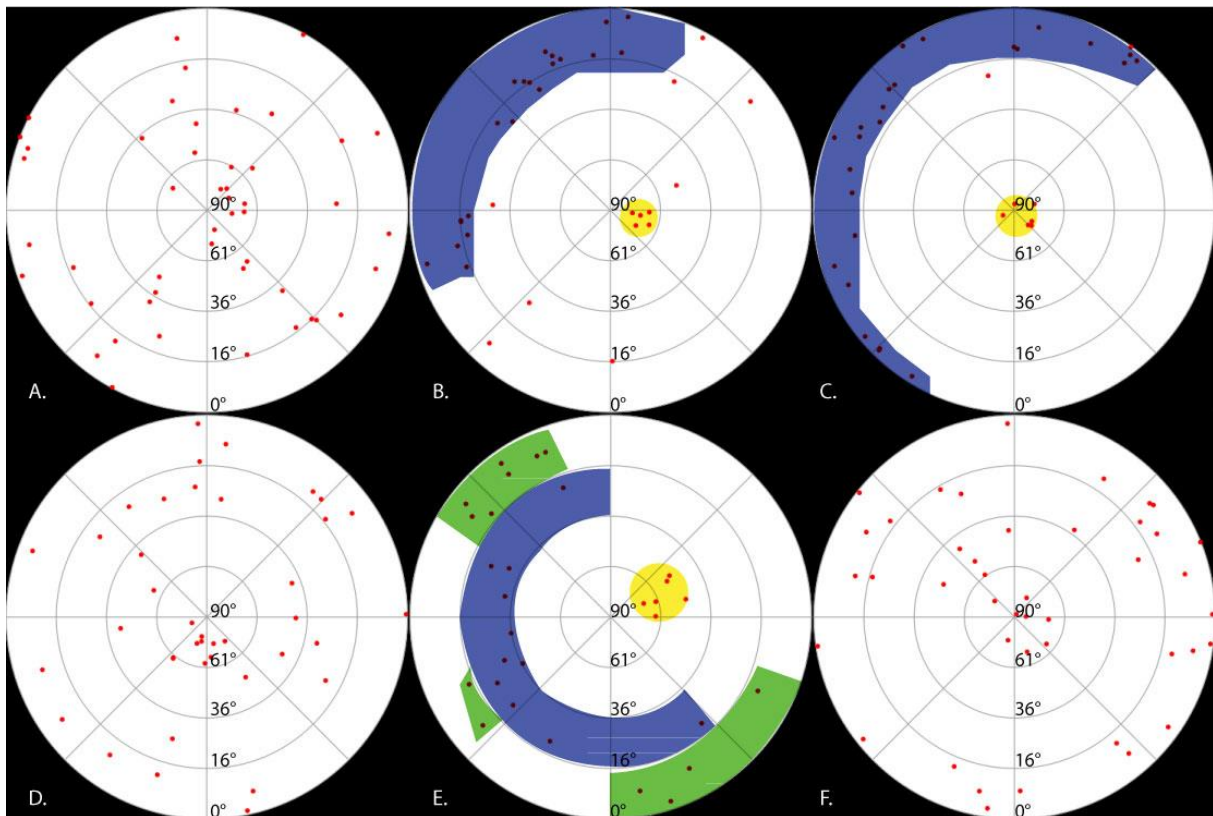


**Figure 16:** Stereographic projections of the fracture objects from samples T1 (a), T2 (b), T3 (c), T4 (d), T5 (e) and S3 (f). The blue subset groups the (semi-) horizontal fractures in figures 16b, 16c and 16e. In the same figures, the yellow subset represents (semi-) vertical fractures. In figure 16e, the green subset represents fractures resulting from sampling. In this stereograph the dip of objects is not linearly distributed. Therefore the dip angles are included in the figures.

For T2 (figure 16b) and T3 (figure 16c) the distribution of the observed fracture orientations can clearly be divided in 2 separate regions. The best example to illustrate this separation is sample T3. The fractures, are either horizontally distributed, with a dip of maximum 16°, or vertically. Most of the fractures of samples T2 and T3 have a (sub-) horizontal orientation. These are the objects which are found in close proximity with the outer border of the stereograph in figure 16b and 16c and are encircled in blue. Nonetheless there is a second group of fractures which have a quasi vertical orientation. They plot close to the centre of the stereograph and are encircled in yellow. A similar differentiation can be made in the orientations of fractures in sample T5, although all fractures seem to be tilted so that the vertical fractures do not plot in the centre of the stereograph and the semi-horizontal fractures are removed further from the border. A similar division is made in figure 16e as with the stereographs of T2 and T3. However, a third subset is added in green. These represent fractures due to sampling. From the field sample, a cylindrical core was drilled. This drilling did not take place perpendicular to the horizontal bedding, but with a slight angle. This is the reason why the horizontal and vertical fractures seem to be tilted in the stereographic projection. In sample T2 the vertical fractures form a connection between different horizontal fractures (figure 17a). Measurements in Fiji reveal they can connect fractures with a height difference of up to 2.7 mm. In sample T3 the vertically oriented fractures do not connect two separate horizontal fractures, but form steps along which one horizontal fracture shifts vertically inside the sample (figure 17b). These steps are significant, but don't exceed distances as large as the vertical fractures in T2. An average step has a vertical distance of 0.7 mm.

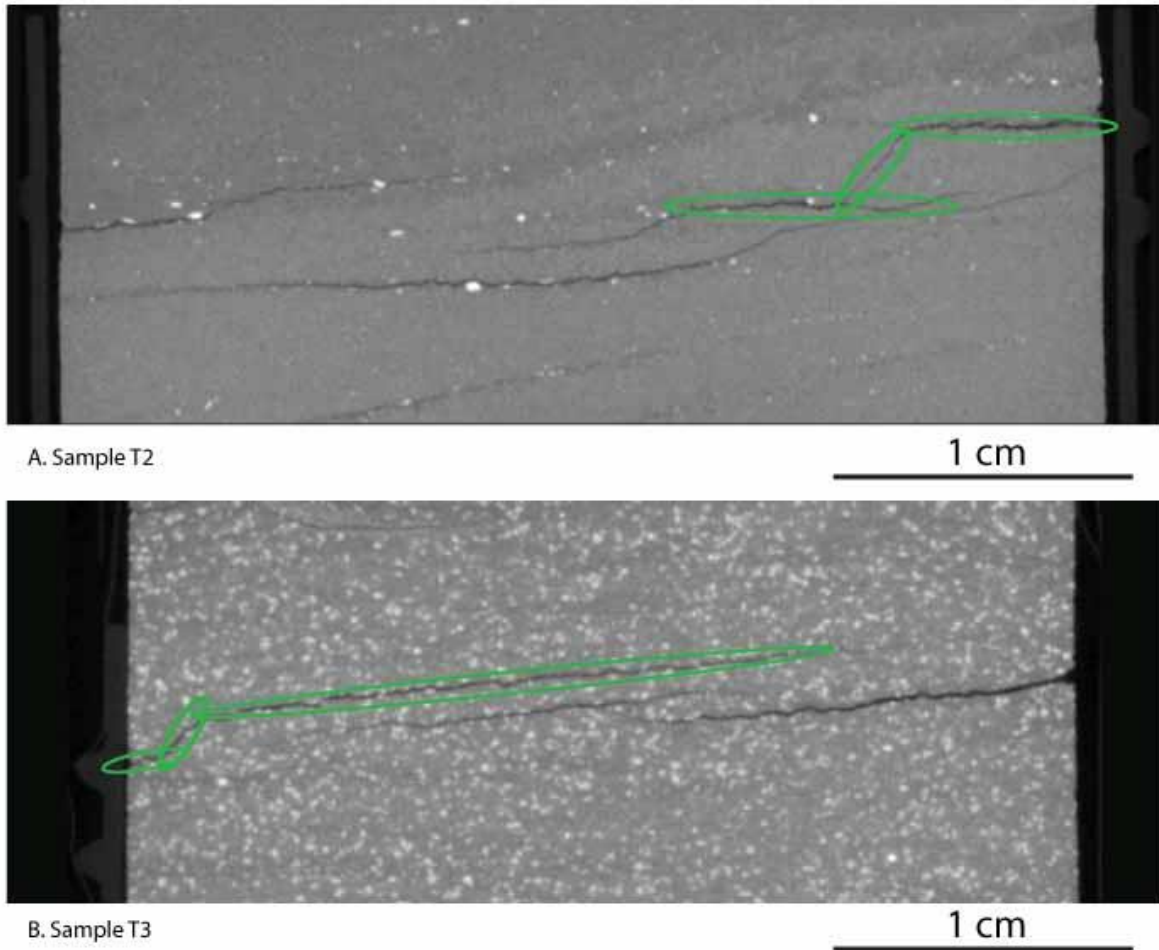


**Figure 17:** Fracture analysis in samples T2 (a) and T3 (b). Vertical fractures form connections between horizontal fractures, or act as a step along which the horizontal fracture moves in order to propagate in the vertical direction.

Sample T5 has a distribution of fractures which are closely related to the areas with a lower greyscale value in the images. They are the clay-rich areas in the sample along which fractures originate. Consequently, the orientation of these enrichments influences those of the fractures. This results in the stereograph as illustrated in figure 16e. From T2, T3 and T5 this is the sample in which the fractures can be described as the least horizontal. Almost 50 % of the orientated fractures have a dip between  $16^\circ$  and  $36^\circ$  and can hardly be described as horizontal. The most vertical fractures have an average dip of  $60^\circ$ . Also in S3, a large part of the fractures show a horizontal orientation while some fractures can be defined as vertical (figure 16f). Again, they can be linked to clay material in the sample (figure 14).

The fractures can not only be described by their orientation, but also by their maximum opening. In figure 18 an overview is given concerning the maximum opening of fractures in samples T1 to T5 and S3. It is expressed in amount of voxels, with a resolution of  $41 \mu\text{m}$ . The fractures in the samples are represented by separated objects, so one fracture can be represented by more than one object. This gives a better characterization of the fractures themselves. From figure 18 one can observe that the fractures are dominated by a maximum opening of 3 voxels ( $123 \mu\text{m}$ ), especially in sample T1 and T4 where the fractures are represented by a higher amount of objects than in the other samples. The largest fracture openings are found in samples T5 and S3 where a part of the fractures are

characterized by a maximum opening of 13 voxels (533  $\mu\text{m}$ ). It is striking that none of the objects have a maximum opening of an even amount of voxels.

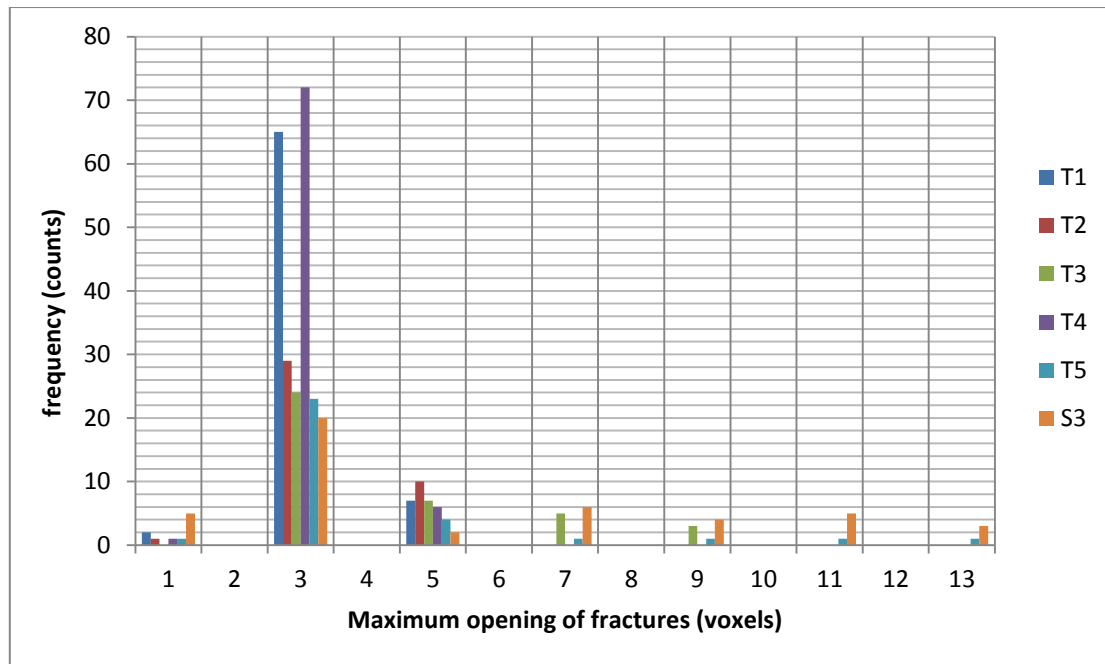


**Figure 18:** Graph showing the distribution of the maximum opening of fractures from samples T1, T2, T3, T4, T5 and S3. One voxel equals 41  $\mu\text{m}$ .

Not all fractures found in the field samples can be explained by physical weathering. In the two conglomerate samples S6 and S7 and in the chamosite-rich sandstone sample S8 there are fractures which are not related to clays in the rocks. S6, the conglomerate with an iron-poor matrix, shows two kinds of fractures. The first kind can also be seen in S7 and is characterized by the fact that the fractures are found inside the pebbles of the conglomerate. They can be found in phosphatic as well as chert pebbles and do not affect the matrix. The second kind of fractures, which is found in S6 but not in S7, are fractures in the matrix of the rock. These don't go through individual clasts but go around them. Unlike the fractures in the T-samples and S3, they are not related to clay in the rock, but are probably enhanced in size due to frost weathering. However, this type of fractures is only present once in the entire sample S6. Therefore, no stereograph was made. The fractures in sample S8 are restricted to the regions in which the rock has a low abundance of ooids as can be seen in figure 15. The fracture in S6 going through the matrix is characterized by openings of 2 to 3 voxels wide (82 – 123  $\mu\text{m}$ ) and is thus of opening width comparable to the fractures in the T-samples and S3. Those however which are found in the clasts of the conglomerates, both of S6 and S7 are wider. The maximum openings found in S7 are 5 voxels wide (205  $\mu\text{m}$ ). In S8 the fractures with a distinct vertical and horizontal orientation follow the same fracture opening distribution in which most of them are characterized by a maximum opening of 3 voxels wide (123  $\mu\text{m}$ ).

### 3.3.1.1.3 Fossil-content

As mentioned in "table 2" in chapter "3.1 Field work", sample T1 is formed by galleries of *Thalassinoides* tunnels, however this is not immediately visible on scans. The ichnofossil *Thalassinoides* in the hand sample however is easily recognisable. It forms mazes of T-branched shafts which are unlined and unornamented. In cross-section, it can be seen that the sides of the

tunnels are plastered by clays while sand fills in the tunnels. This can be the explanation for the fact that the structure is not visible on scans. Since the resolution of the scan is 41  $\mu\text{m}$  everything smaller than this will not be visible as a distinct feature. So if the rim of clay, which forms the outer sides of the tunnels, is smaller than this resolution, it cannot be revealed on the scan.

Another sample in which a fossil can be recognized is S3 (figure 19). The feature of interest is dens, elongated and shows perforations. Although it is difficult to name from these general characteristics, it resembles possibly certain species of algae.

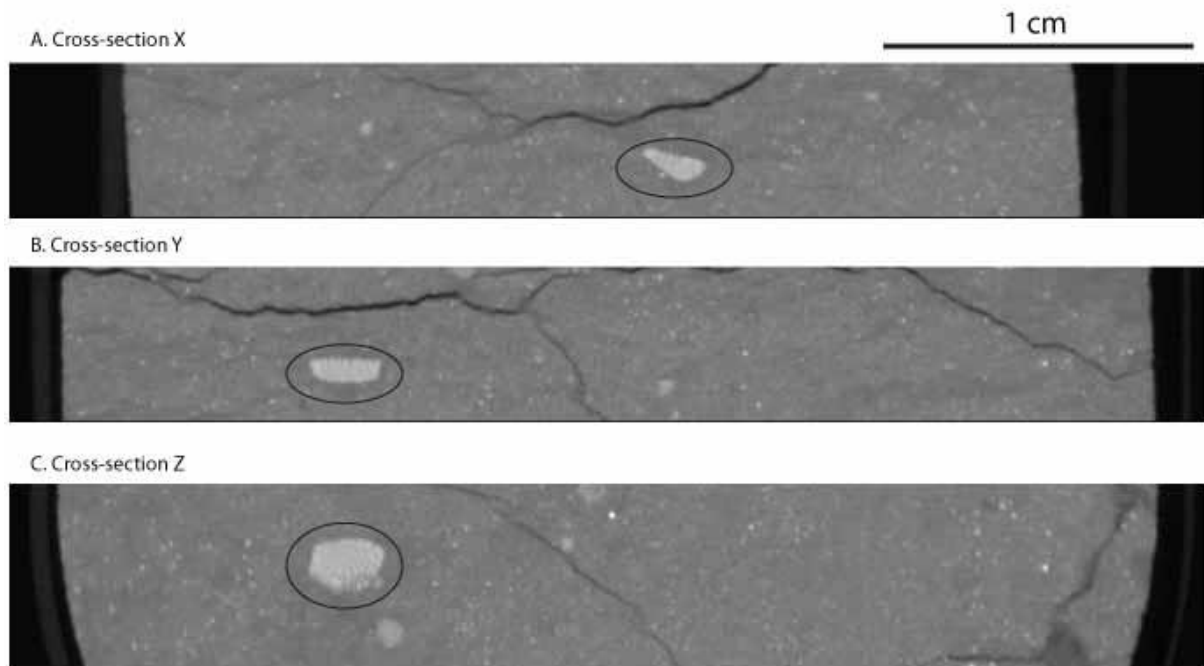


**Figure 19:** Three perpendicular cross-sections through sample S3 in which a dens and elongated object with perforations is visible. For the ease of recognition it is encircled in all three cross-sections. This assumed to be algae fossil is 2.087 mm in length.

#### 3.3.1.1.4 Porosity

Without regarding the fractures as porosity, the porosity was visual in only two of the 9 field samples at this resolution. This is the case in samples S6 and S7 which respectively had an open porosity of 16.76 vol% and 4.47 vol% according to the laboratory tests. When extracting the porosity in Morpho+ however, S6 has a total porosity of 10.85 vol% and S7 one of 0.94 vol%. This means not all of the porosity is visible at this resolution and at least 5.91 vol% and 3.53 vol% of the porosity of S6 and S7 respectively is represented by pores smaller than 41  $\mu\text{m}$  in diameter, since the calculated open porosities for these samples were higher in the laboratory tests. The porosity as seen on scans with this resolution is not suited for extraction of a pore network in E-Core because the sample size would be too big in comparison to the size of the pores and the connectivity between the different pores is poor. Also, since the scans fail to visualize all of the pores in the sample, the results would be false.

#### 3.3.1.2 Scans at resolution 4 $\mu\text{m}$

Five samples were drilled in order to obtain subsamples with a diameter of 5.0 mm. These are S2, S7, T1, T2 and T3. They were subsequently scanned with a SOD of 27.41 mm which gave a magnification

of 31.47 times and an image resolution of 3.99  $\mu\text{m}$ . As a hardware filter a 1 mm thick aluminium plate was used. The resulted scans are illustrated in figure 20.

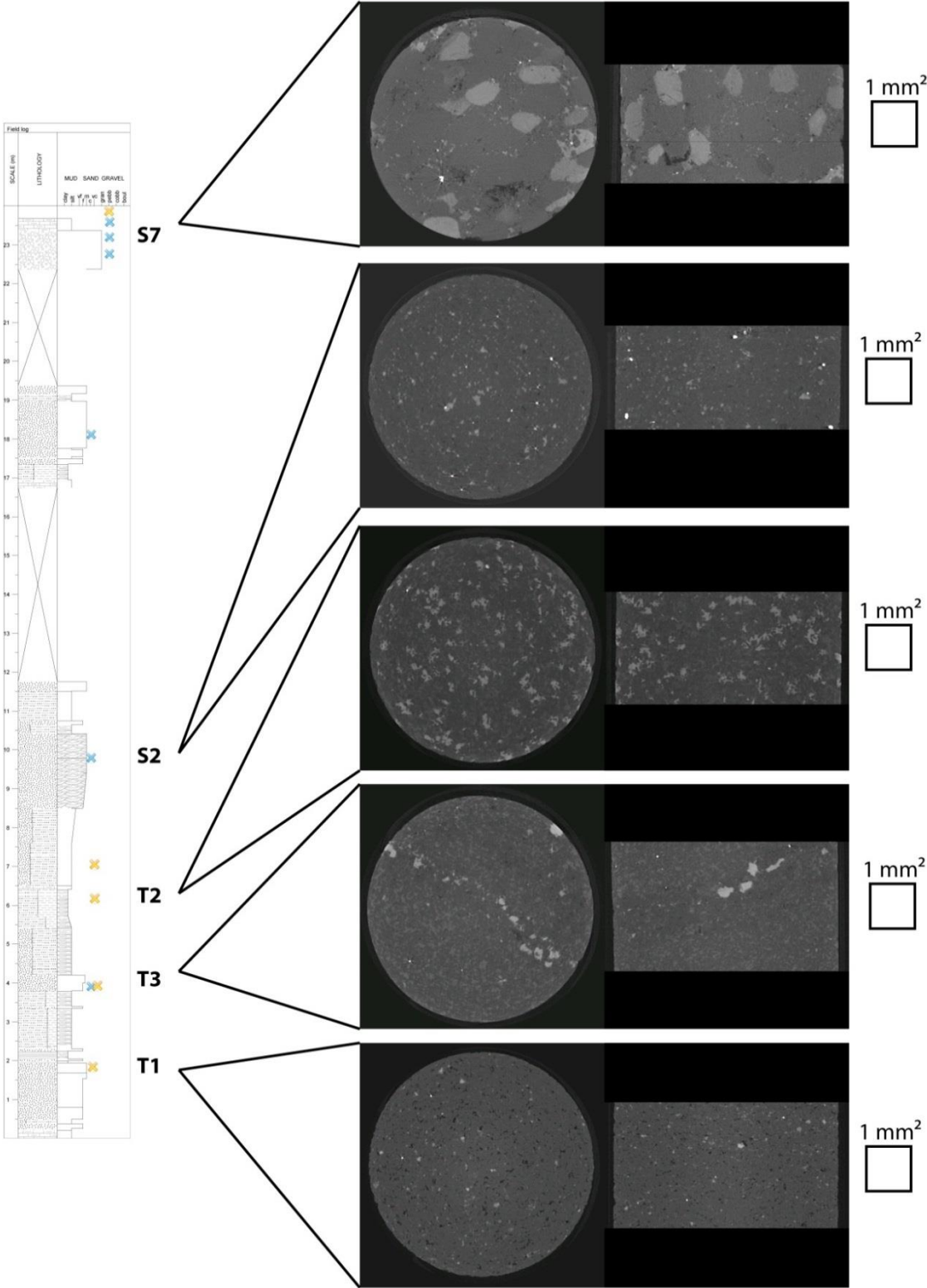


**Figure 20:** A cross-sectional representation of the samples scanned at a resolution of 3.99  $\mu\text{m}$ . The cross-sections, each taken in the Z- and X-plane are linked to the location of the samples in the field log. All samples have a homogeneous distribution of minerals, except for T3 in which a layer of clay-minerals breaks up the homogeneity. In T1 and S7 porosity is visible.

Two of the samples (T1 and T3) have a homogeneous distribution of the minerals at a resolution of 41  $\mu\text{m}$ . The exact location of the subsamples could thus be chosen in a random way. In both samples a subsample was taken at a location that was not affected by fractures in the low-resolution scans. Samples T2 and S7 were characterized with a heterogeneous distribution of minerals. Therefore special attention was given to the exact spot of subsampling. In S7 a subsample was taken at a location characterized by the absence of an iron-rich matrix, because this iron-rich infill tends to destroy the porosity in the sample. The subsample in T2 was taken from the sand-dominated parts of the sample. Due to this targeted way of subsampling, all samples, except for T3, have a homogeneous appearance at this resolution. In T3, there is one layer of clays present, which breaks up the otherwise homogeneous sample.

Since heterogeneous sections and fractures are avoided via targeted subsampling, and no fossils were recognized in the samples, the porosity distribution is the most important feature in these scans. The samples were chosen according to the open porosity results of the laboratory tests. Samples T1 and T3 are among the samples with the highest open porosity at 9.68 vol% and 9.03 vol% respectively. S2 is, with a calculated open porosity of 7.85 vol%, the sandstone sample with the third highest porosity and can thus be especially interesting since it was not scanned at the lower resolution of 41  $\mu\text{m}$ . Sample T2, with an open porosity calculated at only 5.13 vol%, is expected to have a higher porosity in clay-poor regions of the rock. S7, the conglomerate sample with an iron-rich matrix has a much lower porosity than the conglomerate sample poor in iron, but is more representative for the Brentskardhaugen Bed than S6. Therefore it is interesting to characterize the pores in this sample. In two from the five samples (T1 and S7) the porosity was clearly visible at this resolution. However, in T1 the observed porosity is much lower than the calculated open porosity. In total 2.56 % of the scanned volume represents pore space. Since the porosity was not visible at the resolution of 41  $\mu\text{m}$  either, this infers that at least 7.12 vol% from the calculated 9.68 vol% is represented by pores smaller than 4  $\mu\text{m}$ . This is however only correct when the fractures in the sample can be considered as a negligible factor in the porosity, which is probably a false assumption for sample T1. The selected subsample of S7 is characterized by a thresholded porosity of 3.68 vol%. Although this is open and closed porosity combined, it is 0.79 vol% less than the calculated open porosity from laboratory tests. Since S7 was not characterized by fractures through the matrix of the rock at a resolution of 41  $\mu\text{m}$  and no fractures are observed at the resolution of 4  $\mu\text{m}$ , it is safe to infer that the remaining porosity is represented by pores smaller than 4  $\mu\text{m}$ . In two other samples, the scans show hints of porosity: in T3 0.9 % of the scanned volume can be thresholded as porosity and in S2 0.68 %. From previous scans, one can conclude that in T3, fractures are probably important contributors to the porosity, although pores smaller than 4  $\mu\text{m}$  cannot be excluded. For S2 no previous scans are available so the question remains whether or not fractures are important for the porosity in this sample, or normal pores, smaller than the given resolution are the main contributors. In the last sample, T2 not a single pore could be extracted from the scans. Also in this sample, fractures visible at a resolution of 41  $\mu\text{m}$  seem to be important contributors to the porosity.



### **3.3.2 Dh4 Samples (C-samples)**

#### **3.3.2.1 Scans at resolution 56.61 $\mu\text{m}$**

The samples of Dh4 have a diameter of 4.7 cm. All of them were scanned except for C5. They were scanned with a SOD of 182.57 mm which resulted in a magnification of 4.44 and a resolution of 56.61  $\mu\text{m}$ . This resolution is already high enough to notice and characterize certain features in the rocks, but it is too low to extract a pore network from it in order to conduct flow simulations with it. One of the features which can be distinguished within the samples is the occurrence of fractures. However, as with the field samples, an overview is given of the fossil content, the facies and the porosity within the rocks as well.

##### *3.3.2.1.1 Facies*

All scanned samples have a heterogeneous mineral distribution in one way or another. The scans are illustrated in figure 21, in which samples C1, C3, C4 and C8 are visualised and in figure 22 where an overview is given of samples C2, C6, C7 and C9. This division was made to visualise samples with fractures (figure 21) separately from those without fractures (figure 22).

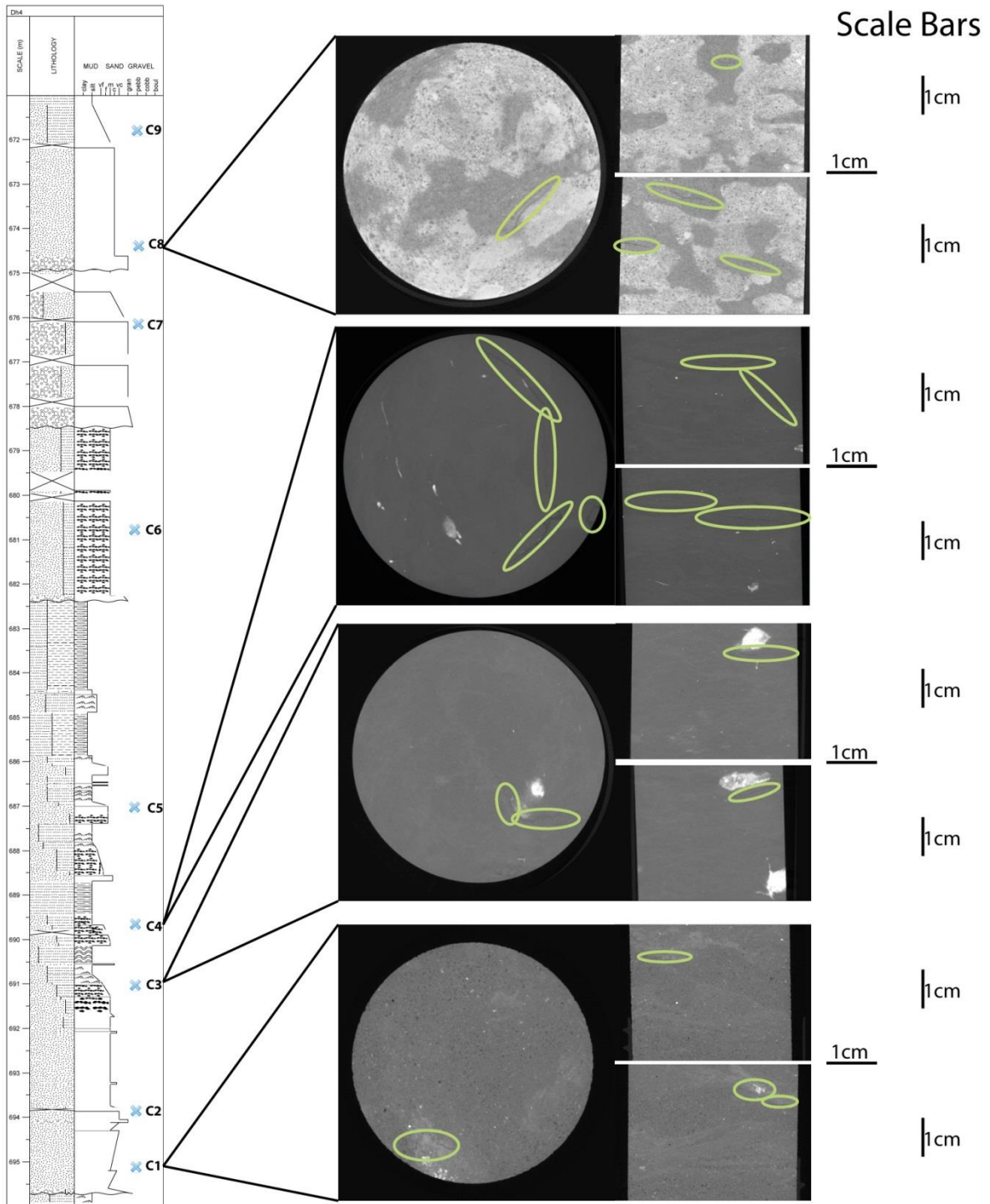


**Figure 21:** An overview of the scanned images in which fractures are visible. They are connected to the litholog in order to locate them. Images of samples C1, C3, C4 and C8 are given in which the fractures are encircled in green. Although it is subtle the fractures can be identified due to their low greyscale value. Apart from the fractures, which are described in the section “fractures” in this chapter; these cross-sections are used in order to describe the general facies of the samples.

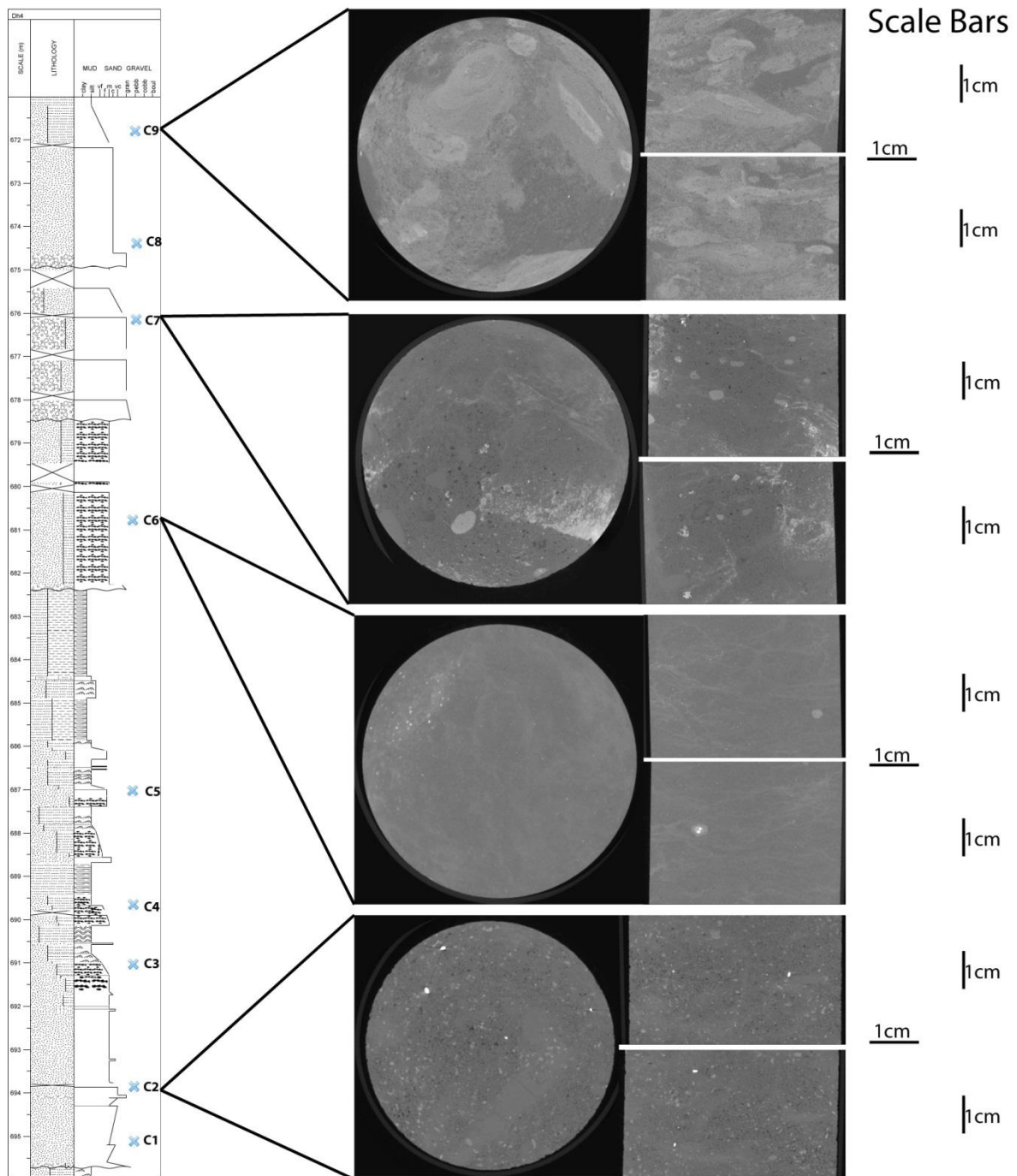


**Figure 22:** An overview of the scanned images of samples C2, C6, C7 and C9. They are connected to the litholog in order to locate them. In all four samples a heterogeneity can be observed in one way or another.

In both C1 and C2 the heterogeneity is visible due to the fact that the images can be subdivided in two distinct parts. On the one hand both samples have areas within them in which porosity can be observed, while on the other hand regions with a clearly decreased porosity signature are present. The difference between both samples is found in the grain size distribution in both samples. In C1 the different quartz grains in the regions with enhanced porosity cannot be distinguished from each other while those in C2 can. In C2 several grain-to-grain contacts can be observed thanks to the slightly larger grain size. In both samples the areas with elevated porosity can be segmented and visualised. This can then be used as a base for deciding where to take subsamples. This process is

illustrated for C2 in figure 23. First, the actual sample is compared to the 3D visualisation. Special attention is given to striking features such as the two vertical mud-rich areas inside the sample. These are both visible in figure 23a and 23b. Now that the sample is orientated, the segmented porosity can be added to the picture. In figure 23c a clipping box is used in order to evaluate the distribution of the pores within the sample. In this way, the areas which are interesting for taking subsamples of can be identified.

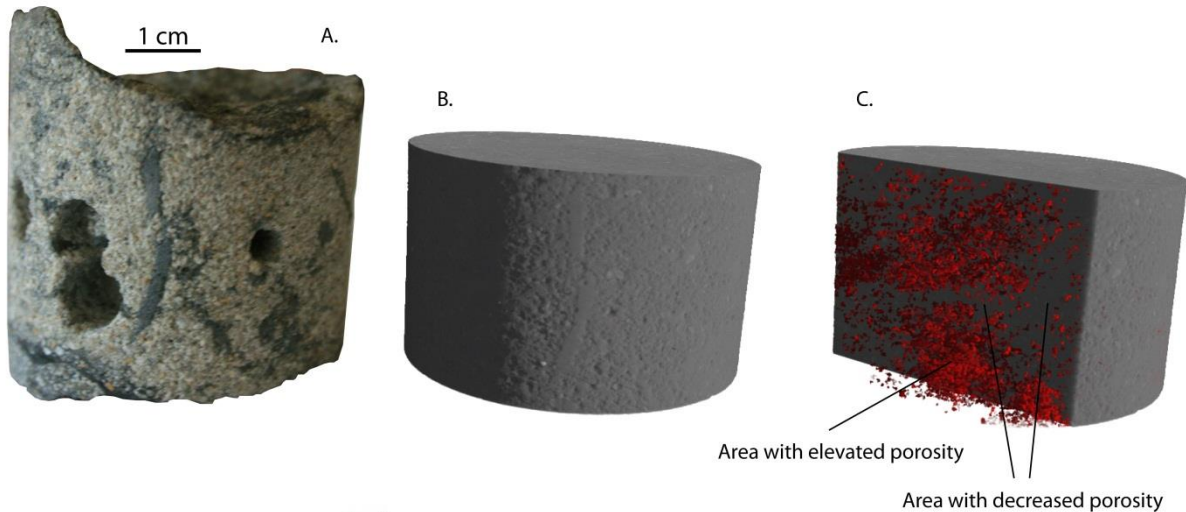


**Figure 23:** Subsampling strategy explained with the example of C2 from which the porosity could be extracted. Figure 23a is a normal photograph of the sample in which two vertical mud features can be distinguished. The same features can be found in the scatter HQ visualised image in figure 23b. Once the sample is orientated, a clipping box is used (figure 23c) in order to extract areas of low and high porosity in the sample.

The main source of heterogeneity in samples C3 and C4 is illustrated and explained in the “fossil” section of this chapter. However, also in the matrix in which a system of burrows is incorporated one can find a heterogeneity. This is due to the fact that a difference can be made between two ground masses. In cross-sections it is very difficult to see this difference. However, when visualised in 3D it is easier to identify the heterogeneous nature of these rocks. In figure 24a the overall heterogeneity of sample C3 is illustrated. One can identify two pyrite filled chambers, fractures and the dual matrix in which these features are incorporated. Figure 24b gives a same impression of sample C4: one of the pyrite filled chambers is visible as well as some tubes part of the burrow system. There are several fractures visible and two different ground masses can be identified. Figure 24c shows that similar structures can be found in sample C6. All three samples are characterized by flaser to lenticular bedding. This explains the different ground masses. There are sandstone fragments and silt- to claystone fragments which are intermixed with each other.

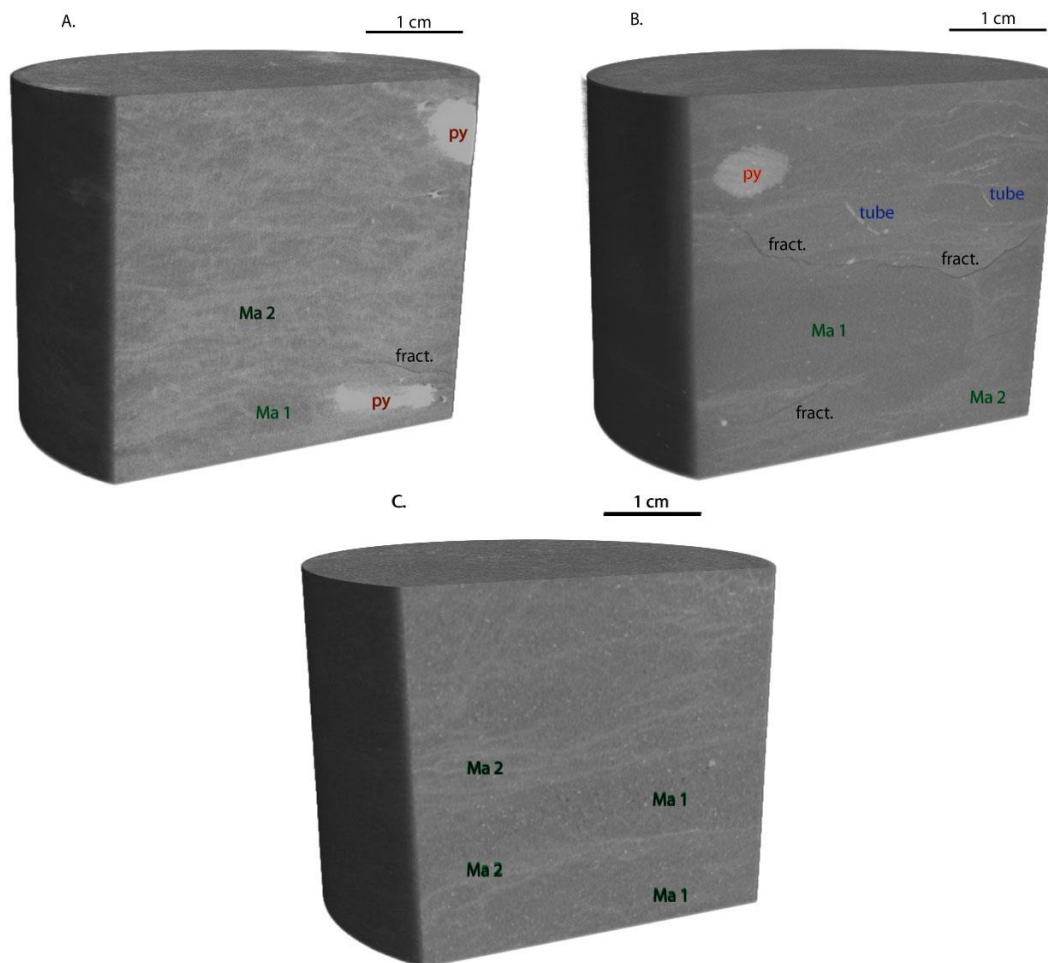


**Figure 24:** Scatter HQ 3D visualisations of samples C3 (a), C4 (b) and C6 (c). In both figures 24a and 24b pyrite chambers are indicated (py) as well as fractures (fract) and the heterogeneity of the ground mass of the sample (Ma 1 and Ma 2). In figure 24b some pyrite tubes can be recognised.

In C7, the conglomerate sample taken from Dh4, clasts with different mineralogies can be identified. It is known from Bäckström & Nagy (1985) that the main pebbles are quartz, chert and phosphates. When plotting apatite and quartz in an attenuation graph such as illustrated in figure 7 (chapter 2.2 Methods: CT), one can see that apatite, which is the main phosphatic mineral group, has an overall higher attenuation than quartz. This makes it possible to distinguish these different clasts in the scanned images. The quartz and chert pebbles have a greyscale value comparable to the overall matrix of the conglomerate and are well rounded, as where the phosphatic pebbles are characterized by an elevated greyscale value and thus appear brighter in the images. They often have a more oval shape than the quartz pebbles which corresponds with the observations of Maher (1989). Concerning the matrix, one can differentiate between two types. A primary matrix consists mainly of quartz grains. In this matrix, a hint of porosity distribution is visible. In the second type, the same matrix is found, but with an elevated clay-content distributed within it. This diminishes the porosity in this matrix type. The difference however is very subtle.

Sample C8 is characterized by the occurrence of ooids and two different matrix-types. The ooids can be found in both types while fractures are only found in the iron-poor matrix. The distribution of the iron-rich and iron-poor matrix can be described as a horizontal layering with frequent vertical

connections between layers of the same type of matrix. This explains the spotted appearance of the sample in scanned images. C9 has a more chaotic distribution. This very dense rock sample in which sand grains are incorporated in a claystone is characterized by three different ground masses which are interwoven in a disorganized manner. Comparison with the hand specimen shows that these consist of a sandstone-rich matrix, a clay-dominated matrix and an iron-rich matrix.

#### *3.3.2.1.2 Fractures*

One can divide the samples of Dh4 in two different categories: those with visible fractures at a resolution of 56.61  $\mu\text{m}$  and those without. Samples C1, C3, C4 and C8 are those characterized by fractures. They are illustrated in figure 21. In this figure the samples are visualised by cross-sections in the Z-, X- and Y-plane, perpendicular to each other. They are also linked to their location in the core. The fractures are encircled in green and are visible in the cross-sections because they are characterized by a lower attenuation than their surroundings. The fractures in these samples were subjected to the fracture filtering script developed by Voorn et al. (2013) which successfully segmented the fractures in three from the four samples. For C1, the script was unable to segment the fractures. Possibly this is the result of the fact that this sample has a heterogeneous distribution of density in which there are areas with increased porosity and areas with an increased presence of dense minerals. It is mainly in these dense areas that the fractures occur. This heterogeneity however makes it more difficult to extract the fractures from the sample because the MSHFF script requires the definition of an average material greyscale value. Specifically this input factor is difficult to define unambiguously. Also in Morpho+ the fractures could not be separated as individual objects due to their location within the more dense areas of the rock. This has the effect that the fractures have an increased greyscale value which is similar to that of the matrix material. However, from cross-sections made in Morpho+ one can see that the fractures in C1 are nearly horizontal. Therefore the fracture size is more distorted in the Z-plane than in the X- and Y-plane. To get an idea of the fracture opening, their diameter can be measured in Fiji. This is illustrated in figure 25. In the X-plane, the fractures are characterized by a diameter of 2 to 4 voxels. This corresponds to a width of 113.2 to 226.4  $\mu\text{m}$ . Of course the accuracy in size of the fracture measured in this way is dependent on several parameters. First of all it is dependent on the resolution of the scanned image. A fracture with an opening smaller than the resolution will not be visible on the scans. Therefore the higher the resolution is, the smaller the fractures will be that can be visualized. This also means that the accuracy in which a fracture can be described is dependent on the resolution. Another parameter is the dip of the fracture. The true opening of a fracture can only be measured perpendicular on this fracture. The true opening of a horizontal fracture can thus be measured on the X- or Y-plane while for a vertical fracture, measurements on the Z-plane are necessary.

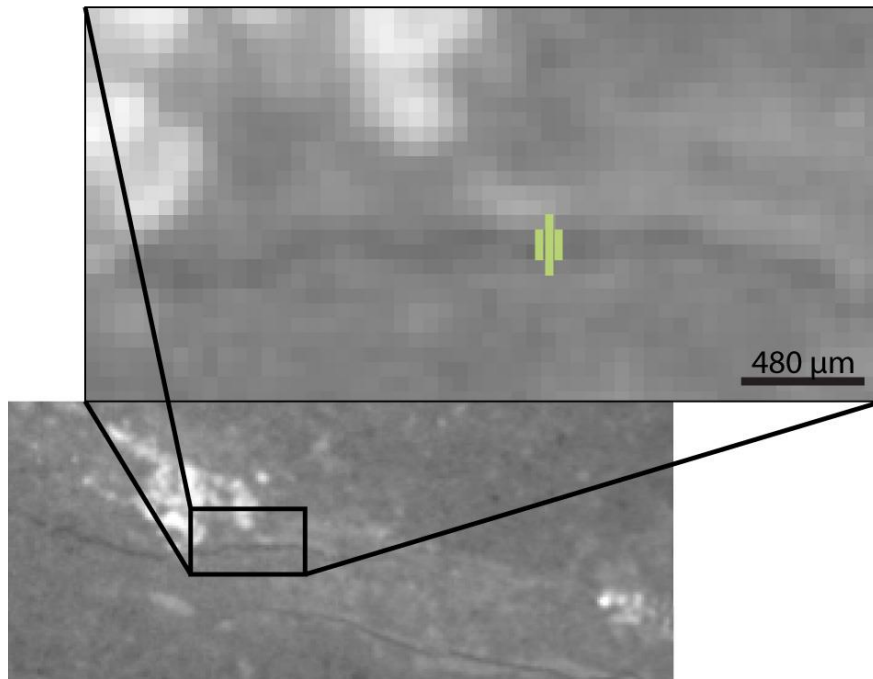


**Figure 25:** Illustration of a cross section in the X-plane of C1. The fracture, located within the more dens fractions of the rock, has a width ranging from 2 to 4 pixels or 113.2 to 226.4  $\mu\text{m}$ .

For C3, C4 and C8 the fractures were successfully segmented with the MSHFF script in Fiji after which they were exported to Morpho+. Here the fractures were visualized as objects from which the orientation and maximum opening could be calculated. In figure 26, the three stereographic projections of these objects in C3, C4 and C8 respectively are illustrated.

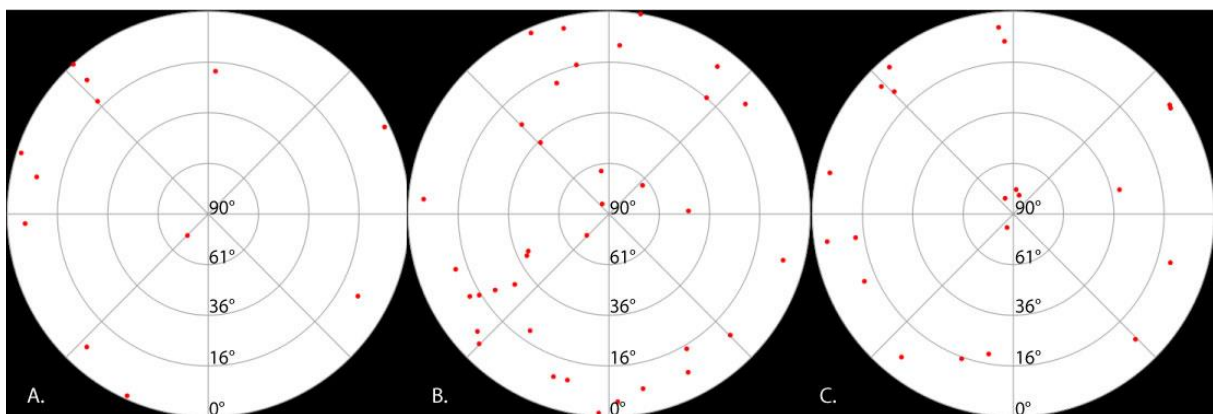


**Figure 26:** Stereographic projections of the fracture objects from C3 (a), C4 (b) and C8 (c). In this stereoplot the dip of objects is not linearly distributed. Therefore the dip angles are included in the figures.

Although the fractures are represented by a smaller amount of objects, a similar observation as with the fractures in the field samples can be made. In the stereograph of C3 (figure 26a) and that of C8 (figure 26c) one can differentiate between fractures with a semi-horizontal orientation with a dip lower than  $16^\circ$  and fractures with a vertical orientation and a dip between  $75^\circ$  and  $90^\circ$ . The stereographic projection of fractures in C4 shows a more differentiated pattern of orientation. However 22 from the 35 fracture objects of C4 have a dip smaller than  $16^\circ$ . Thus a significant fraction of the fractures in C4 can also be described as semi-horizontal. In both C3 and C4, the fractures are found in close proximity of dense structures within the rocks (described in the subdivision “fossils”).

Especially in C3, this structure which forms chambers and pathways seems to be the nucleation point of the fractures. In C4 they are related to an overall denser matrix which can be identified as more clay rich in the hand sample. The fractures form at the transition between clay and sand lenses. In C8 the fractures are linked to the regions of the rock with a lower iron-content. These are also the regions in which less ooids are found as compared to the iron-rich areas. Some of the fractures are found at the boundary between the iron-poor and iron-rich regions, but at least as much are located in the centre of an iron-poor area. To characterize the fractures in C3, C4 and C8 a representation of the maximum openings of the fractures is made in relation with their frequency. This is illustrated in figure 27a. The fractures were segmented in different objects in order to characterize one fracture by different measurements of maximum aperture. For C3 and C8 the majority of fractures have a maximum opening of 3 voxels or 169.8  $\mu\text{m}$ . One twelfth of the fractures in C3 and one sixth of those in C8 have a maximum opening of 5 voxels (283.1  $\mu\text{m}$ ). For C4 the distribution is different: the majority of fractures can be described with a maximum opening of 5 voxels while two seventh of all fractures have a maximum opening of 3 voxels wide.

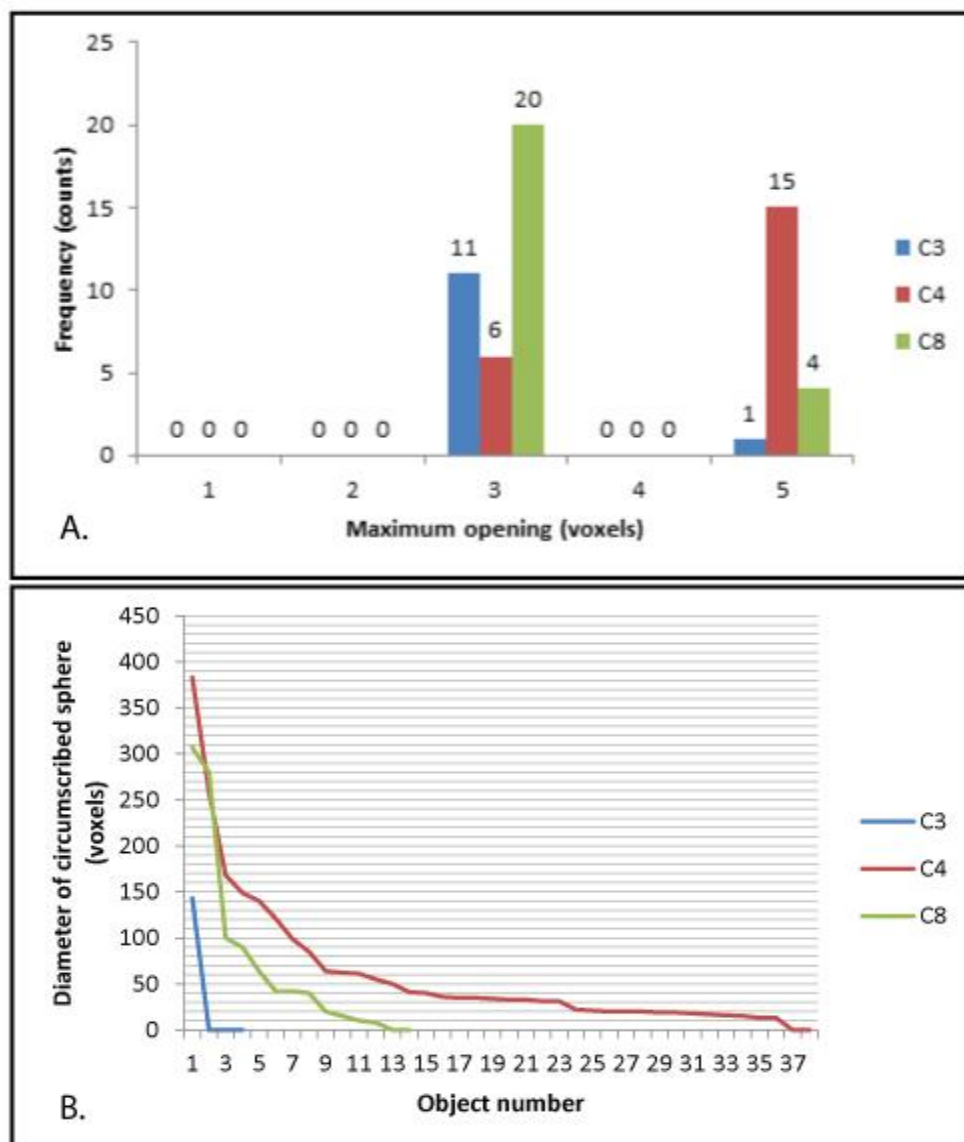


**Figure 27:** Graph A. is showing the distribution of the maximum opening of fractures from samples C3, C4 and C8. In graph B. the fractures are characterized according to their diameter of the circumscribed sphere. One voxel equals 56.61  $\mu\text{m}$ .



Another way of characterizing the fractures in a rock is by the length of the individual fractures. To determine this, each individual fracture was approached as one unique object. Subsequently the diameter of the circumscribed sphere around this object was calculated. To draw the graph illustrated in figure 27b, the diameter of the circumscribed spheres from all objects representing fractures were listed in descending order. The largest circumscribed sphere is obtained for fractures in sample C4. The ten largest fractures are ranged between diameters of 383 voxels and 62 voxels. This equals distances of 21.68 mm and 3.51 mm respectively. When all fractures are included however, the average diameter of the circumscribed fracture sphere is 3.58 mm. C8 is the sample characterized by the second largest length. Twelve fractures were evaluated, from which the five largest were characterized by a diameter of circumscribed sphere of 307 voxels (17,38 mm) to 64 voxels (3.62 mm). As an average diameter 84.83 voxels was calculated. This equals a distance of 4.80 mm. In C3 only 1 fracture was obtained. This is characterized by a circumscribed diameter of 143 voxels which equals 8.10 mm.

#### 3.3.2.1.3 Fossil-content

Both in samples C3 and C4 a network of dense material runs through the rock. This material is found to be pyrite upon inspection of a polished section under the microscope with reflected light. The pyrite in the samples forms both in C3 and C4 a network of tubes connecting different chambers. Thanks to the descriptions and sketches in Bromley & Frey (1974) this network can be identified as the burrow system of *Upogebia affinis*, or coastal mud shrimp. Present-day species are often found in mud- or silt-rich sediments in an estuarine setting (Williams, 1984). Typical for their burrows is that the chambers have rough surfaces, while the tubes are smoother (Bromley & Frey, 1974). Forbes (1973) described similar burrows with chambers in which the swellings acted as breeding chambers. This is however not the function of the chambers of *Upogebia affinis*, because the larvae are regularly found in the oceanic plankton (Sandifer, 1974). Since the burrows in sample C3 and C4 are now filled with pyrite, it is fairly easy to extract them and visualise them in VGStudio MAX®. The result of this visualisation is illustrated in figure 28. In sample C3 (figure 28a and 28b), four large chambers are interconnected. Here the thresholding was carried out in Morpho+ after which the result were exported to VGStudio MAX®. Sample C4, consisting of a number of tubes and smaller chamber than those in C3, was visualised and segmented fully in VGStudio MAX®.

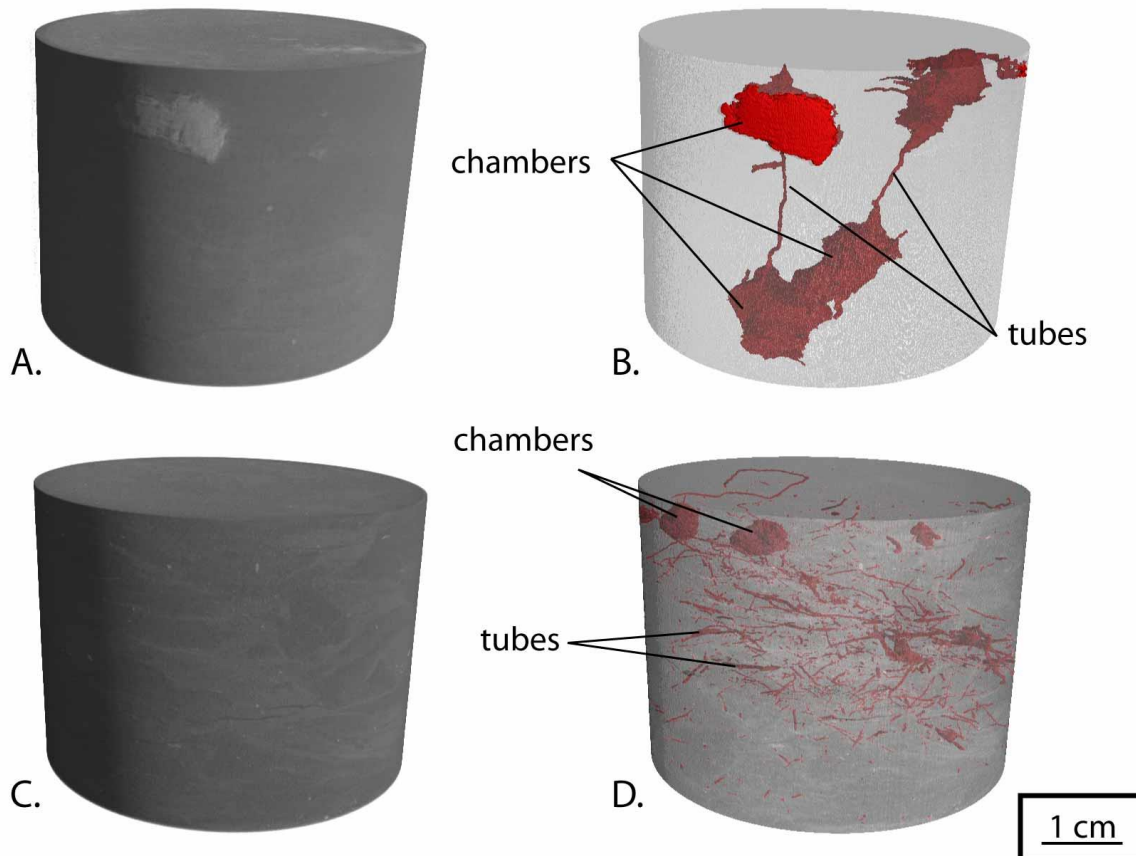


**Figure 28:** Visualisation of both outer look of samples C3 (a) and C4 (c), and the distribution of pyrite inside the samples in which the sample was visualised with a transparency of 60 % so that the coloured pyrite would be visible. In C3 larger pyrite chambers (b) are formed than in C4 (d). The dense network in C3 was extracted by segmentation in Morpho+, while in C4 it was directly visualised in VGStudio MAX®.

#### 3.3.2.1.4 Porosity

When fractures are not regarded as porosity, only three samples from Dh4, scanned at the resolution of 56.61  $\mu\text{m}$  show an indication of porosity. However, most of the porosity of the samples cannot be visualised at this resolution. This indicates that most of the pores in the samples are smaller than 56.61  $\mu\text{m}$ . The three samples in which some of the porosity is visible are: C1, C2 and C7. Not surprisingly these are the three samples which have the highest porosity from the 8 scanned samples. Porosity thresholding in Morpho+ gives an overall porosity (open + closed) of 5.75 vol% in C1. This is 6.83 vol% too little in order to account for all the open pores in the sample as determined by laboratory tests. A similar story can be told for C2 and C7. The thresholded porosity in C2 only accounts for 1.93 % of the entire sample volume as where the calculated porosity in laboratory test was determined at 10.71 vol%. In C7, which has a calculated porosity of 12.96 vol%, only 3.07 vol% of the porosity is represented by pores larger than 56.61  $\mu\text{m}$ . As illustrated in figure 23 however, the fact that some of the porosity is visualised can be used as a base to decide where to take subsamples for a following scan with a higher resolution.

#### 3.3.2.2 Scans at resolution 4 $\mu\text{m}$

Three subsamples with a diameter of 5 mm were taken from Dh4 and were scanned with a resolution of 3.99  $\mu\text{m}$ . They were paced at a SOD of 27.42 mm which gave a magnification of 31.47

times. Between the samples and the source a 1 mm thick aluminium plate was placed as a hardware filter for beam hardening effects. The samples, C1, C3 and C7 will be discussed in this order.

#### 3.3.2.2.1 C1

The subsample in C1 was taken from the region in the sample in which porosity could be seen in the scans with the resolution of 56.61  $\mu\text{m}$ . This was done in order to characterize the porosity in the sample with a higher resolution. The images, illustrated in figure 29, reveal a fairly homogeneous rock sample in which beside the quartz grains also some glauconite can be recognized. Between the grains, an interparticle porosity can be differentiated. At some places, evenly distributed within the sample, this pore space has undergone a secondary infill with a material of clay, or iron-rich signature. This leads to a decrease in porosity. Some of the pores might originate from a preferred dissolution of material and could be described as moldic. They are characterized by a circular to hook shape as emphasized in figure 29. Analysis of the porosity in Morpho+ resulted in a total porosity of 4.48 vol% from which 3.20 vol% was characterized as open porosity.

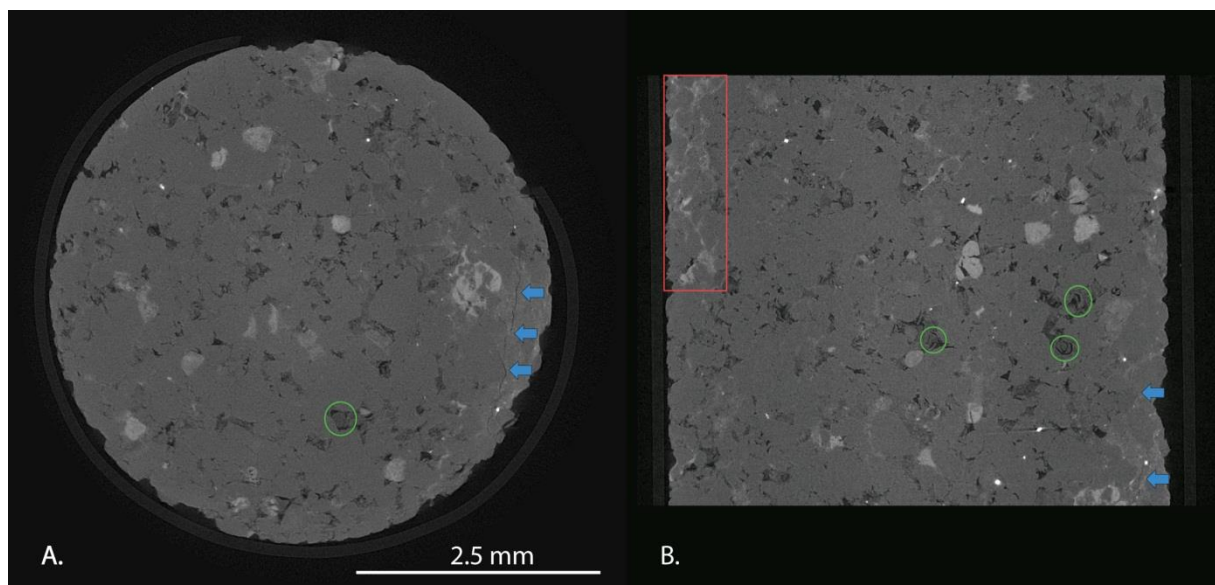


**Figure 29:** Cross-sections along the Z-plane (a) and Y-plane (b) of C1. Encircled in green are pores with a circular to hook shape which represent dissolution features. The blue arrows indicate the location of a fracture. The area between this fracture and the side of the sample is only wide enough for one grain. In the rectangular area indicated in red (figure 29b), the pore space is taken by clays.

In some cross-sections in the Y- and Z- direction small fractures can be observed. However, when present, these fractures are found at the side of the subsample with a vertical orientation. They propagate through the sample by following existing grain contacts and the maximum distance from the side of the subsample is precisely one grain. Therefore, it is unsure to what degree these fractures are primary to the rock, or whether they are the result of the drilling during the subsampling phase.

#### 3.3.2.2.2 C3

A subsample of C3 was taken in order to characterize the ground mass in which the pyritised structures, seen in the scans with a resolution of 56.61  $\mu\text{m}$ , are formed. The cross-sections through this scan along the Z- and X-plane are illustrated in figure 30a and 30b.

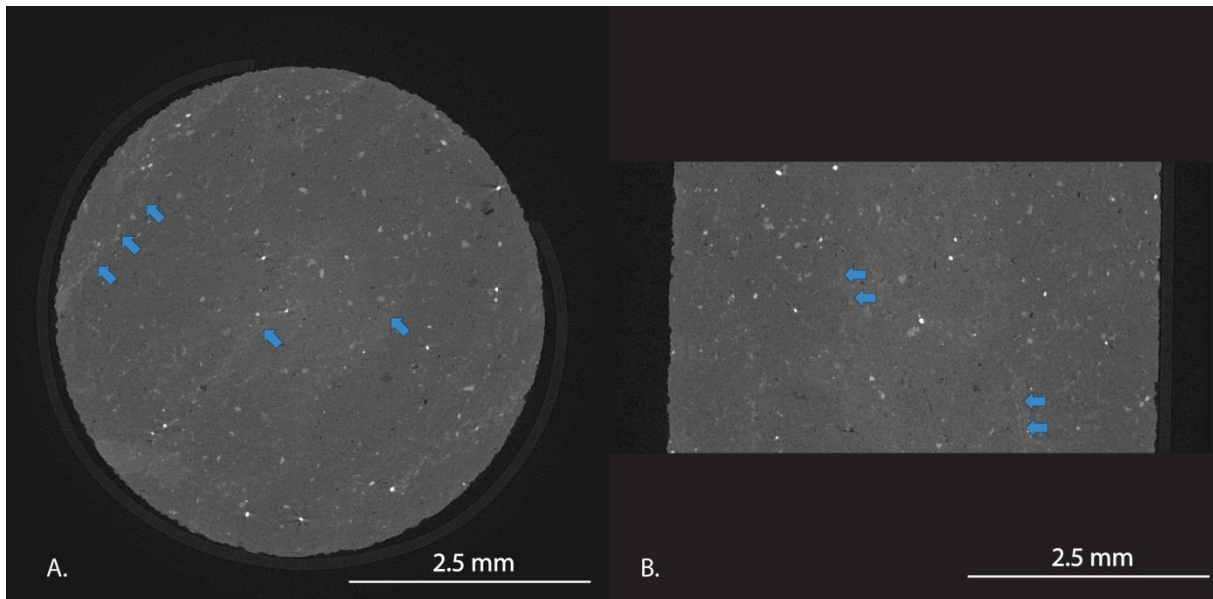


**Figure 30:** Cross-sections of sample C3 along the Z-plane (a) and the X-plane (b). In both cross-sections one can identify fractures along area which are enriched in clay. They are indicated with blue arrows.

The cross-sections illustrate a homogeneous rock sample in which small fractures can be identified. After segmentation of these fractures, a stereographic projection was made of their orientations. This is illustrated in figure 31a. The fractures can be classified in two groups: one with orientations plotted along the blue line and a second group with orientations indicated by the yellow crosses. The fractures with orientations along the blue line illustrate fractures which are lying in a plane along the Z-direction of the subsample. When this orientation is brought back to a lower resolution, this equals a horizontal direction in the core. The fractures with an orientation around the yellow crosses then equal those lying in a plane perpendicular to the fractures in the horizontal plane. From the scans at lower resolution, it is known that fractures occur with a horizontal and vertical component.

For the characterization of aperture and length of the fractures, figures 31b and 31c are given. In figure 31b, the distribution of the maximum opening of fractures is illustrated, as it was calculated on segmented parts of the fractures in order to give a better distribution. Most of the fractures are characterized by maximum openings of 3 voxels, although a significant amount of them shows maximum openings of 5 voxels. This equals 11.97  $\mu\text{m}$  and 19.95  $\mu\text{m}$  respectively. One of the 195 counted objects in which the different fractures were segmented even has a maximum opening of 7 voxels (27.93  $\mu\text{m}$ ). In order to give an idea of the lengths of the fractures, the distribution of diameters of circumscribed spheres is given in figure 31c. For this calculation, the fractures were not segmented. 568 voxels is the maximum circumscribed diameter measured in the fractures. This equals 2.27 mm. Besides from this fracture, 17 other are characterized by a circumscribed diameter larger than 100 voxels. The average circumscribed diameter from the fractures in C3 is 57.43 voxels which equals a distance of 229.15  $\mu\text{m}$ .

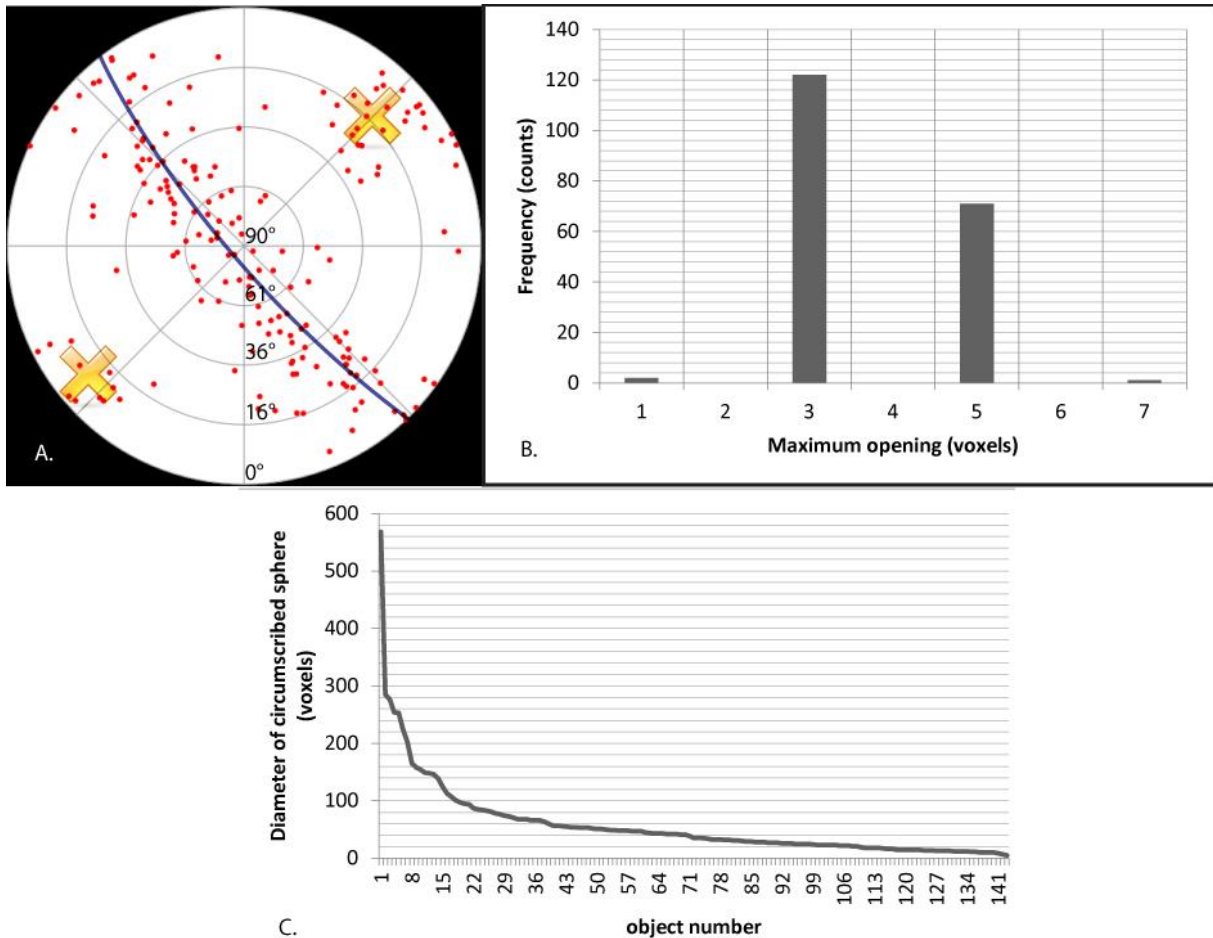


**Figure 31:** Illustration of the stereographic projection of the fracture orientation in the subsample taken from C3 (a). Most of the fractures are plotted along the blue line, while a second group of fractures is plotted around the yellow crosses. In figure 31b, the distribution of the maximum opening of fractures is given. Figure 31c gives the distribution of the diameters of circumscribed spheres for the fractures. One voxel equals 3.99  $\mu\text{m}$ .

### 3.3.2.2.3 C7

In C7 a subsample was taken in a region of the rock poor in iron. This was done, because this is the region of the rock in which traces of porosity were visible when scanned with a resolution of 56.61  $\mu\text{m}$ . Although there were still some parts where the pores were filled with a secondary mineralisation, a large part of the porosity could be extracted. The grains seem to be more loosely packed than those in C1, resulting in a larger interparticle porosity. Also the pores seem to be better connected. A total porosity of 10.11 vol% was obtained in this sample with an open porosity of 9.81 vol%. These seem to be excellent values for flow simulations in E-core. Further, the sample was not characterized by any fossils or fractures. A cross-section along the Z-plane of the sample is shown in figure 32a. Figure 32b is a 3D rendered image of a part of the subsample in which the porosity was extracted and visualised in blue. A clipping plane allows for a 3D visualisation of both the sample, in which the individual grains can be identified, and the porosity, visualised in blue in figure 32b.

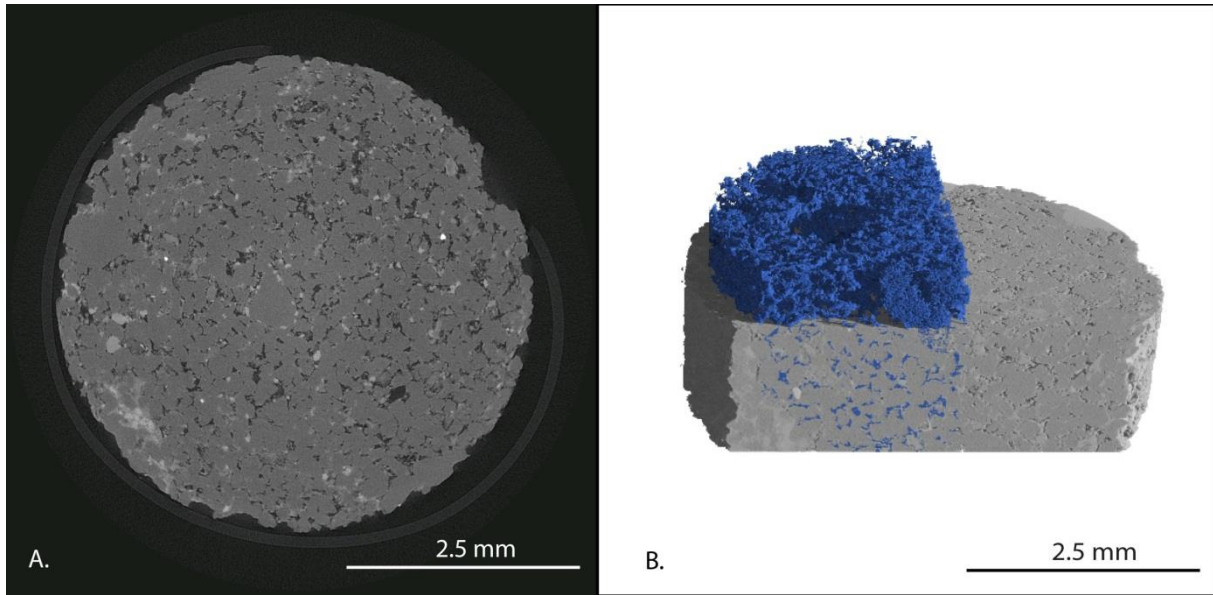


**Figure 32:** Cross-section along the Z-plane of subsample C7 (a) in which pores and pore-filling mineralisations can be observed. In figure 32b, a 3D visualisation is given from the subsample in which the porosity is extracted and visualised in blue.

### 3.3.2.3 Scans at resolution 2.8 $\mu\text{m}$

Two samples, C4 and C6 were scanned with a resolution of 2.8  $\mu\text{m}$ . The SOD was 19.19 mm, which resulted in a magnification of 44.96 times. Only the beam hardening filter implemented in Octopus was used since no hardware filter was placed between the X-ray source and the sample. Both subsamples were taken from sandstone intervals in the heterogeneous samples. In the subsample taken from C4, the distinct pyrite tubes can be recognized due to their elevated attenuation, as can be seen in the cross-sections through the sample illustrated in figure 33a and 33b. However, the most important features which can be recognized in this sample are the fractures.

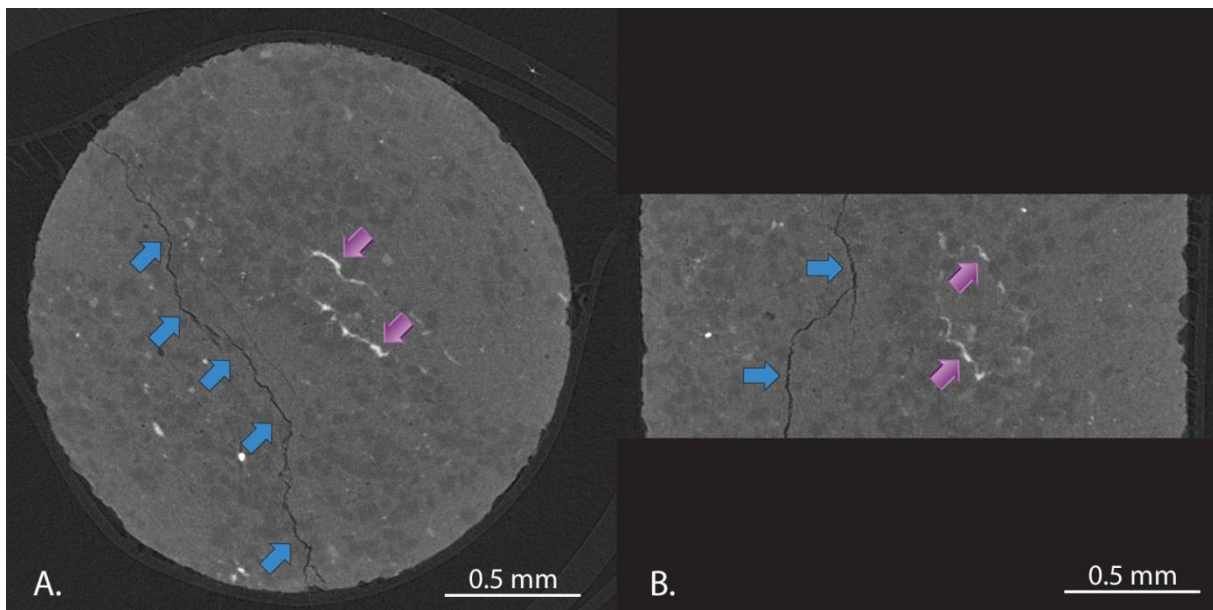


**Figure 33:** Cross-sectional representation of subsample C4 along the Z-plane (a) and the X-plane (b) of the subsample. With blue arrows, fractures are indicated, while the purple arrows indicate minerals with a high resolution, probably pyrite tubes.

The fractures were segmented with the script from Voorn et al. (2013) and the orientations of the fractures were plotted in figure 34a. However, since the calculation speed is dependent on the amount of cross-sections in the vertical direction, the fracture segmentation was limited to a representative section of the scan. Most of the fractures plot within the neighbourhood of the blue line indicated in figure 34a. This indicates an overall orientation along the Z-plane of the subsample. When translating this to the core it represents a horizontal direction.

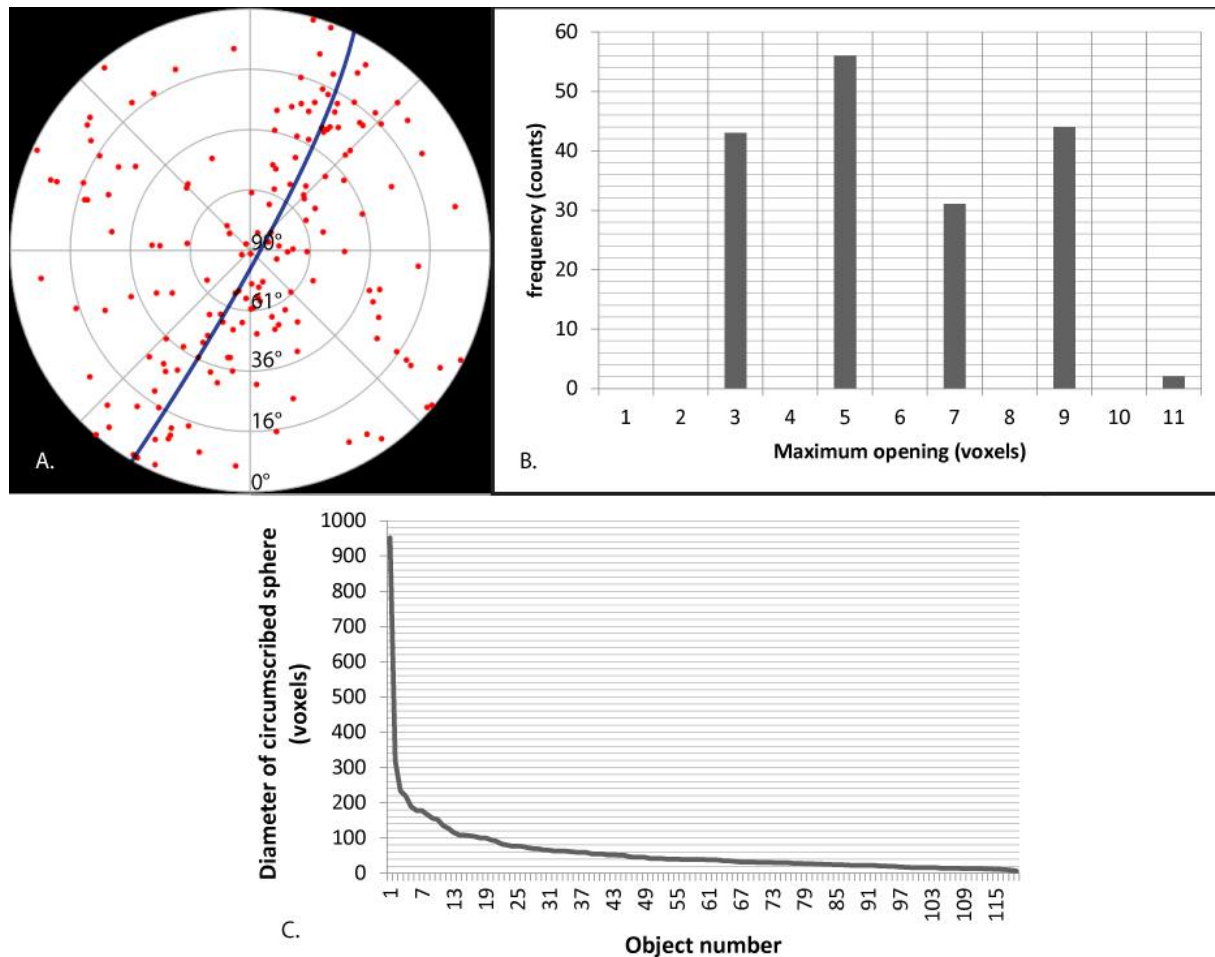


**Figure 34:** Stereographical projection of the fracture orientations in the subsample C4 (a). Most of the fractures are orientated along the blue line, indicating an overall orientation along the Z-plane of the subsample. In figure 34b the distribution of the maximum opening of the analysed fractures is given and figure 34c gives the distribution of the circumscribed diameter of the fractures. For both figures 34b and 34c, one voxel equals 2.8  $\mu\text{m}$ .

In figure 34b the distribution of the maximum fracture openings is visualised. For this calculation, individual fractures were segmented in different objects. Doing so, the amount of information which can be subtracted increases. Most of the fractures are characterized by a maximum opening of 5 voxels (14  $\mu\text{m}$ ). However, a significant amount of the fractures (44 of the 175 segmented objects) is characterized by a maximum opening of 9 voxels (25.2  $\mu\text{m}$ ). Even two of the segmented objects show a maximum opening of 11 voxels (30.8  $\mu\text{m}$ ). Figure 34c illustrates the distribution of the circumscribed diameter of fractures. For this calculation each fracture was treated as an individual object. The largest circumscribed diameter measures 951 voxels, or 2662.8  $\mu\text{m}$ . However, since the fracture at issue is found to be present in the lower-most analysed cross-section, this value is most likely not the true circumscribed diameter of this fracture. This fracture probably continues in the rock sample in the area which was not analysed for fractures. However, it is the only fracture in this

subsample for which this observation is true. The other circumscribed diameters are calculated for fractures which have their start and end in the analysed fraction of the scan. The average circumscribed diameter for the fractures is 62.47 voxels, or 174.9  $\mu\text{m}$ .

The subsample taken from C6 consists mainly of quartz grains. A cross-section of this scan along the Z-plane is illustrated in figure 35a. The grains, as well as the porosity, were thresholded in Morpho+ and visualised in 3D in figure 35b. In this figure, the quartz grains are represented by a different greyscale value according to their classification on the base of the surface value of each grain. This value is a measure for the size and counts the amount of voxels out of which the surface of the grain consist. The porosity of the sample was determined at the value of 6.86 vol% and is illustrated in blue in figure 35b. In some cross-sections small fractures can be identified. However, they do not occur sufficiently in order to segment them with the MSHFF script. Measurements directly on the cross-sections reveal apertures of 3 to 5 voxels which equals 8.4  $\mu\text{m}$  to 14  $\mu\text{m}$ .

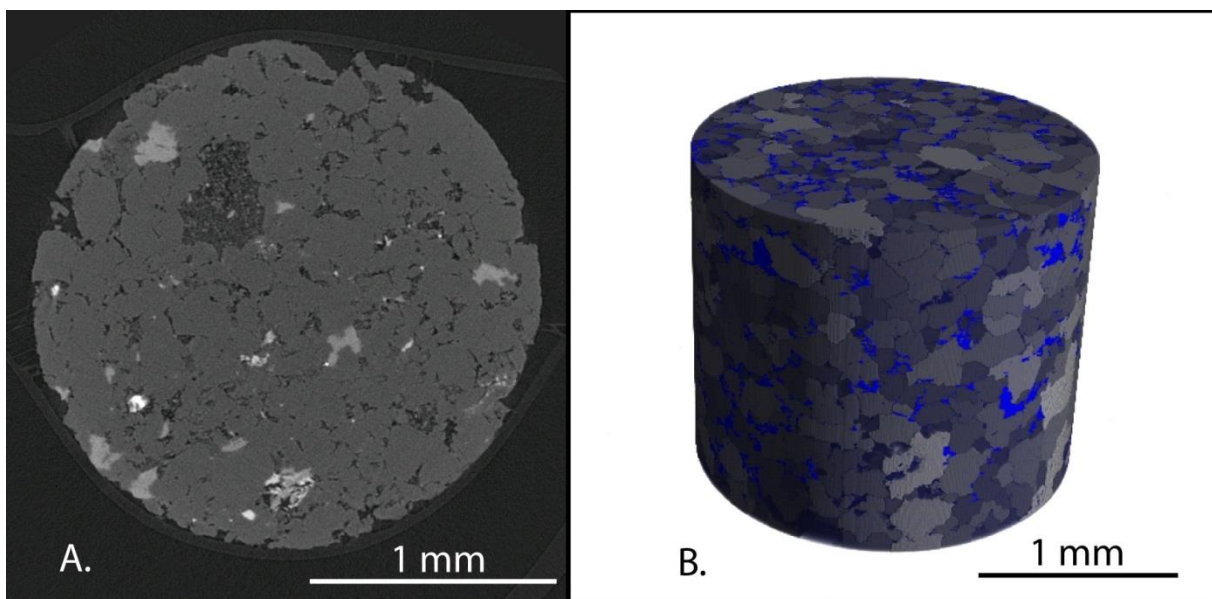


**Figure 35:** Cross-section of sample C6 at a resolution of 2.8  $\mu\text{m}$  (a). One can identify the quartz grains and porosity. These are represented in figure 35b: this 3D rendered image shows the quartz-grains classified according to their surface value and the porosity in blue.

### **3.3.3 Dh2 Samples (D-samples)**

The samples taken from core Dh2 are characterized by an initial diameter of 4.1 cm. This is slightly smaller than the samples of Dh4. A first set of scans was carried out with a resulting resolution of 62.56  $\mu\text{m}$ . Subsequently subsamples were taken with a diameter of 5 mm from which scans with a resolution of 4  $\mu\text{m}$  were obtained. Even smaller subsamples were taken from D2 and D3. These had a diameter of 2 mm and were scanned with a resolution of 2.7  $\mu\text{m}$ . For the analysis of the samples a slightly different approach is used as with the samples of Dh4: the scans will be discussed from low to high position in the core. So first D3 will be discussed, followed by D2 and then D1. In these discussions scans from different resolutions will be used to characterize the samples. Special attention for the general structures which are visible at the given resolution will be highlighted. Neither in D1, D2 or D3 fossils were found. To start with, a general illustration is given from all three samples at a resolution of 62.56  $\mu\text{m}$  (figure 36). For this set of scans, the samples were placed at a SOD of 214.43 mm which resulted in a magnification of 4.02 times. Two hardware filters were placed



between the X-ray source and the sample in order to limit the beam hardening effect. It concerns a 1 mm thick aluminium plate and a 0.3 mm thick copper plate. Since D1 only represents a sandstone sample in which a heterogeneity is given by a difference in matrix, it will not be described in detail. Special features such as fractures or visible porosity are lacking from it.

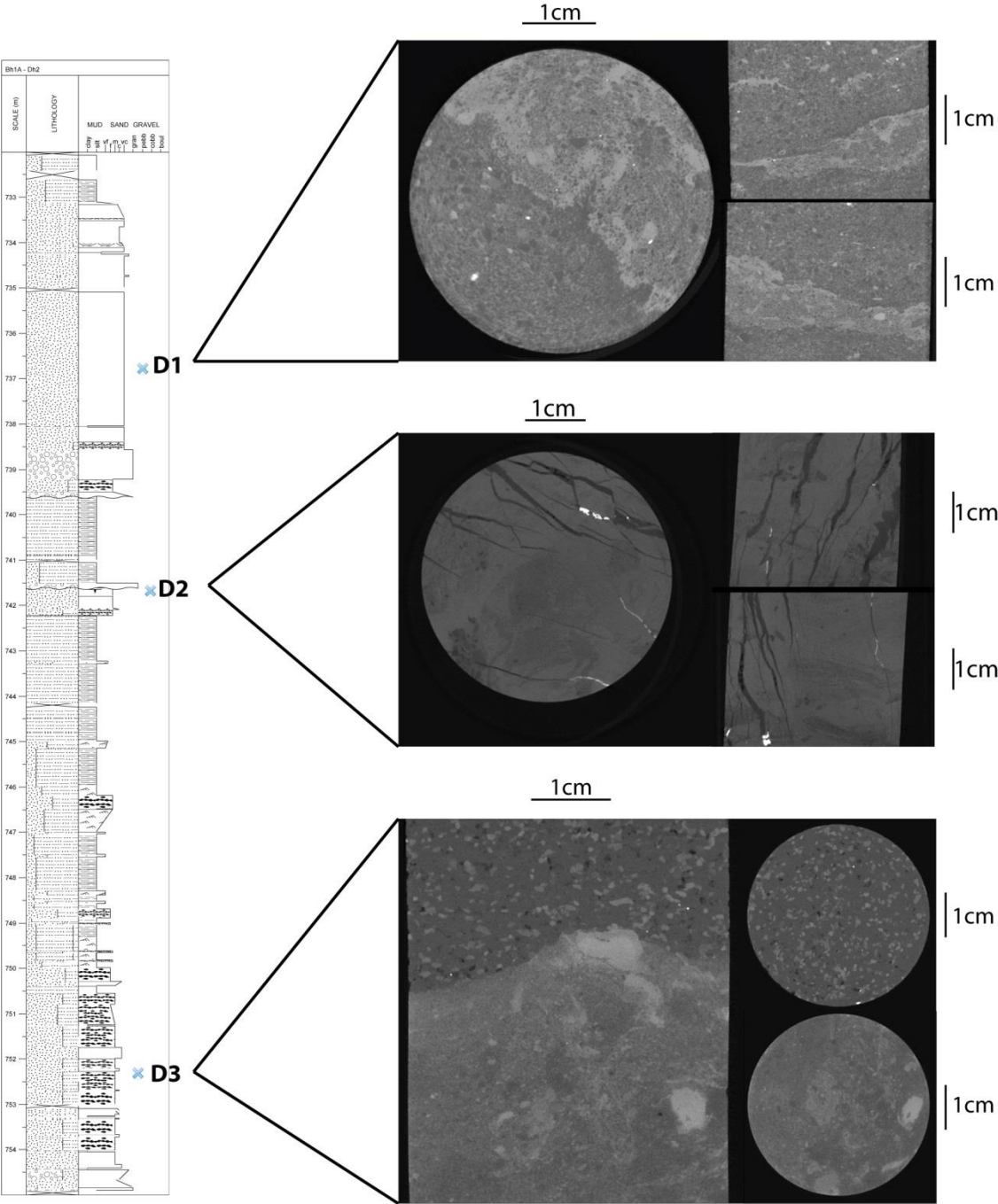


**Figure 36:** Overview of the scanned samples from Dh2, linked to their location in the core. Neither in sample D1 or D3 fractures can be distinguished. In these samples the attention is drawn to the heterogeneity of the samples. In D1 two different matrixes are present while D3 is composed of two entirely different lithologies. In D2 the fractures are the most important features. They were already visible in the hand specimen, but now it is possible to visualise the fractures in 3D.

### 3.3.3.1 D3

D3 is clearly heterogeneous: the sample is composed of two different lithologies which pass into each other via an abrupt transition. The upper part consists of coarse sandstone mainly built of quartz. The lower part is made out of generally smaller grains and an important amount of clay. This gives rise to a secondary heterogeneity within this sample. In none of both lithologies fractures can be distinguished. What can be distinguished is the porosity. Laboratory tests calculated the open porosity at 4.71 vol%. However, at the resolution given in figure 36, porosity is only visible in the upper part, consisting of coarse sandstone. If only this part is considered, the porosity that can be extracted in Morpho+ accounts for only 2.06 % of the total volume. Although the upper part is likely the main contributor of the porosity of D3, most of the pores cannot be visualised. Therefore, there have to be pores smaller than 62.56  $\mu\text{m}$  in both the upper part of D3 and in the lower to account for a total open porosity of 4.71 vol%. It is thus interesting in subsampling both the upper and lower part of the sample in order to check the porosity distribution.

A subsample with a diameter of 5 mm was taken from the upper part of D3 and subsequently scanned with a resulting resolution of 3.99  $\mu\text{m}$ . The lower part of the sample is represented by another subsample. This subsample was characterized by a diameter of 2 mm. The scan of this subsample has a resolution of 2.8  $\mu\text{m}$ . The results of both scans are illustrated in figure 37. Figure 37a represents the coarse upper part and figure 37b the subsample of the lower part.

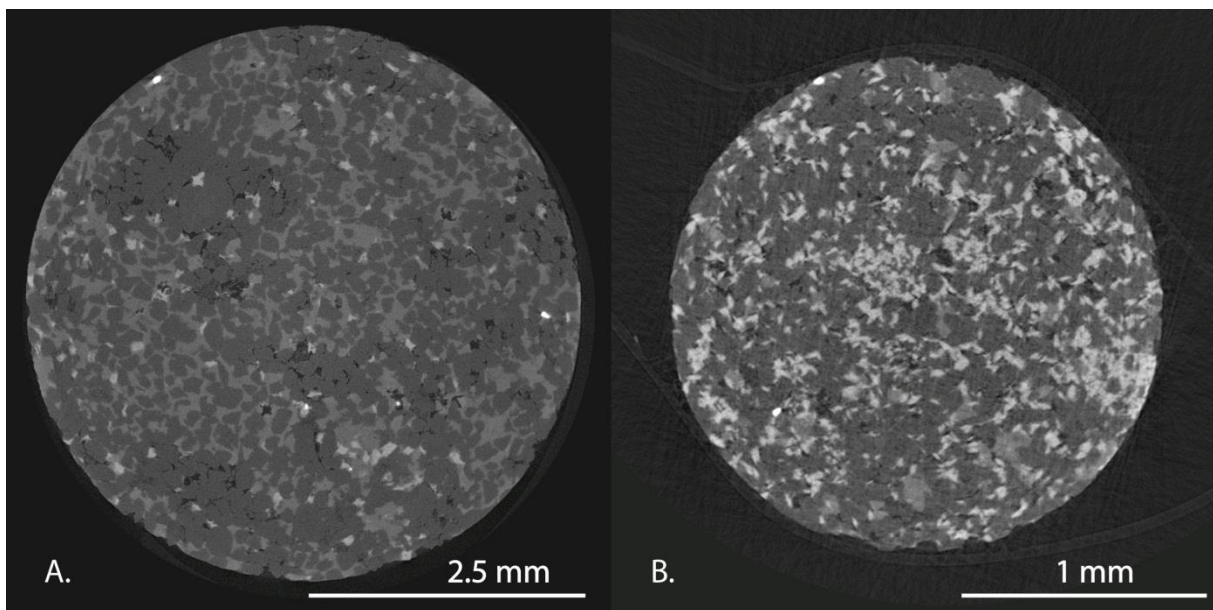


**Figure 37:** Cross-section along the Z-plane of subsamples taken from D3. Figure a represents the upper part of D3, consisting of coarse sandstone. It was scanned with a resolution of 4  $\mu\text{m}$ . Figure b is the fine grained lower part of D3, scanned with a resolution of 2.8  $\mu\text{m}$ .

In both the upper part and the lower part, the porosity can be extracted from the scanned images. In the coarse sandstone a total porosity of 2.25 vol% is obtained. This is slightly more than the porosity obtained from the same sample scanned with a lower resolution. In the lower part the porosity, limited by a resolution of 2.8  $\mu\text{m}$  was calculated to be 2.45 vol%. This somewhat unexpected result indicates that the porosity in both the upper part and lower part of D3 is similar.

### 3.3.3.2 D2

The most important features in D2 are without doubt the fractures. They occupy more than 10 % of the entire volume in the sample and are predominantly closed, although some pores can be distinguished within them. In total, the pores represent 0.2 % of the entire rock volume. Thanks to the morphology of the fractures, one can conclude that they were formed during two different stages of faulting. This resulted in two sets of fractures with the latest set superimposed on top of the previous. This superposition occurred with an angle of approximately 60°. Both fracture sets are nearly vertical and filled in with the same material. This implicates that the infilling took place after the formation of the secondary fracture set. The fractures can be thresholded in Morpho+ and after segmentation of each fracture in different objects, a stereographic projection of the fracture orientations can be made. This is given in figure 38a. The fractures which are plotted on the blue line are lying in a nearly vertical plane. They are part of the first set of fractures. The second set of fractures plots around the yellow cross.

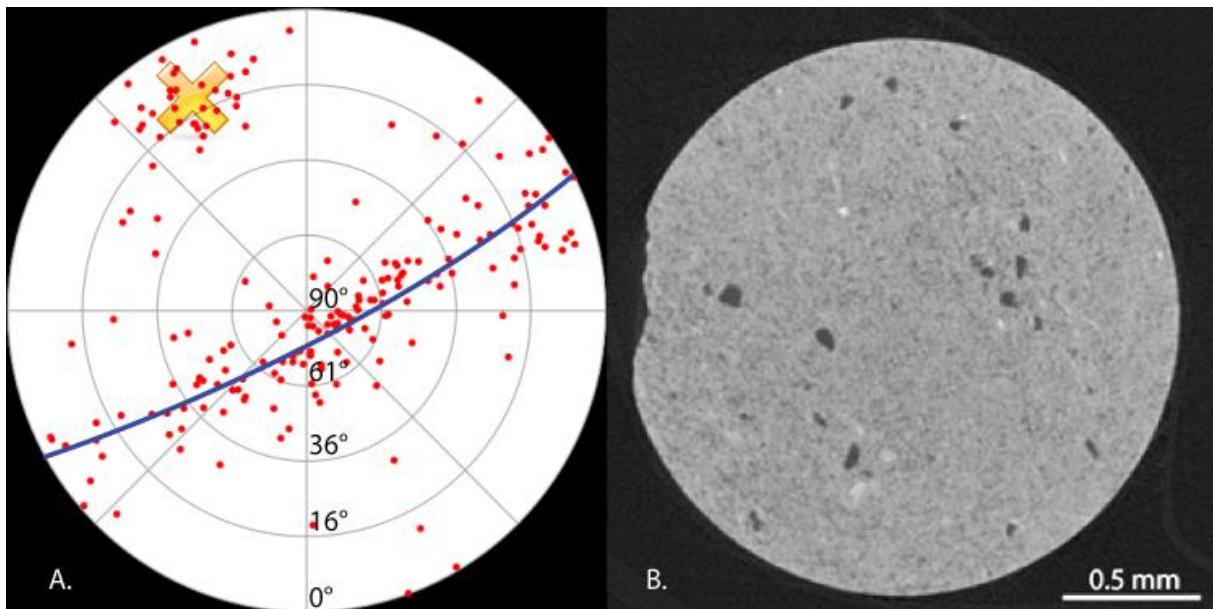


**Figure 38:** Stereographic projection of the fracture orientations in scans with a resolution 62.56  $\mu\text{m}$  of sample D2 (a). Two main orientations can be observed. They are indicated with the blue line and yellow mark. In figure 38b, a characterization is given of the ground mass in which these fractures occur. This cross-section is scanned with a resolution of 1.68  $\mu\text{m}$  and shows porosity.

The statistical analysis of the fractures shows that most of them are characterized by a maximum width between 8 and 10 voxels wide. In this resolution this result translates to 500  $\mu\text{m}$  and 625  $\mu\text{m}$ . However ten of the fractures segmented from the scan had a maximum opening between 24 and 28 voxels. This corresponds to spheres with diameters from 1.5 mm and 1.75 mm.

In order to characterize the ground mass in which these fractures occur, a subsample was taken from a section in D2 which is not affected by the fractures. This subsample had a diameter of 2 mm and was scanned at a slightly higher resolution than the other samples of this diameter. The obtained resolution was 1.68  $\mu\text{m}$ . A cross-section along the Z-plane through this subsample is illustrated in figure 38b. This illustrates the overall clay-content of the sample with thinly distributed coarser grains and a porosity which is visible of 0.83 vol%.

### 3.3.3.3 D1

Sample D1 is a sandstone sample characterized by the presence of ooids and two different matrixes. It was characterized by scans at two resolutions. The first scans had a resolution of 56.61  $\mu\text{m}$ , after which a subsample was taken. This was scanned at a resolution of 3.99  $\mu\text{m}$ . In figure 39a and 39b, the results of both scans are illustrated by a cross-section perpendicular to the Z-direction of the sample. This corresponds to a horizontal cross-section for figure 39a and a vertical cross-section for figure 39b when they are linked to the core. The scan with the lowest resolution (figure 39a) shows a heterogeneous distribution of an iron-rich matrix in which ooids and mineral grains are found. The scan at higher resolution (figure 39b) shows an overall porosity of 0.96 vol% as well as fractures, separating different grains in the sample. Due to the heterogeneous nature this subsample it was not possible to separate the fractures from the pores with the MSHFF script by Voorn et al. (2013). Measurements on cross-sections along the Z-plane of the subsample however indicated that the fracture apertures are 2 voxels to 6 voxels wide. At this resolution, this corresponds to 7.98  $\mu\text{m}$  to 23.94  $\mu\text{m}$ . One can thus without doubt speak of micro-fractures to characterize these.

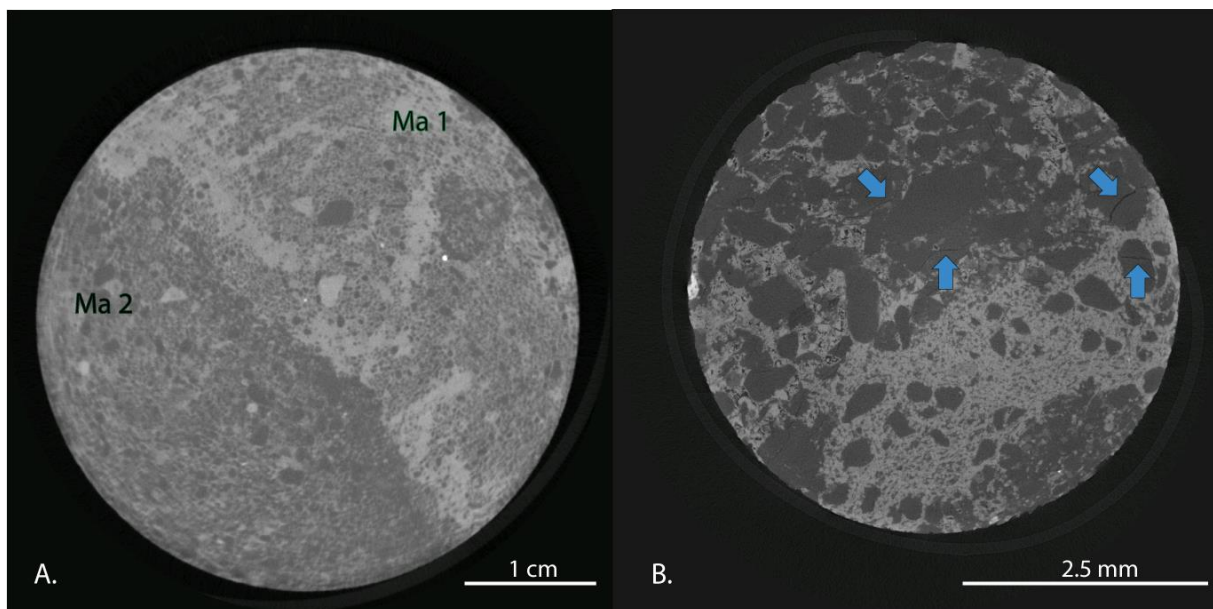


**Figure 39:** Horizontal cross-section from a scan of D1 with a resolution of 62.56  $\mu\text{m}$  (a). A difference in matrix is visible in this scan, indicated by 'Ma 1' and 'Ma 2' in figure 39a. A subsample was taken from this sample in Ma 1. This subsample was scanned with a resolution of 3.99  $\mu\text{m}$ . A vertical cross-section of this subsample is illustrated in figure 39b. Blue arrows indicate micro-fractures in this subsample.

## **3.4 Rock modelling**

Four scans were selected for analysis in E-core on the basis of their open porosity and the results from the high resolution scans. They are all sampled from Dh4 and are, starting from the deepest: C1, C3, C6 and C7. The scans which formed the basis of the analysis all had a resolution of 3.99  $\mu\text{m}$ , except for sample C6 where the obtained resolution was 2.8  $\mu\text{m}$ . Of these samples, pore networks were extracted, which formed the basis for flow simulations when possible. Subsequently MICP tests were simulated and for C6 and C7 the absolute permeability was calculated on the extracted pore space. The results are listed below according to the simulation. First the different pore networks will be discussed together with MICP results, followed by the flow simulations of  $\text{CO}_2$  and the absolute permeability measurements on C6 and C7.

### 3.4.1 Pore network characterization

To visualise the pore network in the samples, the pores first were segmented in Morpho+. Subsequently, the image stack in which the pores were thresholded was cropped into a bar to cube shape so the entire image stack represented the rock and the air outside of the sample was eliminated. The pores and grains then were given a designated greyscale value so that E-core could recognize them as such. Subsequently, the image stack was imported in E-core after which the analysis could start. The pore network of the four samples is illustrated in figure 40 as a ball-and-stick model in which the pore bodies are represented as red balls and the pore throats as white sticks.

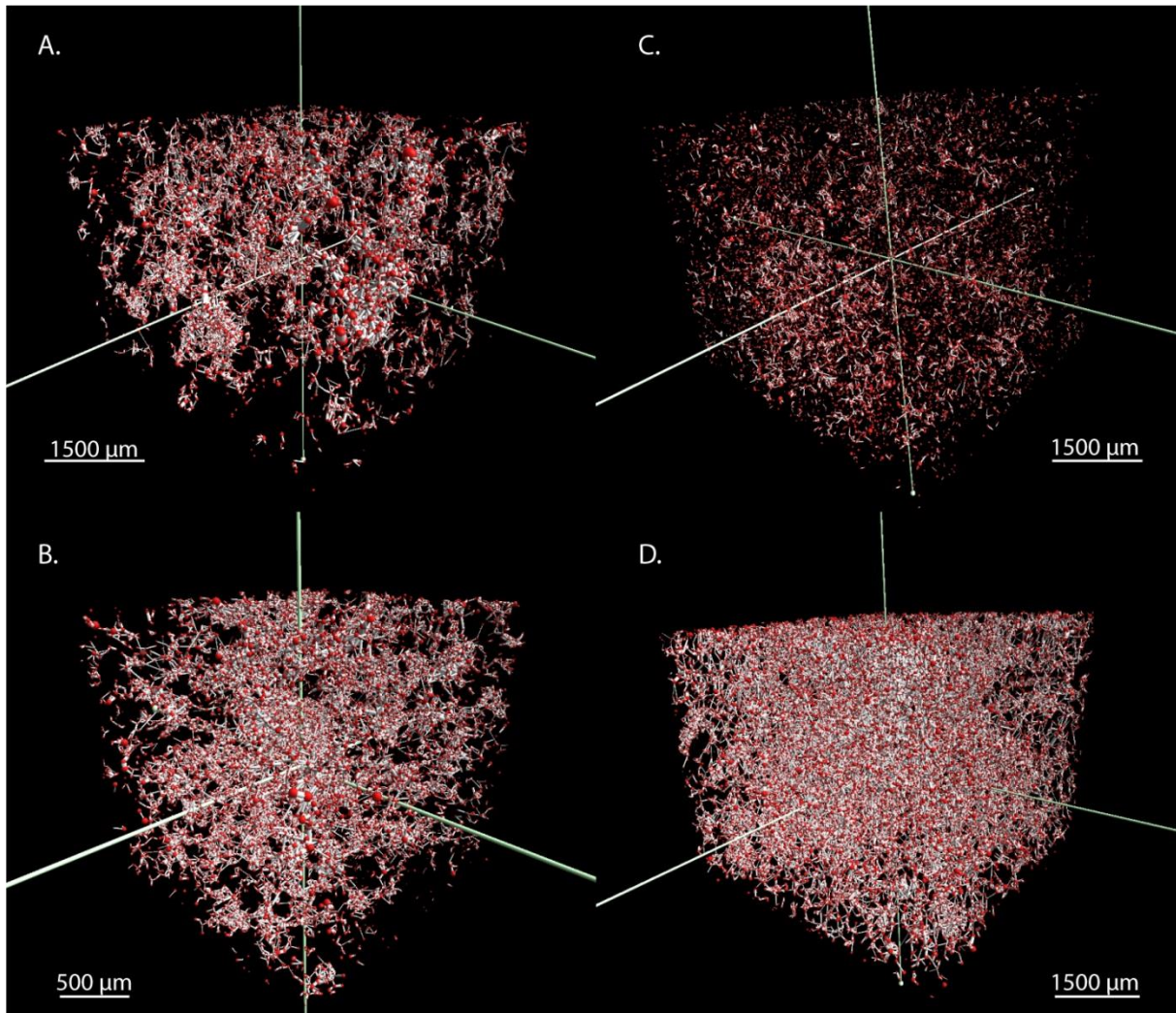


**Figure 40:** Representation of the pore networks in C1 (a), C3 (b), C6 (c), and C7 (d). Notice the scale bar difference between figures 40 a, b, d and figure 40c. For visualisation reasons, only a part of the total volume which was used for the analysis is represented in these models.

In figure 40a the pore network of sample C1 is given. A porosity of 4.48 vol% is obtained from which 1.653 vol% represents the percolating, or open porosity of the rock. The pore network is built from 17942 nodes from which 17931 have a triangular shape. The average radius of the pore bodies is calculated at 11.3  $\mu\text{m}$  with a maximum pore radius of 71.59  $\mu\text{m}$ . Overall this network is too tight in order to simulate flows through the pores, or to calculate an absolute permeability from it. Similar results are found for C3 (figure 40b), with a total porosity of 2.9 vol% and a percolating porosity of only 0.3215 vol%. The network consists of 26287 pore bodies, from which the majority, 26240 pore

bodies to be precise, has a triangular shape. The average pore radius is 8.50  $\mu\text{m}$  and the maximum pore radius within this sample is 36.46  $\mu\text{m}$ . This network is even tighter than the one representing the porosity in C1. Therefore it is not suited for flow simulations or permeability measurements. The MICP data for both C1 and C3 shows a stepwise intrusion of mercury with increasing pressure instead of a smooth curve. However, it does give an idea of the overall pore size distribution. In C1, most of the pores are characterized by a radius of around 10  $\mu\text{m}$ . Significant mercury intrusion started at a pressure of 0.66 bar, which corresponds to a pore radius of 11  $\mu\text{m}$ . In C3, the starting pressure with significant mercury intrusion is found at 1.41 bar. Mercury started to intrude in pores with a radius of 5  $\mu\text{m}$ .

The pore network in sample C6 (figure 40c) represents a total porosity of 7.2 vol%. A percolating porosity of 5.67 vol% is obtained. As with samples C1 and C3, the majority of pores have a triangular shape: from the 47398 pore bodies in total, 47345 are triangular. The average pore body radius is 6.538  $\mu\text{m}$  but pores of maximum 72.44  $\mu\text{m}$  are present as well. The MICP test produces stepwise curves. However, they could continue calculating up to a mercury saturation of 0.92. The most important intrusion phase takes place at pressures higher than 1.35 bar. At this point pores smaller than 7.5  $\mu\text{m}$  start to fill with mercury. The pore throats are generally smaller than the pore bodies and have an average radius of 4.11  $\mu\text{m}$ . In C7 a pore network is visualised which fills 10.41 % of the entire rock volume (figure 40d). 9.26 vol% is represented by percolating porosity. Also in this model triangular pore bodies are represented for the majority of the pores. The average pore radius is 11.81  $\mu\text{m}$ , while maxima of 68.98  $\mu\text{m}$  are obtained. The MICP test shows significant intrusion of the rock starting from a 0.66 bar. From then on, pores smaller than 12  $\mu\text{m}$  are intruded.

### **3.4.2 CO<sub>2</sub> flow simulations**

For the flow simulations, in which the pore network, filled with water, undergoes a primary drainage with liquid CO<sub>2</sub>, followed by a waterflooding and a secondary drainage of CO<sub>2</sub>, the density of the liquid CO<sub>2</sub> is set at 900 kg/m<sup>3</sup>. These simulations were carried out on two samples: C6 and C7. In figure 41, the end state distribution of the pore network is given of C6 after the primary drainage (a), subsequent waterflooding (b) and the secondary drainage (c). After the primary drainage, 39 % of the total porosity remains filled with water. This means the liquid CO<sub>2</sub> entered 61 % of all pores. The data suggest that the liquid CO<sub>2</sub> did not enter the pores in one smooth flow. With increasing pressure, several jumps in CO<sub>2</sub> saturation could be observed. This is an indication that either the resolution of the scans is too low, or that the thresholded porosity lacks effective connections between the pores. In this phase of the simulations, a permeability of 0.43 mD is obtained. After the waterflooding, one can see in figure 41b that some of the liquid CO<sub>2</sub> has been trapped in the pores. However, some CO<sub>2</sub> has been replaced by water. The residual CO<sub>2</sub> saturation now is 50 %. A secondary drainage results in a similar end state as the primary drainage: 39 % of the entire porosity is filled with water, leaving 61 % of the pores filled with CO<sub>2</sub>. Absolute permeability measurements on gengar gave a total permeability of 8.2 mD. This result however is too high for this specific sample. Therefore, not only the results of the absolute permeability must be treated with great caution but also those obtained from the flow simulations, even though the permeability obtained from these simulations (0.43 mD) are closer to the range of permeabilities as known in the Wilhelmøya Subgroup in Dh4.

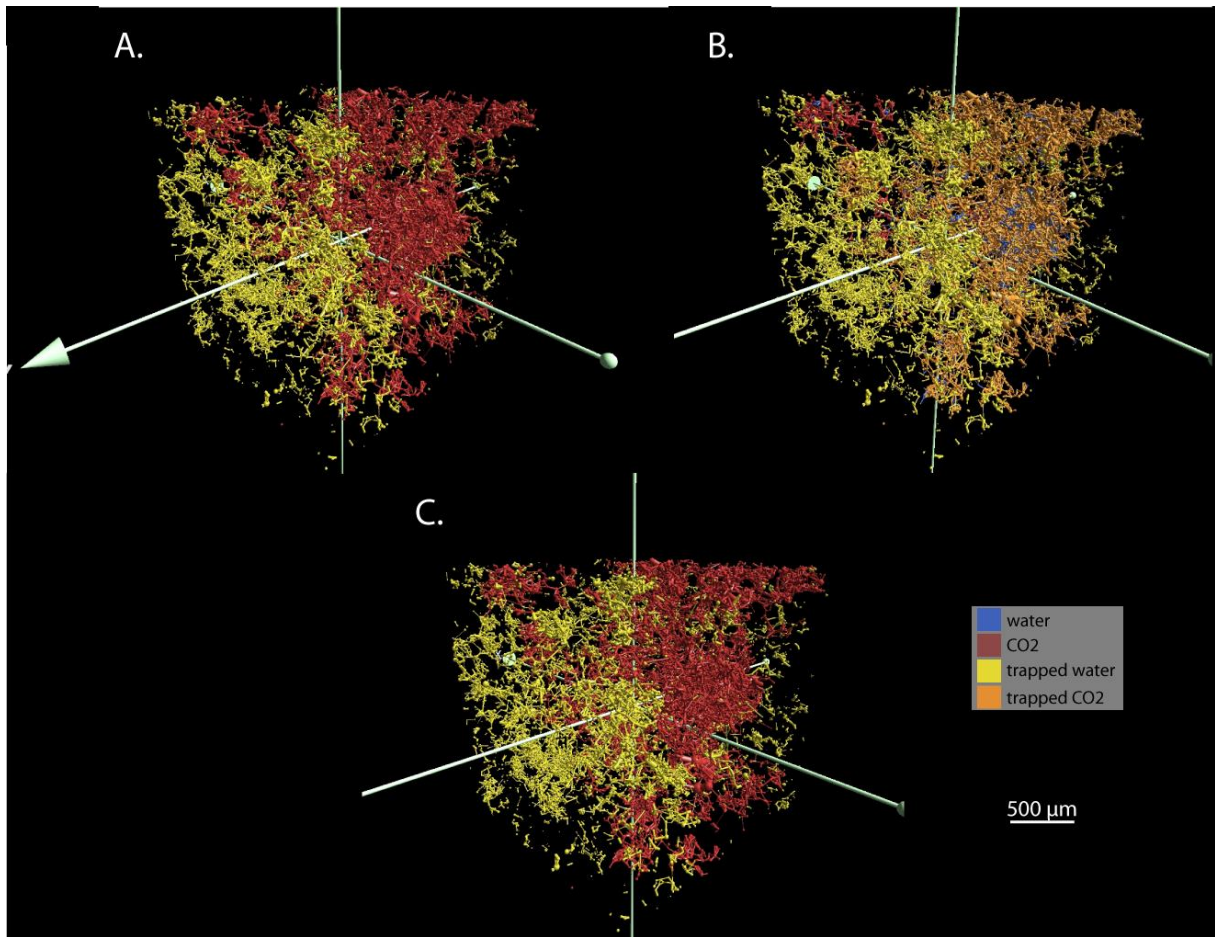


**Figure 41:** End state of the flow simulations in C6 after: primary drainage with CO<sub>2</sub> (a), waterflooding (b) and secondary drainage (c). Pores shown in blue are filled with water, red pores are filled with CO<sub>2</sub> in yellow pores water is trapped and in orange pores CO<sub>2</sub> is trapped.

The flow simulated in C7 is illustrated in figure 42: figure 42a gives the end state after a primary drainage, figure 42b the end state after waterflooding and 42c gives the end state distribution of phases after a secondary drainage. The primary drainage resulted in an uptake of CO<sub>2</sub> in 87 % of all the pores. This uptake was carried out at a calculated permeability of 11 mD. The CO<sub>2</sub> started to enter the pores at a pressure of 0.07 bar and already at the low pressure of 0.1 bar the CO<sub>2</sub> occupied 60 % of the pores in the rock volume. After waterflooding still 59 % of all pores were filled with liquid CO<sub>2</sub>. A secondary drainage brought that level back up to 87 %. However, these results have to be handled with care, since the permeability of this sample was calculated at PanTerra Geoconsultants B.V. at only 0.77 mD. The value of 11 mD is high above this calculated one and too high for all permeabilities measured in the Wilhelmøya Subgroup in Dh4. Also the absolute permeability as calculated on gengar was high above the expected value from laboratory tests.

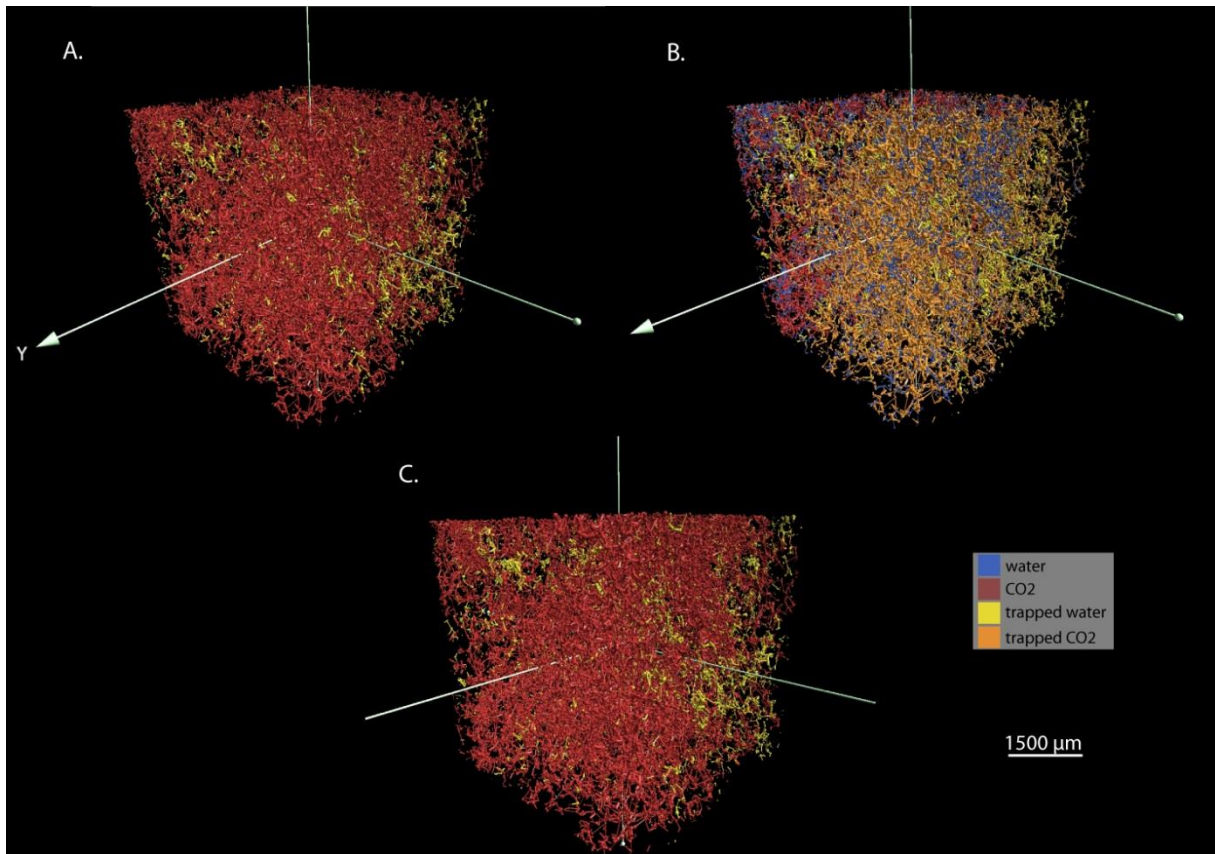


**Figure 42:** End state of the flow simulations in C7 after: primary drainage with CO<sub>2</sub> (a), waterflooding (b) and secondary drainage (c). Pores shown in blue are filled with water, red pores are filled with CO<sub>2</sub> in yellow pores water is trapped and in orange pores CO<sub>2</sub> is trapped.





## **4. Discussion**

In this discussion special attention is given to the porosity and fractures within the samples. Both are important features in the field samples and in the core samples from Dh2 and Dh4. In the discussion concerning the porosity, individual samples are linked to each other according to their overall facies and porosity distribution.

Prior to the analysis of the results, some thoughts or constrictions have to be made clear with respect to their interpretation. The samples which were analysed are taken from three approximately 20 m thick rock successions. The total combined thickness of the samples from Dh4 is 54 cm, those from Dh2 add up to 21 cm and in the field a similar combined thickness is obtained from the samples. This means that the analysis of the samples cannot be considered representative for the entire Wilhelmøya Subgroup, let alone the Kapp Toscana Group. This is the case for both the porosity distribution as the fracture analysis which will follow. Furthermore, the samples were prepared and drilled in a cylinder with maximum diameter of 4.7 cm. The results which are obtained from any analysis on this level are merely indicative and should thus not be extrapolated to the entire reservoir section below Longyearbyen. Also the rocks were preferentially sampled from sandstone rich layers in the successions. However, this does not mean that all sandstone layers in the succession now are characterized with CT data. The results must be interpreted as characteristic for the samples, not for entire metre-thick sandstone strata. Another constriction which must be kept in mind has to do with the resolution of the scans. The field samples were first scanned with a resolution of 41  $\mu\text{m}$ , those from Dh4 obtained a resolution of 56.61  $\mu\text{m}$  and samples in Dh2 were first characterized by scans with a resolution of 62.56  $\mu\text{m}$ . Not all samples were subsequently scanned with a higher resolution. Those which were scanned at higher resolutions were characterized by resolutions ranging from 3.99  $\mu\text{m}$ , over 2.8  $\mu\text{m}$  to 1.68  $\mu\text{m}$ .

### **4.1 Porosity distribution**

In the discussion of the porosity distribution, the results of the different samples will be compared to each other according to their position in the correlated lithologs (figure 12). The overview will be given from the deep parts within the cores upwards: first section 1 from figure 12 will be discussed, followed by the other sections, up to section 7. Sections 3, 4 and 5 will be discussed together. In these sections only four samples were scanned. C5, the sample with the highest calculated open porosity within Dh4 was not scanned at a resolution of 56.61  $\mu\text{m}$ , after which samples were chosen for subsampling. In this selection, samples were preferred from which scans were already made in order to characterize them at a higher resolution. Therefore C5 is not characterized by CT-scans. Also sections 6 and 7 will be discussed together. In the correlation these can be treated as two separate sections, because the extent of the conglomerate in section 6 is much higher than conglomerate units in section 7. But for this discussion, sample C7 represents a conglomerate sample which is representative for the conglomerate units in both section 6 and section 7. The porosity which was thresholded in scans of different resolutions will be compared to the results of laboratory tests in which the open porosity was calculated. The thresholded porosity contains both the pore space and the fractures found at a given resolution within the samples. However, when no porosity could be thresholded besides from the porosity due to fractures, this was not calculated for this part of the discussion.

### **4.1.1 Section 1**

Section 1 is represented by sample T1 in the field, samples C1, C2 and C3 in Dh4 and sample D3 in Dh2. Table 7 gives a summary of the obtained results in these samples. It includes the open porosity as calculated in laboratory tests and the total porosity thresholded from scans at different resolutions.

**Table 7:** Overview of the obtained results in section 1, concerning the porosity distribution.

	<b>T1</b>	<b>C1</b>	<b>C2</b>	<b>C3</b>	<b>D3</b>
Laboratory porosity (vol%)	9.68	12.58	10.71	3.92	4.71
Porosity > 56.61 $\mu\text{m}$ (vol%)	N.A.	5.76	1.93	/	2.06
Porosity > 41.00 $\mu\text{m}$ (vol%)	/	N.A.	N.A.	N.A.	N.A.
Porosity > 3.99 $\mu\text{m}$ (vol%)	2.56	4.48	N.A.	2.9	2.25
Porosity > 2.8 $\mu\text{m}$ (vol%)	N.A.	N.A.	N.A.	N.A.	2.45

In table 7, 'not applicable' (N.A.) infers that the sample was not scanned at a given resolution. The symbol '/' means that the sample was scanned at the given resolution, but did not show any porosity that could be thresholded, other than possible fracture porosity. It is clear that for all five samples the thresholded porosity does not provide for the total porosity of the sample as calculated in the laboratory tests. For T1 for example, at a resolution of 3.99  $\mu\text{m}$  a porosity of only 2.56 vol% is obtained. This is 7.12 vol% less than the open porosity calculated from laboratory tests. Also in C1, both the porosity at a resolution of 56.61  $\mu\text{m}$  and 4  $\mu\text{m}$  are much lower than the calculated open porosity. The porosity larger than 3.99  $\mu\text{m}$  is larger than that larger than 56.61  $\mu\text{m}$  in C1. This result is odd, since the porosity larger than 3.99  $\mu\text{m}$  should incorporate that larger than 56.61  $\mu\text{m}$ . In the subsample, the pores larger than 56.61  $\mu\text{m}$  are apparently less represented. Analysis in E-core resulted in a further characterization of the pore network in C1. It was characterized by an average pore diameter of 11.3  $\mu\text{m}$ . Although some pores were up to 71.59  $\mu\text{m}$  wide, the majority of the pores were restricted to an upper value of 20  $\mu\text{m}$ . In C2 a porosity of 1.93 vol% was obtained at low resolution, however the sample was not scanned at a resolution higher than 56.61  $\mu\text{m}$ , leaving the pores smaller than this resolution undetected. C3 was characterized with an open porosity calculated in the laboratory at 3.92 vol%. The scan with a resolution of 3.99  $\mu\text{m}$  revealed pores as well as fractures. Together these gave a total porosity of 2.9 vol%. From this, 0.05 vol% accounts for the fractures. Although there still is a total difference of 1 vol%, this is a smaller difference than obtained in the other samples. D3, the sample which is represented by two lithologies had an overall porosity of 2.06 vol% in the scan with the lowest resolution. This increased slightly with increasing resolution, both for the upper part of the sample (2.25 vol%) and for the lower part (2.45 vol%). However, the laboratory results still are not matched by the CT-results.

Facies like, T1 shows to be the most similar with C3. Both have a sandstone matrix, in which clay is dispersed in either layers or as patches within the sample, and both are bioturbated, resulting in the presence of ichnofossils. The *Thalassinoides* burrows in T1 consist of T-formed tubes, just as the tubes which are present in C3 (and C4) and are in T1 part of the burrowing system of *Upogebia affinis*

and in C3 identified as Thalassinoides. Both ichnofossils can be brought back to decapod crustaceans (Williams, 1984). Also the porosity which could be thresholded at a resolution of 3.99  $\mu\text{m}$  is similar for both samples.

#### **4.1.2 Section 2**

Section 2 is represented by four samples in total. These are T3, T2 and T4 from the field and C4, from Dh4. Their properties are listed in table 8, using the same methodology as in table 7.

**Table 8:** Representation of the porosity distribution in samples within section 2. The Wilhelmøya Subgroup is represented in the field as well as in Dh4.

	<b>T3</b>	<b>T2</b>	<b>T4</b>	<b>C4</b>
Laboratory porosity (vol%)	9.03	5.13	7.00	1.81
Porosity > 56.61 $\mu\text{m}$ (vol%)	N.A.	N.A.	N.A.	0.05
Porosity > 41.00 $\mu\text{m}$ (vol%)	/	/	/	N.A.
Porosity > 3.99 $\mu\text{m}$ (vol%)	0.9	/	N.A.	N.A.
Porosity > 2.8 $\mu\text{m}$ (vol%)	N.A.	N.A.	N.A.	0.59

The results listed in table 8 clearly indicate that none of the four samples shows a porosity in the scans characterized by the lowest resolution (41  $\mu\text{m}$  for T3, T2 and T4 and 56.61  $\mu\text{m}$  for C4). Even when the resolution is increased up to 4  $\mu\text{m}$ , T2 fails to indicate porosity. The porosity which is given in C4 is 100% due to fractures in the sample. At a resolution of 2.8  $\mu\text{m}$ , the fractures give the sample a total porosity of 0.59 vol% Compared to the open porosity value from laboratory tests, this is a significant value. However, at lower resolution, fractures account for less porosity. The only indication of pores is given in sample T3 where at a resolution of 4  $\mu\text{m}$  a porosity of 0.9 vol% could be thresholded. Since there are no fractures in this subsample of T3, the thresholded porosity is entirely due to pore space between the grains. Clearly, for what concerns the distribution of porosity, or the lack of it, one can correlate the samples from the field with C4, from Dh4. However, concerning the facies of the rocks, C4 has more affinity to C3 and therefore T1, found in the first section of the correlation. The resolution at which certain features are observed thus definitely has to be kept in mind.

#### **4.1.3 Sections 3, 4 & 5**

Sections 3, 4 are represented by 4 samples which have been scanned: S2, S3, C6 and D2. Their porosity distribution according to the resolution of the scans is listed in table 9. Sample S2 and S3 represents section 3 and 5 respectively in the field, Dh4 is represented by C6 section 5 and the top of section 4 is represented by D2 in Dh2.

**Table 9:** Overview of the porosity distribution for samples S2, S3, C6 and D2 representing section 3 to 5 in the field, Dh4 and Dh2.

	<b>S2</b>	<b>S3</b>	<b>C6</b>	<b>D2</b>
Laboratory porosity (vol%)	7.85	5.96	7.54	1.05
Porosity > 56.61 $\mu\text{m}$ (vol%)	N.A.	N.A.	/	0.2
Porosity > 41.00 $\mu\text{m}$ (vol%)	N.A.	/	N.A.	N.A.
Porosity > 3.99 $\mu\text{m}$ (vol%)	0.68	N.A.	N.A.	N.A.
Porosity > 2.8 $\mu\text{m}$ (vol%)	N.A.	N.A.	6.86	N.A.
Porosity > 1.68 $\mu\text{m}$ (vol%)	N.A.	N.A.	N.A.	0.83

Sample S2 is only scanned at a resolution of 3.99  $\mu\text{m}$  revealing a porosity of 0.68 vol%, as where the laboratory test calculated an open porosity of 7.85. No fractures were distinguishable in the scan. So either the sample of S2 was taken at a location in the rock with a depleted porosity, or important fractures were missed by sampling. Of course a combination of both is possible as well. S3, which is only scanned at a resolution of 41.00  $\mu\text{m}$  did not show any porosity asides from the fractures within the rock. A similar result is obtained in the low resolution scan of C6. The sample does not show porosity at the resolution of 56.61  $\mu\text{m}$ . However, from this sample a subsample was taken and scanned with a resolution of 2.8  $\mu\text{m}$ . This scan revealed a porosity good for 6.86 % of the entire subsample. This is not as much as the open porosity calculated from laboratory tests. The last sample representing these sections is D2. This is found right beneath the boundary between section 4 and section 5 in Dh2 (figure12). The sample is characterized by the presence of predominantly vertical fractures filled with secondary mineralisations. However, in some of these fractures pore space can be observed. Thresholding of this porosity in the veins resulted in a porosity of 0.2 vol% at a resolution of 56.61  $\mu\text{m}$ . Subsequently a subsample was taken and scanned with a resolution of 1.68  $\mu\text{m}$ . Since it was taken at a location in which no veins are found, the subsample characterizes the matrix in which the veins were found. A porosity of 0.83 vol% was obtained. Since it is known that the fractures occupy 10.53 % of the entire volume and thus the matrix represents 89.47 % of the volume, the total pore space which is visualized in both scans can be calculated. This calculation has a resulting total porosity of 0.94 vol%. It is clear that even the combined porosity of scans with different resolutions cannot account for the calculated open porosity from laboratory tests.

Although sample C6 has a more heterogeneous look, the facies of S3 and C6 are comparable in the low-resolution scans. Both are characterized by a distribution of clays within the sample. In S3 this happens in a homogeneous way, while in sample C6 a more heterogeneous distribution is present. Also their porosity distribution can be linked: the open porosity, calculated in the laboratory, is similar, and both samples lack porosity in the scans at a low resolution. However, it is not known if a subsample from S3 would have shown a porosity at higher resolution as C6 did.

#### **4.1.4 Section 6 & 7**

Section 6 and 7 are represented by samples S6, S7, S8 and T5 in the field; C7, C8 and C9 in Dh4 and D1 in Dh2. The results are listed in tables 10a (field samples) and 10b (core samples).

**Table 10a:** Overview of the porosity distribution in samples S6, S7, S8 and T5.

	<b>S6</b>	<b>S7</b>	<b>S8</b>	<b>T5</b>
Laboratory porosity (vol%)	16.76	4.47	12.09	5.78
Porosity > 41.00 $\mu\text{m}$ (vol%)	10.85	0.94	/	/
Porosity > 3.99 $\mu\text{m}$ (vol%)	N.A.	3.68	N.A.	N.A.

**Table 10b:** Overview of the porosity distribution in samples C7, C8, C9 and D1, representing section 6 and section 7 in Dh4 and Dh2.

	<b>C7</b>	<b>C8</b>	<b>C9</b>	<b>D1</b>
Laboratory porosity (vol%)	12.96	7.09	1.24	1.83
Porosity > 56.61 $\mu\text{m}$ (vol%)	3.07	0.02	/	/
Porosity > 3.99 $\mu\text{m}$ (vol%)	10.11	N.A.	N.A.	0.96

Table 10a shows that for both conglomerate samples S6 and S7, the porosity which can be thresholded in the scans remains lower than the open porosity calculated in laboratory tests. Sample S6, scanned at a resolution of 41  $\mu\text{m}$  is characterized by a thresholded porosity of 10.85 vol%. This is 5.91 vol% lower than the open porosity of the sample. However, no scans were taken with a resolution higher than 41  $\mu\text{m}$ , leaving the pores smaller than this resolution undetected. Sample S7 is characterized by a thresholded porosity of 0.94 vol% in the scans with a low resolution. A subsample scanned at a higher resolution revealed a porosity of 3.68 vol% which is still 0.79 vol% under the calculated open porosity of the sample. In both S8 and T5 no porosity was shown in the scans and no subsamples were subsequently scanned. In these samples, pores smaller than 41  $\mu\text{m}$  remained undetected.

In table 10b the results for the core samples are displayed. Sample C7, which shows affinity with the field conglomerates S6 and S7, was scanned at both a resolution of 56.61  $\mu\text{m}$  and 3.99  $\mu\text{m}$ . In both scans porosity was revealed. The porosity greater than 3.99  $\mu\text{m}$  was determined to be 10.11 vol%. This result is close to the open porosity calculated at 12.96 vol%. In comparison to the results of the field samples, C7 would plot in between S6 and S7. In sample C8, fractures are responsible for a porosity of 0.02 vol% in scans with a resolution of 56.61  $\mu\text{m}$ . Samples C9 and D1 have also been scanned at a resolution of 56.61  $\mu\text{m}$ , but failed to show porosity. However, a subsample taken from D1 showed a porosity of 0.96 vol% at a resolution of 3.99  $\mu\text{m}$ . From both the laboratory porosity characterization and the facies as seen in the scans, one can link C9 with D1.

## **4.2 Fracture analysis**

Before the fractures can be discussed concerning their maximum aperture and circumscribed diameters, certain observations are important to note. One of those observations is the difference which can be seen in the fracture distribution in the field and in the core samples. In all 9 samples from the field which were scanned at a resolution of 41  $\mu\text{m}$  fractures were observed. In the scans with the lowest resolution taken from the core samples, 4 from the 11 samples which were scanned showed the occurrence of fractures and in D2 veins with mineral infill were observed. To these samples, D1 and C6 can be added, which showed fractures at the resolution of 3.99  $\mu\text{m}$  and 2.8  $\mu\text{m}$  respectively. This brings the total of core samples characterized by observed fractures to 6 plus D2, characterized by vertical veins. One can thus agree that the frequency in which fractures occur in the field samples is higher than that of fractures in the core samples. In both the field samples and the core samples however, the fractures are most often related to a competence contrast between different layers. This can be seen from the fact that the fractures often follow borders between sandstone lithologies and clay-layers. This is an observation which is also made in Ogata et al. (2012). Another observation from these authors is that most of the fractures observed in the Wilhelmøya subgroup as characterized in Dh4 are found to have a connection between the orientation of the fractures and the lithology in which they occur. Low-angle ( $0^\circ - 45^\circ$ ), non-mineralized fractures predominate in fine-grained lithologies such as shales and siltstones as where high-angle ( $> 45^\circ$ ) fractures and veins preferably occur in coarse-grained units as sandstones (Ogata et al., 2012). For this thesis, samples with a sandstone-dominated lithology were preferentially sampled. However, the fractures within the samples from Dh4 are mainly characterized by a preferred horizontal orientation. In 3 from the 5 fractured samples from Dh4 there is an important incorporation of clays (C3, C4 and C6). Although not on macroscopic level, one can also see in scanned images that the fractures in C1 are also bound to clay infillings of the rock. In C8 however, this is not visible.

One of the conclusions of Ogata et al. (2012) was that the fractures, as observed in the drill cores and in the outcrops, were relevant for fluid circulation. Borehole water injection tests and results from wireline logs were cited to support this. Because the storage potential of the targeted aquifer for  $\text{CO}_2$  injection is considered to be mainly depending on the interconnectivity, length and aperture of the fracture system (Ogata et al., 2012), the fractures were analysed for these parameters. No data is provided here for the characterization of the interconnectivity between samples, but the length of the fractures was approached via characterizing the diameter of the circumscribed sphere for the individual fractures. In order to have an idea of the fracture apertures, the fractures were divided in different objects and from each object the maximum opening was calculated. This calculation starts with the virtual emplacement of one testing voxel in the centre of the object. While this voxel is kept in place, other voxels are placed beside it in order to form a cube with the original voxel as centre. This is done with an increasing amount of voxels until the testing cube reaches the sides of the object. As a result of this type of virtual measurement, the maximum opening of an object will always be defined with an uneven number of voxels. In what follows, the maximum opening of all observed fractures will be discussed, in order to further compare the field samples with those from the cores. Subsequently, an overview will be given from the circumscribed diameters calculated in the core samples characterized by fractures.

### 4.2.1 Maximum openings

The maximum opening of fractures was calculated for both the field samples and those from the cores. If the fractures could be extracted with the MSHFF script by Voorn et al. (2013), their maximum opening was calculated in Morpho+. Otherwise the fracture apertures were manually measured in a plane perpendicular to the fractures. This however only gives an indication of the maximum opening. In table 11a the maximum fracture apertures for the field samples are listed. These were calculated from scans with a resolution of 41  $\mu\text{m}$ . Table 11b gives the distribution of maximum fracture openings as found in the core samples. The samples were all, but C8 (N.A.) scanned at different resolutions. They are arranged according to their location in the field litholog.

**Table 11a:** Overview of the maximum openings from fractures as calculated in Morpho+, or manually measured in cross-sections of the field samples.

	T1	T3	T2	T4	S3	S6	S7	S8	T5
Morpho+ calculated ( $\mu\text{m}$ )	123 - 205	123 - 369	123 - 205	123 - 205	41 - 533	/	/	/	123 - 533
Manual measurement ( $\mu\text{m}$ )	/	/	/	/	/	82 - 123	205	123	/

**Table 11b:** Overview of the maximum fracture openings as calculated in Morpho+, or manually measured in cross-sections of samples from Dh4 and Dh2. Measurements were carried out at different resolutions.

	C1	C3	C4	C6	C8	D1
Morpho+ calculated ( $\mu\text{m}$ )	/	169.83 16 - 20	283.05 8.4 – 25.2	/	169.83 N.A.	/
Manual measurement ( $\mu\text{m}$ )	226.4 8 - 20	/	/	/	/	/
				8.4 - 14		8 – 23.9

From table 11a one can determine that the field samples are mostly characterized by fractures with maximum apertures of 123  $\mu\text{m}$  to 205  $\mu\text{m}$ . The occasional outlier with a fracture aperture of up to 533  $\mu\text{m}$  is rather an exception if one refers to the frequency of occurrence. Also in the samples where the fractures could not be thresholded with the MSHFF script, manual measurements obtained apertures of 82  $\mu\text{m}$  to 205  $\mu\text{m}$ , which is in line with the calculated apertures by Morpho+. Table 11b in which results from scans with different resolutions are given shows that the fractures which are found in C1, C3, C4 and C8 at a resolution of 56.61  $\mu\text{m}$  show similar apertures as the fractures in the field samples. Their fracture openings range from 169.83  $\mu\text{m}$  to 283.05  $\mu\text{m}$ . In three samples scanned at a resolution of 3.99  $\mu\text{m}$  and two which were scanned with a resolution of 2.8  $\mu\text{m}$  micro-fractures could be distinguished. In C3 and C4 the fractures could be segmented which resulted in maximum openings of 8.4  $\mu\text{m}$  to 25.2  $\mu\text{m}$ . Manual measurements of the fractures in C1, C6 and D1 show similar apertures. The micro-fractures within these samples can thus be characterized with maximum apertures of 8  $\mu\text{m}$  to 25.2  $\mu\text{m}$ .



### **4.2.2 Diameter of circumscribed sphere**

To give a characterization of the length to which fractures affect the rocks in the given samples, the circumscribed diameter of a sphere by which the entire fracture is surrounded is given. For this analysis it is important to note that the fractures as found in the core samples do not penetrate the rocks in the same way as they do in the field samples. The fractures in the core samples are more subtly distributed in the rock. They do not form large cracks which can be followed from one side of the sample to the other as the fractures in the field samples do. In the field samples the fractures were subjected to physical weathering which has caused the fractures to propagate deeper in the rocks. Therefore this analysis was only carried out for core samples. More specifically samples C3, C4 and C8 were analysed for this parameter because in these samples, it was possible to visualise the fractures as individual objects. In table 12 the results of this analysis is joined in one table. In this table 'CD' stands for circumscribed diameter and a distinction is made between macro-fracture analysis, obtained from scans with a resolution of 56.61  $\mu\text{m}$  and micro-fracture analysis from scans with a higher resolution (3.99  $\mu\text{m}$  and 2.8  $\mu\text{m}$ ).

**Table 12:** Overview of the results concerning the circumscribed diameter of fractures in samples C3, C4 and C8. 'CD' stands for circumscribed diameter and '\*' means that the value represents a minimum circumscribed diameter since this fracture as such was not completely found within the analysed section of the sample.

		<b>C3</b>	<b>C4</b>	<b>C8</b>
<b>Macro-fractures</b>	Maximum CD ( $\mu\text{m}$ )	143	21681	17379
	Average CD ( $\mu\text{m}$ )	/	3580	4802
<b>Micro-fractures</b>	Maximum CD ( $\mu\text{m}$ )	2266	2662 (*)	/
	Average CD ( $\mu\text{m}$ )	229	175	/

In table 12 one can read that from the fractures which were analysed in C3, the micro-fractures propagate further in the sample than the macro-fractures. Not only the maximum CD is greater in the micro-fractures, but the average CD is greater than the upper and only value of circumscribed diameter obtained in C3. Macro-fractures in C4 however can affect up to 2.17 cm of the sample. In this sample also the average CD calculated from the macro-fractures is greater than the maximum CD of the micro-fractures. However, one must take into account that the maximum CD of micro-fractures in C4 is only a minimum length. This is because the fracture of subject probably propagates further in the section of the rock which was not analysed. But, since the micro-fracture with the second large CD in C4 is characterized by a CD of 893  $\mu\text{m}$  it is safe to conclude that in C4 the macro-fractures are found to be the main propagators in length. In C8, only scanned at the lowest resolution, the fractures affect the rocks for larger lengths than in C4. Here the average CD is 4.8 mm, although the maximum CD in C8 is smaller than that in C4.

## **5. Conclusion**

In order to further characterize the rocks from the Wilhelmøya Subgroup, samples, taken at three different locations, were analysed with the X-ray computed tomography scanners developed at the UGCT. It concerns a total of 9 field samples and 11 core samples, spread over the cores of Dh4 and Dh2, two drilling locations developed by the UNIS CO<sub>2</sub> Lab. The rocks of the Wilhelmøya Subgroup are of particular interest to the UNIS CO<sub>2</sub> Lab since the Subgroup has been identified as the section which is most suitable for CCS in the direct neighbourhood of Longyearbyen, Svalbard (Mørk, 2010). Previous studies have shown that the highest porosities and permeabilities are found within rocks from the Knorringfjellet Formation, Wilhelmøya Subgroup. Therefore these rocks were targeted for further characterization with a multi-scale approach. Specifically sandstone units and sand-supported conglomerate units were sampled. Shales and siltstone intervals were avoided as much as possible. For the CT characterizations of the rock samples one must take into account that the samples only represent a total thickness of approximately 50 cm of the Wilhelmøya Subgroup in the field, 54 cm of the Subgroup in Dh4 and 21 cm in Dh2. In all three locations the total thickness of the Subgroup extends to approximately 20 m. Therefore, the results obtained from these analyses should be interpreted with care. The samples do not represent the Wilhelmøya Subgroup in its totality and the results are merely characterizing those parts of it which were sampled.

### **5.1 Pore-scale characterization**

The field samples were analysed in scans with the resolution of 41 µm after which five of them were subsampled and scanned at a resolution of 3.99 µm. In the lower resolution scans, the rock samples were characterized for their general facies distribution as well as for their fossil content. At this resolution, the porosity of the samples could be extracted in only two samples, both from the conglomerate section of the Brentskardhaugen Bed. What could be extracted however did not correspond to the calculated open porosities from laboratory tests. Fractures were observed in all field samples which were scanned. It is clear that these fractures, which form the main pore space in the rocks at this resolution, are strongly enhanced by physical weathering due to their susceptibility to frost and thaw in the field. This mainly influenced the length at which they affect the rocks in which they are found. The apertures of the fractures correspond to the apertures of fractures as seen in the core samples. Subsamples were subsequently taken in regions within the rocks which were not affected by fractures. Scans from these subsamples with a resolution of 3.99 µm made it possible to observe pore space in 4 of the 5 scanned samples. However, as in the scans at lower resolution, the thresholded porosity could not account for the open porosity, calculated from laboratory tests.

8 core samples were taken from Dh4 and primarily scanned at a resolution of 56.61 µm. In Dh2, the low resolution scans were determined at a level of 62.56 µm. For both cores the samples were characterized and visualised according to their facies distribution and fossil-content. This led to the determination of regions in the samples which were interesting for subsampling so the best chances for the extraction of a porosity were obtained. However, also at the lower resolution of the first scans, pores could be extracted from 3 of the samples in Dh4 and 2 of the samples in Dh2. The extracted porosity however did not account for the open porosity calculations from laboratory tests. Also pore networks extracted in scans from subsamples, at resolutions ranging from 1.68 µm to 3.99 µm failed to represent the total amount of porosity. The open fractures which were observed in 6 of the 11 scanned core samples could be divided in two distinct groups: macro-fractures, visible in the

scans at low resolution, and micro-fractures, observed in the scans carried out with the highest resolutions. The apertures as found for the macro-fractures are comparable to the apertures found in fractures in the field samples. However, for 3 of the 6 samples in which fractures were identified, circumscribed spheres were calculated in order to give an idea of the fracture length. Where the fractures in the field samples are often found to propagate along the entire diameter of the cylindrical sample (4.1 cm), maximum circumscribed diameters were found for the fractures in the core samples of 143  $\mu\text{m}$  to 21681  $\mu\text{m}$ . The average circumscribed diameters in samples C4 and C8 are calculated at 3.58 mm and 4.802 mm respectively. Micro-fractures observed in the core samples were calculated to have maximum apertures of 8  $\mu\text{m}$  to 25.2  $\mu\text{m}$ . For the two samples in which these were abundantly present and the Voorn et al. (2013) script could segment them, diameters of circumscribed spheres were calculated. The fractures were characterized by a maximum propagation in the samples of 2.266 mm in C3 and 2.662 mm in C4. The average micro-fractures are found to have a circumscribed diameter of 229  $\mu\text{m}$  in C3 and 175  $\mu\text{m}$  in C4. One can thus conclude that the fractures as observed in the core samples are rather subtle features in these samples, whether they can be characterized as macro- or micro-fractures. Their maximum opening is similar to that of fractures in the field samples, but their propagation length is significantly smaller. To relate these results to possible  $\text{CO}_2$  flow in the samples, a suitable approach for determining the interconnectivity between the fractures should be applied next. However since the segmentation algorithm for fractures in Morpho+ already labels the fractures as one object when they are connected, their connectivity could disappoint in these specific samples. The observations are moreover also limited due to the limits of the bore holes. The diameter of the core rocks is 4.1 cm for Dh2 and 4.7 cm for Dh4. Although specific attention was given as where to drill, the rocks of the Wilhelmøya Subgroup are known to be prone to lateral variations. This also could have its implications on the observed features in the samples. The results must thus not be generalised.

Concerning the MSHFF script by Voorn et al. (2013): it has proven to be a useful tool for the segmentation of well-pronounced fractures, specifically when they are found in a rather homogeneous matrix, as was the case with most of the field samples. However when the script is used for the segmentation of rather subtle fractures in a more heterogeneous matrix, it is much more difficult to find the right input parameters for the calculations. Therefore the calculation time increases significantly and for this research, the script failed to segment the fractures in in three core samples. Overall the script uses a very computer intensive algorithm, restricting the workable volume in which fractures can be segmented.

## **5.2 Rock modelling**

The rock modelling in E-core was carried out on 4 samples: C1, C3, C6 and C7. Two of which were only characterized by the making of a simplified pore network by a ball-and-stick model (C1 and C3). This resulted in the definition of the average pore radius within the pore network. For C1 this was determined at 11.3  $\mu\text{m}$  and for C3 a value of 8.5  $\mu\text{m}$  was obtained. These values were confirmed by simulated MICP measurements carried out on the simplified pore network. For samples C6 and C7 a similar pore network was constructed. The pores were described with average radii of 6.538  $\mu\text{m}$  and 11.81  $\mu\text{m}$  respectively. Because the pores were characterized with a better connection between them, these samples were subsequently used for flow simulations, both on the simplified network via drainage simulations and on the actual segmented pore network in a supercomputer environment. Doing so, permeability measurements were simulated. For both samples, the absolute

permeability simulations gave values which were too high according to actual measurements. This indicates that the interconnectivity of the pores was not sufficiently visible in the scans. Most likely, an increase in resolution of the scans would result in a better simulation for the absolute permeability. Also the simulations carried out on the simplified network, resulted in permeabilities which were above the real permeabilities known from laboratory tests. This is yet another indication that the resolution still was not high enough for a detailed flow simulation to be carried out.

### **5.3 Further research**

There are several ways in which this research could be continued. Since Ogata et al. (2012) have shown that the fractures which are characterized by a horizontal orientation are mainly found in the shales and siltstone sections of the Wilhelmøya Subgroup, one could shift the focus of fracture analysis to samples from these sections in order to examine if they are characterized by more significant fractures or not. A more detailed study in which the samples are analysed at greater resolution and fluid flow models are made from both samples with significant fractures and without in order to compare the results of these simulations, is another option. Or one could shift the focus of the study to rock samples from other possible fractured reservoir sections, for example in the De Geerdalen Formation, in order to characterize the fractures at different depths in the cores.

Generally, CT has shown to be a unique tool in order to characterize these rock samples at a micrometre scale, so that for the first time, an indication could be given of the fracture aperture and propagating length within samples of the Wilhelmøya Subgroup.



## 6. References

- Attix, F.H. (1986). *Introduction to radiological physics and radiation dosimetry*. New York: Wiley.
- Bäckström, S.A. & Nagy, J. (1985). Depositional history and fauna of a Jurassic phosphorite conglomerate (the Brentskardhaugen Bed) in Spitsbergen. *Norsk Polarinstitutt Skrifter*. 183. 1-61.
- Bakke, S. & Øren, P.E. (1997). 3-D Pore-Scale Modelling of Sandstones and Flow Simulations in the Pore Networks. *SPE Journal*. 2, 136-149.
- Bergan, M. & Knarud, R. (1993). Apparent changes in clastic mineralogy of the Triassic-Jurassic succession, Norwegian Barents Sea: Possible implications for palaeodrainage and subsidence. In: Vorren, T.O., Bergsager, E., Dahl-Stamnes, Ø.-A., Holter, E., Johansen, B., Lie, E. & Lund, T.B. (eds) *Arctic geology and petroleum potential*. Amsterdam, Elsevier: Norwegian Petroleum Society, Special Publication v. 2. 481-493.
- Bergh, S.G., Braathen, A. & Andresen, A. (1997). Interaction of basement-involved and thin-skinned tectonism in the tertiary fold-thrust belt of central Spitsbergen, Svalbard. *American Association of Petroleum Geologists Bulletin*. 81, 637-661.
- Braathen, A., Baelum, K., Christiansen, H.H., Dahl, T., Eiken, O., Elvebakk, H., Hansen, F., Hanssen, T.H., Hochmann, M., Johansen, T.A., Johnsen, H., Larsen, L., Lie, T., Mertes, J., Mørk, A., Mørk, M.B., Nemeč, W., Olaussen, S., Oye, V., Rød, K., Titlestad, G.O., Tveranger, J. & Vagle, K. (2012). The Longyearbyen CO<sub>2</sub> Lab of Svalbard, Norway – initial assessment of the geological conditions for CO<sub>2</sub> sequestration. *Norwegian Journal of Geology*. 92, 353-376.
- Brabant, L., Vlassenbroeck, J., De Witte, Y., Cnudde, V. et al. (2011). Three-dimensional analysis of high-resolution X-ray computed tomography data with Morpho+. *Microscopy and Microanalysis*. 17 (2), 252-263.
- Bromley, R.G. & Frey, R.W. (1974). Redescription of the trace fossil Gyro-lithes and taxonomic evaluation of Thalassinoides, Ophiomorpha and Spongeliomorpha. *Bulletin of the Geological Society of Denmark*. 23, 311-335.
- Brooks, R.A. & Di Chiro, G. (1976). Principles of computer assisted tomography (CAT) in radiographic and radioisotopic imaging. *Physics in Medicine and Biology*. 21 (5), 689-732.
- Chen, S. & Doolen, G.D. (1998). Lattice Boltzmann Method for Fluid Flows. *Annual review of Fluid Mechanics*. 30, 329-364.
- Cnudde, V. (2011). Integrated reservoir modelling, Partim: Petrophysical rock properties. *University of Ghent course notes*.
- Dypvik, H., Hvoslef, S., Bjaerke, T. & Finnerud, E. (1985). The Wilhelmøya Formation (Upper Triassic-Lower Jurassic) at Bohemanflya, Spitsbergen. *Polar Research*. 3, 155-166.
- Elvebakk, H. (2010). NGU Report 2010.018 Results of borehole logging in well LYB CO<sub>2</sub>, Dh4 of 2009, Longyearbyen, Svalbard. Geological Survey of Norway: 5-35.

European Standard NBN EN 1936:2006. Natural stone test methods – Determination of real density and apparent density and of total and open porosity. CEN, Brussels.

Farokhpoor, R., Torsaeter, O., Baghbanbashi, T., NTNU, Mørk, A., SINTEF, NTNU, Lindeberg, E. & SINTEF (2010). Experimental and Numerical Simulation of CO<sub>2</sub> Injection into Upper-Triassic Sandstones in Svalbard, Norway. *The Society of Petroleum Engineers international conference on CO<sub>2</sub> capture, storage and utilization held in New Orleans, USA*.

Forbes, A.T. (1973). An unusual abbreviated larval life in the estuarine burrowing prawn *Callinassa kraussi* (Crustacea: Decapoda: Thalassinidea). *Marine Biology*. 22, 361-365.

Glover, P. (2001). Formation Evaluation MSc Course Notes. *Aberdeen University*. 84-94.

Gómez, J.J. & Fernández-López, S. (1994). Condensation processes in shallow platforms. *Sedimentary geology*. 92, 147-159.

Greg, M. (2001). X-ray computed tomography. *Physics Education*. 36 (6), 442-451.

Haremo, P., Nagy, J., Elverhøi, A., Eikeland, T.A. & Johansen, H. (1990). Structural development along the Billefjorden Fault Zone in the area between Kjellströmdalen and Adventdalen/Sassendalen, central Spitsbergen. *Polar Research*. 8, 195-216.

Harland, W.B. (1997). The Kapp Toscana and Sassendalen Groups (Liassic, mainly Triassic). In: *The geology of Svalbard*. London: The geological society. 59-63.

Ketcham, R.A. (n.d.). *X-ray computed tomography*. Available: [http://serc.carleton.edu/research\\_education/geochemsheets/techniques/CT.html](http://serc.carleton.edu/research_education/geochemsheets/techniques/CT.html). Last accessed 31 may 2013.

Ketcham, R.A. & Carlson, W.D. (2001). Acquisition, optimization and interpretation of X-ray computed tomographic imagery: applications to the geosciences. *Computers & Geosciences*. 27, 381-400.

Klinkenberg, L.J. (1941). The permeability of porous media to liquids and gases. *API Drilling and Production Practice*. 200-213.

Knoll, G.F. (2000). *Radiation Detection and Measurement*. New York: Wiley.

Maher, H.D.Jr. (1989). A storm-related origin for the Jurassic Brentskardhaugen Bed of Spitsbergen, Norway. *Polar Research*. 7, 66-77.

Major, H., Haremo, P., Dallmann, W.K. & Andresen, A. (2000). Geological map of Svalbard 1:100 000, sheet C9G Adventdalen (revised after Major 1964). *Norsk Polarinstitutt Temakart nr. 31*.

Mørk, A., Hynne, I.B. & Rød, R.S. (2010). Upper Triassic sandstones as possible reservoir for CO<sub>2</sub> storage below Longyearbyen, Svalbard. 29<sup>th</sup> Nordic Geological Winter Meeting, Oslo, 11-13 January. *Abstract and Proceeding of the Geological Society of Norway 1-2010*. 28-29.

- Mørk, M.B.E. (2013). Diagenesis and quartz cement distribution of low-permeability Upper Triassic-Middle Jurassic reservoir sandstones, Longyearbyen CO<sub>2</sub> lab well site in Svalbard, Norway. *American Association for Petroleum Geologists Bulletin*. 97 (4), 577-596.
- Nagy, J. & Berge, S.H. (2008). Micropalaeontological evidence of brackish water conditions during deposition of the Knorringfjellet Formation, Late Triassic-Early Jurassic, Spitsbergen. *Polar Research*. 27, 413-427.
- Ogata, K., Senger, K., Braathen, A., Tveranger, J. & Olaussen, S. (2012). The importance of natural fractures in a tight reservoir for potential CO<sub>2</sub> storage: a case study of the upper Triassic-Middle Jurassic Kapp Toscana Group (Spitsbergen, Arctic Norway). *Geological Society, special Publications* v374. London.
- Olsen, R.K. & Grigg, M.W. (2008). Mercury Injection Capillary Pressure (MICP) A Useful Tool for Improved Understanding of Porosity and Matrix Permeability Distributions in Shale Reservoirs. *AAPG Search and Discovery Article* 40322.
- Ramstad, T., SPE, Øren, P.-E., SPE & Bakke S. (2010). Simulation of Two-phase flow in Reservoir Rocks Using a Lattice Boltzmann Method. *Society for Petroleum Engineers Journal*. 1-11.
- Reineck, H.-E. & Wunderlich, F. (1968). Classification and Origin of Flaser and Lenticular Bedding. *Sedimentology*. 11, 99-104.
- Sandifer, P.A. (1973). Distribution and abundance of decapod crustacean larvae in the York River Estuary and adjacent lower Chesapeake Bay, Virginia, 1968-1969. *Chesapeake Science*. 14, 235-257.
- Span, R. & Wagner, W. (1996). A new equation of state for carbon dioxide covering the fluid region from the triple-point temperature to 1100K at pressures up to 800 Mpa. *Journal of Physical and Chemical Reference Data*. 25 (6), 1509-1596.
- Steel, R.J. & Worsley, D. (1984). Svalbard's post-Caledonian strata: an atlas of sedimentational patterns and palaeogeographic evolution. In: Spencer, A.M. et al. (eds) *Petroleum Geology of the North European Margin*. London: Norwegian Petroleum Society/Graham & Trotman. 109-135.
- Succi, S. (2001). The lattice Boltzmann Equation for Fluid Dynamics and Beyond. *Oxford University Press*.
- Tanikawa, W. & Shimamoto, T. (2006). Interactive comment on "Klinkenberg effect for gas permeability and its comparison to water permeability for porous sedimentary rocks". *Hydrology and Earth System Sciences Discussions*. 3, 997-998.
- Vlassenbroeck, J., Dierick, M., Masschaele, B., Cnudde, V., Van Hoorebeke, J. & Jacobs, P. (2007). Software tools for quantification of X-ray microtomography at the UGCT. *Nuclear Instruments and Methods in Physics Research*. 580, 442-445.
- Vlassenbroeck, J. (2010). Advances in laboratory-based X-ray microtomography. *Phd dissertation, university of Ghent*.
- Voorn, M., Exner, U. & Rath, A. (2013). Multiscale Hessian fracture filtering for the enhancement and segmentation of narrow fractures in 3D image data. *Computers & Geosciences*. 57, 44-53.

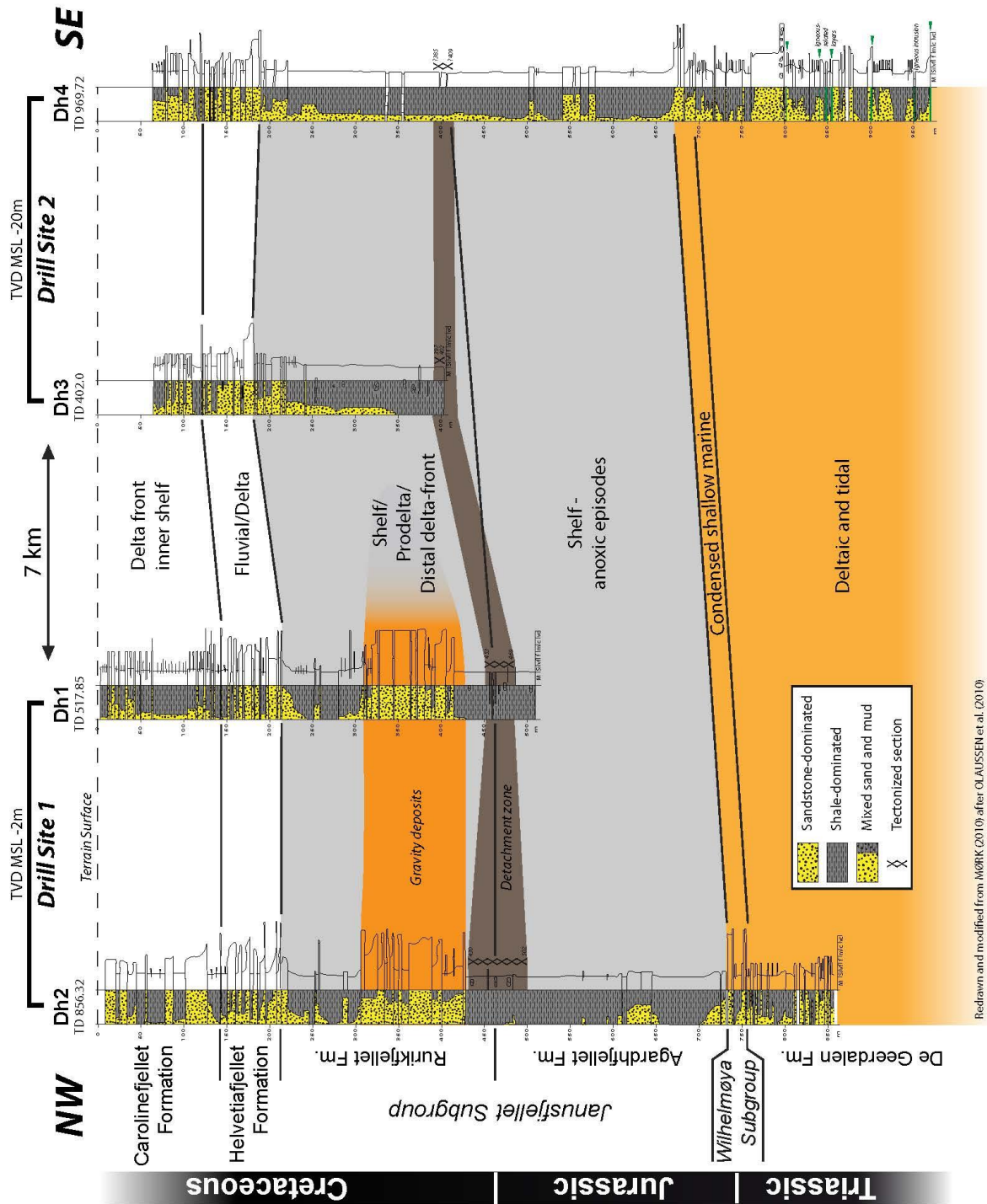


Williams, A.B. (1984). Family Upogebiidae. In: Fisher, D.C. *Shrimps, lobsters and crabs of the Atlantic Coast of the Eastern United States, maine to Florida*. Washington D.C.: Smithsonian institution Press. 190-191.

Worsley, D. (1973). The Wilhelmøya Formation – a new lithostratigraphical unit from the Mesozoic of eastern Svalbard. *Norsk Polarinstitutt Årbok 1971*. 17-34.

Worsley, D. (2008). The Post-Caledonian development of Svalbard and the western Barents Sea. *Polar Research*. 27 (3), 298-317.

# 7. Attachment



Redrawn and modified from HØRKK (2010) after OLUSSEN et al. (2010)

**Attachment 1:** Correlation of four drilled cores, taken from Braathen et al. (2012). One can clearly see that the Wilhelmøya Subgroup and the De Geerdalen Formation are only sampled in Dh2 and Dh4.